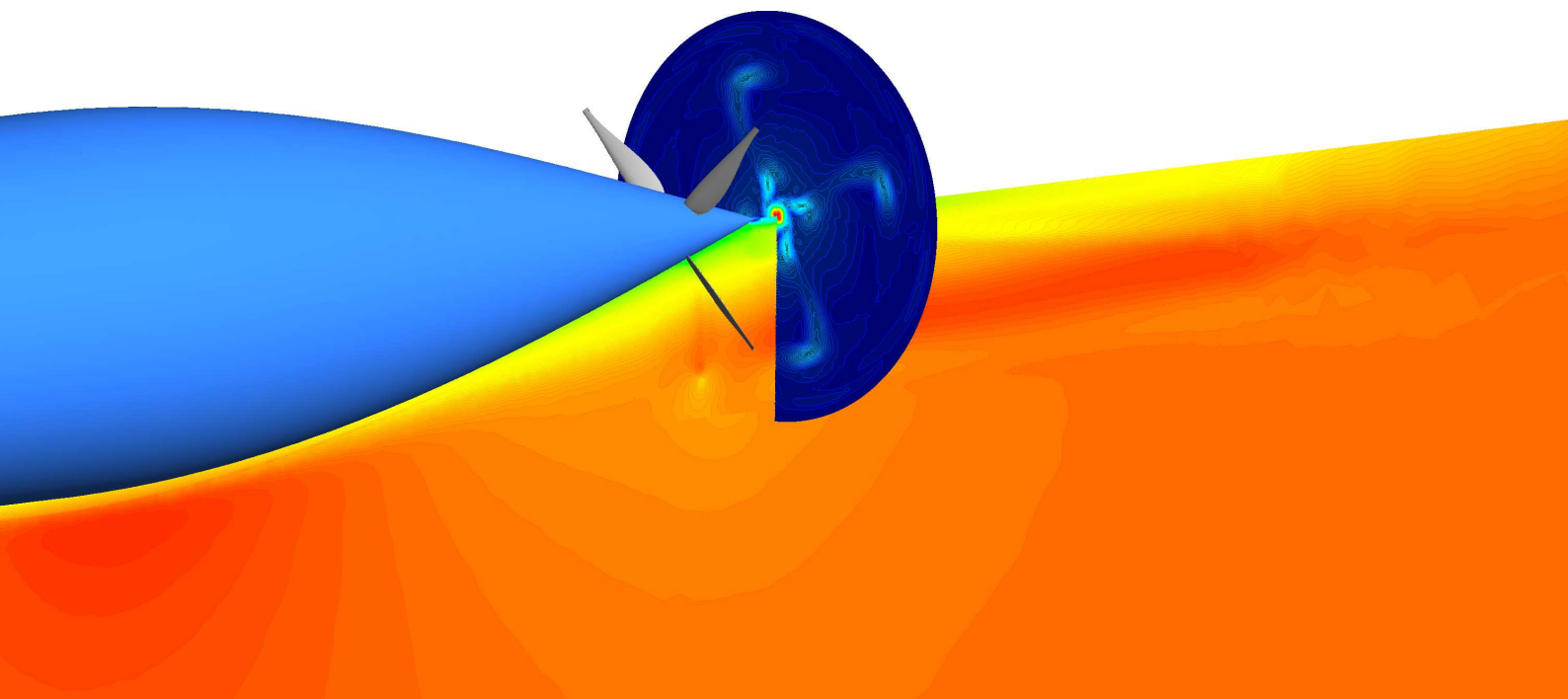


# Design and Analysis of an Installed Pusher Propeller with Boundary Layer Inflow

Nando van Arnhem

Delft University of Technology





# DESIGN AND ANALYSIS OF AN INSTALLED PUSHER PROPELLER WITH BOUNDARY LAYER INFLOW

by

**Nando van Arnhem**

in partial fulfillment of the requirements for the degree of

**Master of Science**  
in Aerospace Engineering

at the Delft University of Technology,  
to be defended publicly on Thursday 17 September, 2015 at 14:00.

Supervisor: P. Lv, MSc  
Thesis committee: Prof. dr. ir. L.L.M. Veldhuis  
Prof. dr. -ing. G. Eitelberg  
dr.ir. J. Sodja  
P. Lv, MSc.

An electronic version of this thesis is available at <http://repository.tudelft.nl/>.  
Thesis Registration Number: 047#15#MT#FPP



# ACKNOWLEDGEMENTS

There are a number of staff members from the Flight Performance and Propulsion group I would like to thank. First of all my supervisor Lex, for his motivation, feedback and time to guide me through the thesis work. When I was stubborn to go my direction, which happened regularly, he kept on being supportive. I would like to thank Leo Veldhuis and Georg Eitelberg for their time, input and motivation to help students during the weekly Propeller Research Group meetings. Those meetings are a nice opportunity to see what fellow students are doing and how things work within our department. Furthermore, thanks to Arvind Rao, all the students and PhD candidates who were present at these meetings for the nice discussions and their suggestions.

Thanks to my friends in Delft who made the studies an enjoyable time. Special thanks to Tom for always being supportive, for proof reading the thesis report and for the nice discussions.

Last but not least, I want to thank my parents for their support. Without them I may not have studied Aerospace Engineering as at the age of eleven they gave me the opportunity to fly radio-controlled aircraft and helicopters. That hobby very likely made me decide to study Aerospace Engineering.

*Nando van Arnhem  
Delft, September 2015*



# ABSTRACT

Boundary Layer Ingestion is an integrated propulsion concept in which a propulsor operates in boundary layer flow instead of the free stream flow with the goal to reduce the fuel flow for a given operating condition. The objective of this thesis is to obtain a better understanding of the power benefit of an installed pusher propeller at the aft fuselage by designing the aerodynamic shape of the propeller and validate the design by means of Computational Fluid Dynamics (CFD) simulations.

A propeller analysis tool for uniform inflow (UI) and non-uniform inflow (NUI) named N-XROTOR is developed using the lifting line code XROTOR [1] in combination with XFOIL [2] to calculate airfoil properties. The tool is validated using experimental results and results from CFD simulations of uniform inflow propellers. N-XROTOR shows good agreement of the trend of the  $C_T - J$  and  $C_P - J$  curves but a constant over prediction of both thrust and power with respect to experimental data is observed and several deviations are explained.

A series of CFD simulations in ANSYS Fluent™ using a reduced wedge shaped domain of one blade of the N250 propeller are performed for several advance ratios including a grid refinement study. Minor deviations between a transient and a steady simulation are found and the steady method is chosen based on computational cost. The trends of N-XROTOR in terms of  $C_T - J$  and  $C_P - J$  compare well with the CFD simulation with a constant over prediction of the performance quantities by N-XROTOR. These over predictions are also noticeable in the radial distributions of thrust and torque with slight over predictions in the high loaded region on the blade. For a moderate advance ratio of  $J = 0.79$  the thrust and power are over predicted by 5.25% and 3.67% respectively. A comparison with the standard  $\kappa - \omega$  SST turbulence model and the SST model with low Reynolds number correction is made. The radial flow on the propeller blade is shown to be quite significant and varies along the blade and shows good agreement with the distribution of bound circulation and the resulting trailing vorticity.

A design procedure is developed in which the propeller shape is optimised using shape functions to describe the pitch and chord distribution and a NACA four series airfoil is used to limit the number of design variables for a gradient based optimisation algorithm in Matlab environment. The interaction effects are assumed to be determined a-priori and a tapered aft fuselage and the pressure field induced by the fuselage are neglected. Input quantities for the design routine include a inflow field from CFD analysis, the design advance ratio and a thrust requirement. The design objective of all optimisations is minimum power.

For the reference design case an axisymmetric body from ESDU is subject to CFD simulations to obtain the inflow profile and fuselage drag for the isolated and installed configuration. Interference effects are approximated using an Actuator Disk (AD) model at the predefined location of the propeller with a pressure jump equal to the defect in total pressure in the boundary layer based on findings from previous research [3]. An 11% increase of drag is found for the equilibrium condition which is primarily due to increased pressure drag. Larger pressure jumps show only a marginal increase in drag.

In a comparison study, the number of blades is set to four, an advance ratio of  $J = 1.50$  is chosen and in combination with a radius equal to 99% of the total gage pressure of the undisturbed air yields a tip Mach number of around 0.50. The optimisation results show that the NUI propeller requires 6.93% less power compared with the UI propeller despite the 11% higher thrust. The thrust distribution of the NUI propeller shows a significant increase in thrust in the low axial velocity region towards the root and the maximum thrust is shifted inboard. The ratio of thrust to torque  $\frac{dT}{dQ\Omega}$  along the propeller blade shows a constant distribution for the UI propeller, while the NUI propeller has a smooth increasing distribution towards the root. This distribution shows that thrust requires a relatively low power when the local axial velocity is relatively low. It is found that this is the main benefit of positioning a propeller in the boundary layer. The bound circulation distribution shows a shift towards the root compared with the distribution of the uniform inflow propeller which is the result of the optimised propeller shape which benefits from the favourable thrust to power ratio in the inner radii. The NUI propeller has a significant increased chord compared with the optimal UI and also a higher lift coefficient distribution. The local efficiency defined as  $\eta_{local} = \frac{dT V_a}{dQ\Omega}$  with  $V_a$  as the local inflow velocity. Optimal UI propellers have a constant efficiency distribution, but the NUI propeller shows a decreasing trend towards the root which is also found in literature. The trend of lower  $\eta_{local}$  is also found

when an optimisation for minimum power is performed using a radially varying actuator disk with the same inflow and thrust requirement as for the full blade propeller. Additional analysis on the NUI propeller include comparison of off design conditions and additional optimisations are performed to quantify the effect of the number of blades, radius and advance ratio.

The optimised NUI propeller in the installed configuration is simulated using CFD. N-XROTOR over predicts the thrust and power by 4.15% and 4.71% respectively compared with the CFD simulation, which are deviations of the same order as the N250 simulation. The  $\frac{dT}{dQ\Omega}$  distribution shows good correspondence. In the root region this ratio is under predicted by N-XROTOR which is expected to be the result of a large pressure and velocity gradient at the junction of the spinner and propeller surface resulting in a region of recirculation. Also the blockage effect of the tapered spinner results in larger angles of attack in the root region. The outer region ( $\frac{r}{R} = 0.7...0.95$ ) shows trailing edge stall which is found to be primarily due to the coarse mesh in that region. Improved results are obtained when N-XROTOR uses airfoil data obtained from two-dimensional CFD analysis of a particular airfoil section. The  $\kappa - \omega$  SST model with low Reynolds number correction shows almost exact agreement with XFOIL. The standard turbulence model shows a decambering effect and an earlier stall behaviour.

The remaining deviations between N-XROTOR with approximated CFD airfoil properties are expected to originate from the radial flow on the blade and the variation in circulation in chordwise directions which are not simulated in N-XROTOR. Both the externally induced radial flow by the tapered aft fuselage and the self induced radial flow are expected to result in a decambering of the airfoil due to the influence on boundary layer growth as well as a reduced chord wise velocity resulting in a locally lower dynamic pressure experienced by the airfoil contour.

The interference effects of the propeller onto the fuselage are compared with the Actuator Disk (AD) approximation. An over prediction of 0.74% of the drag by the AD model of the fuselage excluding spinner is observed. Downstream of the full blade simulation the pressure is rapidly decreased to a low finite value at the aft end of the spinner. This is the result of the finite bound circulation at the propeller root which releases a strong trailing vortex from each blade. These vortices combine into a strong axial vortex which induces a strong tangential velocity and therefore in a low pressure acting on the spinner. A slipstream analysis is performed of circumferentially averaged flow quantities in radial direction at a plane behind the propeller and the axial development of several averaged flow quantities is shown.

Several recommendations for future work are formulated to improve the propeller design, improve the design procedure, reduce the interference effects and increase the power benefit of the non-uniform inflow propeller.

# CONTENTS

<b>Abstract</b>	<b>v</b>
<b>Nomenclature</b>	<b>viii</b>
<b>1 Introduction</b>	<b>1</b>
1.1 History of Propellers with an Upstream Body	1
1.2 Previous Research on Boundary Layer Ingestion	3
1.3 Previous Propeller with a Boundary Layer Inflow Design Studies	5
1.4 Research Objective	5
1.5 Scope of Thesis	6
1.6 Outline of Thesis	6
<b>2 Preliminary Analysis of Non Uniform Inflow Effects on Propeller Performance</b>	<b>7</b>
2.1 Simplified Analysis of a Reduced Inflow	7
2.2 Propeller Vortex System	9
2.3 Installation Effects of an Integrated Propeller	10
2.4 Local Propeller Efficiency	11
<b>3 N-XROTOR: Propeller Design Tool for Non-Uniform Inflow</b>	<b>17</b>
3.1 Choice of Propeller Analysis Method	17
3.2 N-XROTOR: Propeller Lifting Line Code	18
3.2.1 XROTOR	18
3.2.2 Airfoil Section Data	20
3.3 Simplification of the Inflow Profile	21
3.4 Description of Optimisation Problem	22
3.4.1 Optimisation Setup	22
3.4.2 Design Variables	23
3.4.3 Constraints	25
3.5 Reference Case: Optimisation for Uniform Inflow	26
<b>4 Validation of N-XROTOR for Uniform Inflow</b>	<b>29</b>
4.1 Comparison of N-XROTOR Results with Experimental Results	29
4.2 CFD Analysis of N250 Propeller	30
4.2.1 Computation Method and Solver	30
4.2.2 Turbulence Model	31
4.2.3 Discretisation Schemes	33
4.2.4 Domain and Boundary Conditions	33
4.2.5 Mesh and Mesh Refinement Study	35
4.3 Comparison of CFD Results with N-XROTOR	35
4.3.1 Radial Distributions and Performance	36
4.3.2 Effect of Airfoil Properties	37
4.3.3 Radial Flow	37
4.3.4 Comparison of Multiple Reference Frame and Sliding Mesh	38
<b>5 CFD Simulation of a Reference Non-Uniform Inflow</b>	<b>45</b>
5.1 Geometry of Reference Fuselage and Operating Condition	45
5.2 CFD Simulation of the Isolated Fuselage	46
5.2.1 Computational Settings	46
5.2.2 Domain and Boundary Conditions	47
5.2.3 Mesh Setup and Mesh Independence Study	47
5.3 Some Results	48
5.4 Approximation of Upstream Effects Propeller	50

<b>6</b>	<b>Optimisation Results</b>	<b>55</b>
6.1	Effect of Uniform $V_\infty$ on Required Power	55
6.2	Description of Design Condition	56
6.3	Discussion of Results	57
6.4	Performance Graphs	61
6.5	Additional Optimisation Results	61
6.5.1	Design with Equivalent Velocity	61
6.5.2	Effect of Additional Thrust	61
6.5.3	Effect of Number of Blades	63
6.5.4	Effect of Advance Ratio	64
6.5.5	Effect of Tip Radius	64
<b>7</b>	<b>CFD Analysis of Optimised Propeller</b>	<b>67</b>
7.1	Computational Setup	67
7.2	Comparison with N-XROTOR	68
7.2.1	Radial Distributions	68
7.2.2	Influence of Airfoil Data and Turbulence Model	69
7.2.3	Radial Flow	72
7.2.4	Stall at Outboard Sections	73
7.2.5	Performance of Root Sections	74
7.3	Effect Propeller on Aft Fuselage	78
7.4	Description of Slipstream	81
7.4.1	Radial Distributions with and without Propeller	81
7.4.2	Development of Flow Quantities in Axial Direction	81
<b>8</b>	<b>Conclusions and Recommendations</b>	<b>87</b>
8.1	Conclusions	87
8.2	Recommendations for Further Research	90
<b>A</b>	<b>Geometry Description of Two Propellers used in Validation of N-XROTOR</b>	<b>93</b>
A.1	N250 Propeller	93
A.2	NACA-3 Propeller	93
<b>B</b>	<b>Additional Results of the N250 Propeller</b>	<b>95</b>
B.1	Mesh Refinement Study in N-XROTOR	95
B.2	Mesh Refinement Study	95
B.3	Effect of Transition in N-XROTOR on $C_l(r)$ and $C_d(r)$	99
B.4	Effect of low- $Re$ Correction on CFD Results	99
<b>C</b>	<b>Description of Reference Fuselage Shape</b>	<b>101</b>
<b>D</b>	<b>CFD Setup of NACA Airfoil Simulation</b>	<b>103</b>
D.1	CFD Setup	103
D.2	Grid Refinement Study	103
D.3	Effect of Turbulence Model	103
	<b>References</b>	<b>105</b>

# NOMENCLATURE

## Greek Symbols

$\delta_{99}$	Boundary layer thickness based on total pressure
$\gamma$	Vorticity = $-\frac{d\Gamma}{dy}$
$\Gamma_B$	Bound circulation
$\Omega$	Propeller rotational speed
$\Phi$	Rate of dissipation
$\phi$	Outflow angle including induced velocities
$\phi'$	Outflow angle excluding induced velocities
$\mu$	Dynamic viscosity
$\rho$	Density
$\eta_{local}$	Local propeller efficiency at radial position $r$
$\gamma_a$	Vorticity in axial direction
$\gamma_t$	Vorticity in tangential direction
$\eta_{propeller}$	Propeller efficiency

## Other Symbols

$\bar{g}$	Inequality constraints
$\bar{h}$	Equality constraints
$\bar{x}$	Design vector
$\beta$	Geometrical pitch angle
$\Delta D_{pressure}$	Interference drag due to an increased pressure drag
$\Delta D_{skin}$	Interference drag due to an increased skin friction drag
$\Delta p_{fan}$	Pressure jump at the Actuator Disk
$\Delta T_{\frac{dp}{dx}}, \Delta P_{\frac{dp}{dx}}$	Change in thrust and power due to an axial pressure gradient induced by the fuselage
$\dot{E}_a$	Axial kinetic energy deposition rate $\dot{E}_a = \iint \frac{1}{2} \rho u^2 (V_\infty + u) dS^{TP}$
$\dot{E}_p$	Pressure work deposition rate $\dot{E}_p = \iint (p - p_\infty) u dS^{TP}$
$\dot{E}_v$	Transverse kinetic energy deposition rate $\dot{E}_v = \iint \frac{1}{2} \rho u^2 (v^2 + w^2) (V_\infty + u) dS^{TP}$
$\frac{V_a}{nD}$	Local advance ratio
$A_d$	Disk area
$B$	Number of blades
$c$	A constant
$c$	Chord
$C_d$	Section drag coefficient
$C_l$	Section lift coefficient
$C_P$	Power coefficient = $\frac{P}{\rho n^3 D^5}$

$C_Q$	Torque coefficient = $\frac{Q}{\rho n^2 D^5}$
$C_T$	Thrust coefficient = $\frac{T}{\rho n^2 D^4}$
$C_{d,fuselage}$	Drag coefficient fuselage
$D$	Propeller diameter
$D_{fuselage}$	Fuselage drag
$D_{installed}$	Total drag of the fuselage with a propeller installed
$D_{isolated}$	Drag of isolate fuselage
$D_{vortex}$	Drag induced by a (hub) vortex
$dp$	Pressure difference induced by the fuselage at the propeller location
$dQ$	Torque of blade section
$dT$	Thrust of blade section
$J$	Advance ratio = $\frac{V_\infty}{nD}$
$L_{fuselage}$	Fuselage length
$M$	Mach number
$n$	Rotational speed
$N_{crit}$	Critical amplification ratio of $e^N$ method
$p$	Pressure
$P_{momentum}$	Power required according to axial momentum theory
$P_{shaft}$	Propeller shaft power
$p_{t,0}$	Total pressure of free stream flow
$p_t$	Total pressure
$Q$	Propeller torque
$R$	Propeller radius
$r$	Radial position
$R_{hub}$	Propeller hub radius
$Re$	Reynolds number
$Re_L$	Reynolds number based on fuselage length
$S_{fuselage}$	Fuselage surface area
$T$	Thrust
$T_{momentum}$	Thrust according to axial momentum theory
$T_{ref}$	Design thrust
$T_{shaft,installed}$	Required installed shaft power of the propeller
$T_t$	Total temperature
$Tu$	Turbulence intensity
$u', v', w'$	Fluctuations w.r.t. mean flow
$u, v, w$	Perturbed velocity components relative to the freestream flow
$V_\infty$	Freestream velocity
$V_a$	Local axial inflow velocity
$V_{eff}$	Effective velocity of an airfoil section
$V_{i,a}$	Axial induced velocity
$V_{i,t}$	Tangential induced velocity
$v'$	Axial velocity of a vortex sheet

# 1

## INTRODUCTION

Most aircraft have a clear architecture: the lift production, payload holding and propulsion components are separated from each other. By minimising the interactions between these components the complexity in terms of maintenance and design is limited. However, with the assigned efficiency improvements for the future generation of aircraft by the European Union in the "Flightpath 2050" agenda [4], integrated propulsion systems with the goal of improving the aircraft's efficiency have gained increased attention [5, 6]. One of the integrated propulsion concepts is to position a propulsor, instead of the free stream flow, inside the boundary layer of the aircraft with the goal of reducing the fuel consumption. A frequently used terminology for such configuration is 'Boundary Layer Ingestion' (BLI) or 'wake ingestion' when the propulsor has the wake of an upstream body as inflow. Before this integrated propulsion system is applied in further wind tunnel and full scale tests, it is of importance to design a dedicated propeller for this configuration and analyse the flow phenomena at the integrated propulsor.

In section 1.1 some history on propellers with an upstream body is presented. Recent research related to the concept is discussed in section 1.2 and some previous research on propeller design for non-uniform inflow is discussed in section 1.3. The motivation for research, the research objective and its goals are stated in section 1.4. The scope and outline of the thesis are discussed in sections 1.5 and 1.6 respectively.

### 1.1. HISTORY OF PROPELLERS WITH AN UPSTREAM BODY

A propeller is a highly efficient means of propulsion because the change of momentum to produce a certain thrust is introduced by a small velocity change. This small change in velocity results in a relatively low kinetic energy that is deposited into the propeller slipstream [7], resulting in high propulsive efficiency, for an isolated propeller often expressed as  $\eta_p = \frac{TV_\infty}{P_{shaft}}$ . The kinetic energy that is added to the free stream flow is closely related to the shaft power of the propeller. In addition to the power required to increase the axial momentum, kinetic energy is lost in the swirling motion and the viscous effects in the propeller boundary layer lead to dissipation of energy. Blade profile losses account for a small fraction of the total power, typically a few percent [7]. When transverse kinetic energy losses and profile drag losses are neglected, the efficiency is a function of the relative axial induced velocity only such that the efficiency is reduced when the ratio of axial induced velocity to the freestream velocity is relatively large. A low axial velocity requires a relatively large induced axial velocity when a thrust requirement is to be met. For a three dimensional blade, a frequently used quantity to express the efficiency as function of operating condition for a given propeller geometry is the advance ratio  $J = \frac{V_\infty}{nD}$ . Typical efficiency-advance ratio curves show a reducing efficiency at reducing advance ratio. For constant rotational speed this means a reducing efficiency with reducing axial velocity [8]. This behaviour of the efficiency curve rises a relevant question of why one would place a propeller in a lower axial flow if the efficiency of the (isolated) propulsor is decreased.

The effect of an upstream body on the performance of a propeller has been investigated in several experiments and theoretical studies by a number of authors. Already in 1917 in Fage and Collins [9] it was noted that the maximum system efficiency is increased when the airflow experienced by the propeller has a lower velocity than the free stream velocity. In a contribution from Glauert in the collected works of Durand [10] from 1935 the interference between a propeller and an upstream body was briefly discussed. It was recognised that the propulsive efficiency may be increased with a propeller operating in a lower velocity than the

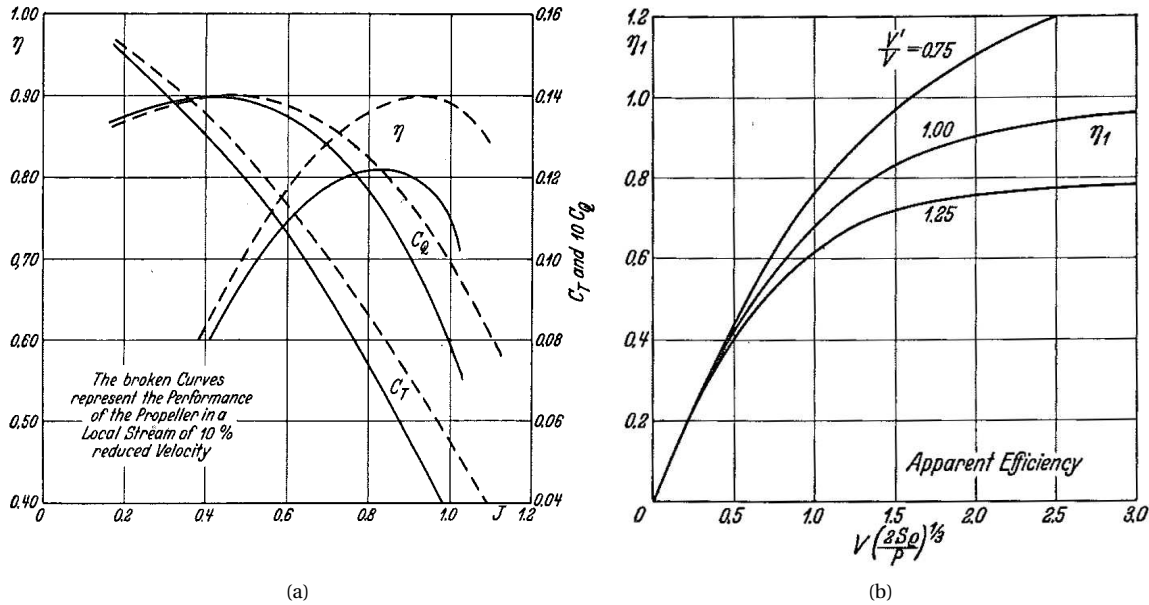


Figure 1.1: (a) The effect of a reduced velocity experienced by the propeller with respect to the freestream flow on the propulsive performance. (b) The effect of a reduced velocity experienced by the propulsor on the efficiency. Source: Durand [10]

body it propels, as shown in figure 1.1 (a). The figure shows that when the propulsor is positioned in a local flow field with a 10% reduced velocity compared with the free stream velocity, the thrust and the torque coefficients ( $C_T = \frac{T}{\rho n^2 D^4}$  and  $C_Q = \frac{Q}{\rho n^2 D^5}$  respectively) are increased compared with the reference case and because the thrust is increased more than the torque, the efficiency is increased and shifted to higher advance ratios. When a thrust requirement is to be met, the required power is reduced by this lower inflow velocity. It was recognised that when the definition of  $\eta_p = \frac{TV_\infty}{P_{shaft}}$  is used, the efficiency can become greater than unity, as depicted in figure 1.1 (b). It was recommended that a complete solution including interference effects is necessary to conclude on possible benefits or disadvantages in terms of power for this configuration. It was found that when the efficiency was corrected for the additional drag of the body, in some experiments the maximum efficiency was decreased, although these propellers were not specifically designed for this operating condition. Betz [11] noted that: "A favourable arrangement of propeller and vehicle leads to a better efficiency than that of the same propeller in an undisturbed stream". In addition it was noted that the power expended of a propeller operating in a boundary layer or wake of a body can be less than the product of forward speed and drag of the aircraft.

A propulsor operating in the boundary layer of a body has been applied regularly in marine applications such as torpedos and ships. In aerial applications mostly cruise missiles have such configuration. Unpublished studies on cruise missiles have indicated a power reduction of around 7% due to the position of the propulsor being in the boundary layer of the missile [12]. In those cases the total drag of the missile is overcome by the thrust of the propulsor. Aircraft propulsors are required to overcome the drag of the total aircraft. Some examples of airplanes with a pusher propeller installed on the aft fuselage as a sole means of propulsion or as a fraction of the total propulsion system are available. The XB-42 aircraft (shown in figure 1.2 (a)) has shown to have superior performance compared with aircraft of its class as noted in Lv and Rao [3]. Although not taken into production, the Lear Fan (figure 1.2 (b)) also has a pusher propeller. Primary benefits were mentioned as noise shielding and a thrust vector through the center of gravity improving safety and handling qualities [13]. Recently, a number of research studies have been conducted on BLI for civilian transport aircraft. Boeing has performed research on BLI for a Blended Wing Body (BWB) aircraft with propulsors installed on the upper surface of the aircraft [14]. The Cambridge-MIT Institute developed the D8 aircraft concept together with NASA [15] in which the propulsor is mounted on the upper surface of the aft fuselage. Bauhaus Luftfahrt currently investigates the 'propulsive fuselage concept' [6], shown in figure 1.2 (c). VoltAir, an Airbus Group owned subsidiary, is developing an electric aircraft utilising BLI using contra-rotating propellers located on the aft-fuselage (shown in figure 1.2 (d)).

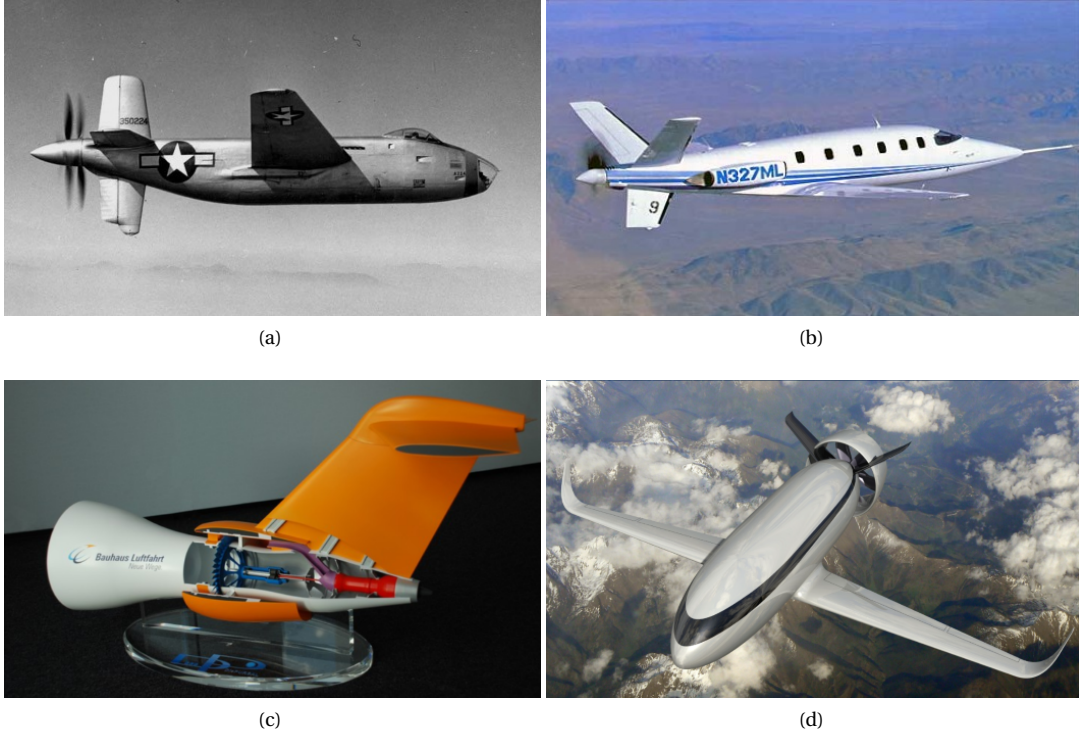


Figure 1.2: Examples of propellers operating in a wake: (a) Douglas XB-42 aircraft from [16], (b) Lear Fan aircraft from [17], (c) Propulsive fuselage concept from [18] and (d) Voltair from [19]

## 1.2. PREVIOUS RESEARCH ON BOUNDARY LAYER INGESTION

The concept of Boundary Layer Ingestion (BLI) has been investigated by various authors and some of the theory developed is considered in this section.

A mathematical tool which is used by several authors is a Control Volume (CV), e.g. by [3, 20–22]. By using a CV instead of a force based method to determine the required power, also integrated propulsion systems such as BLI may be analysed more accurately [20]. A method using a CV is the Power Balance Method by Drela [20]. The method relates the power balance within the CV, the power that flows into and out of the CV. The upper and lower boundary are streamlines which ensure no mass flow through these boundaries. In Drela [20] the following relation is proposed when the sides of the control volume are far from the body and no supersonic flow is considered:

$$P_S + P_V + P_K = \Phi + \dot{E}_a + \dot{E}_v + \dot{E}_p \quad (1.1)$$

The left hand side consists of the power supplied to the CV. The right hand side of the equation consists of the dissipation rate  $\Phi$  which takes place inside the control volume and of the mechanical energy outflow rate. When the upper and lower boundaries are streamlines, the kinetic energy outflow rates have finite values in a Trefftz plane behind the body and propulsor. To maintain an equilibrium, this kinetic energy outflow rate and dissipation rate is balanced by the shaft power. Drela [20] uses this equation to evaluate the individual terms for different propulsion configurations. Figure 1.3 shows how the terms of a typical conventional aircraft-propulsion configuration evolve downstream. When the Trefftz plane is relatively close to the body and behind the propulsor,  $\Phi$  has the value of the dissipation rate inside the boundary layer. Both the body and propulsor induce velocities, primarily in axial direction. Therefore  $\dot{E}_a + \dot{E}_v$  is larger than zero and close to the body and propulsor the pressure has not reached free stream conditions yet and therefore  $\dot{E}_p$  also is non-zero. When the Trefftz plane is moved downstream, a number of effects occur. First the pressure term is decreasing and is exchanged for increased axial velocity. In addition, the due to the velocity gradients in the slipstream dissipation takes place, i.e.  $\dot{E}_a + \dot{E}_v$  vanish downstream [21]. Arntz et al. [21] uses a similar approach as Drela [20] in which also a thermal energy outflow term is added to the power balance. It is argued that when a propulsor is positioned just behind the body which induces a flow field such that  $\dot{E}_a + \dot{E}_p = 0$  just behind the propulsor. When equation 1.1 is applied to a simplified isolated propeller model in potential

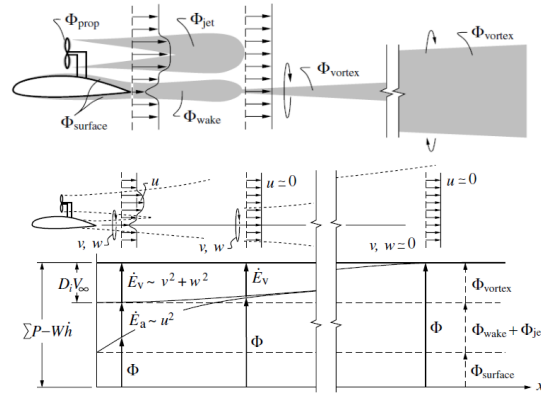


Figure 1.3: Kinetic energy deposition and rate of pressure defect at various positions of a Trefftz plane and identification of dissipation terms in the flow.  $u$  is denoted as the perturbation velocity relative to  $V_\infty$ . Source: [20]

flow, this equation indicates the shaft power is equal to the change in kinetic energy between the free stream conditions and the far downstream conditions. When viscosity is added and the intermediate state of the fluid is to be analysed, equation 1.1 describes these phenomena as well.

Smith [12] used an Actuator Disk approach where the power saving and efficiency were related to wake properties such as a shape factor, displacement thickness and wake recovery. The non-uniformity of the wake is thereby taken into account. A Power Saving Coefficient (PSC) was introduced to express the benefit of wake ingestion. Smith concluded on theoretical bases that the highest efficiency is reached when the wake is completely recovered, i.e. when the defect in velocity is zero behind the propulsor. However, there is no mention of how the pressure influences the solution as the increased pressure behind the propeller will go to ambient conditions and this will increase the axial velocity. Examples by Smith [12] have shown to reduce the power by 20% for complete wake recovery, based on the velocity relative to freestream flow. It was recommended that for practical purposes the interaction effects should be included in the design process.

In Seitz and Gologan [6] a parametric study of the power benefit of a propulsive fuselage (shown in figure 1.2 (c)) configuration was performed using drag predictions using empirical methods. The inflow field and 'ideal wake filling' was assumed. PSCs in the order of 10% were found compared with a propulsor in uniform flow with equal disk area although interaction effects were not discussed. Recommendations included a more precise radial distribution of velocity, a better understanding of the loss effects of the propulsor and more practical considerations concerning installation are required for further analysis.

In Atinault et al. [5] both a numerical and experimental analysis were performed of a body of revolution. A modified propulsive efficiency was proposed which is also a function of the velocity in the wake  $V_w$ :  $\eta_{modified} = \frac{2V_\infty}{V_j + V_w}$  with  $V_j$  the jet velocity far downstream of the propulsor. A preliminary study showed a power benefit of 9% when a full ingestion of the wake was realised and a force balance was maintained. Experimental results using an off the shelf fan showed an decreasing PSC with increasing distance between propulsor and fuselage in axial direction; the propulsor should be close to the body in order to benefit from the low velocity. The configuration with the smallest spacing showed a power benefit of around 22%. Numerical studies included an Actuator Disk with a pressure jump and a jump in tangential velocity and showed reasonable agreement with the experimental results.

Kim and Felder [22] investigated the effect of a total pressure loss and low velocity upstream of a turbofan with an infinite by-pass ratio (electric motor) and no by-pass ratio (pure turbojet). Instead of a power benefit a thrust benefit was investigated which is approximately linear with a power benefit. A quasi-one dimensional analysis with averaged flow quantities was performed. The conclusion was that an electric fan benefits from the boundary layer ingestion while a turbojet performs best in free stream flow due to the higher total pressure entering the turbojet. A reduced total pressure compared with free stream conditions results in a lower thermal efficiency and for the same thrust a larger fuel mass flow is required [8].

### 1.3. PREVIOUS PROPELLER WITH A BOUNDARY LAYER INFLOW DESIGN STUDIES

A range of literature is found related to propulsor design of a propeller operating in the radially non-uniform boundary layer flow. Already in 1927 it was observed by Helmbold [23] that *"The construction of the ideal wake screw leads to a higher loading where the frictional wake is greatest"*. This observation is also made in Lv and Rao [3], in which a conceptual propulsor design is presented. It is noted that an ideal propulsor fully recovers the defect in total pressure to minimise the kinetic energy deposition in the flow behind the propeller. The blade loading should have a loading inversely to the upstream total pressure profile. It is recognised that this is not possible in reality as the potential of creating a large induced velocity in the root region is difficult due to the low dynamic pressure experienced by the root airfoil sections. A relatively larger chord is proposed in the root region with an adapted pitch angle distribution. A two stage propulsor may be used in which the smaller second propulsor may have a significantly higher rotational speed than the larger main propulsor due to tip Mach number limitations, allowing for a higher local loading in the region of lowest axial velocity.

The work of Hirner et al. [24] on the dedicated design of a pusher propeller operating in the fuselage boundary layer has some similarities with this thesis. It was recognised that a dedicated design for the non-uniform inflow is necessary in order to effectively use the propulsor. Two propellers were designed for two different aft fuselage shapes. It was recognised that the interference of the propeller and the fuselage results in an additional fuselage drag and the design should be such that this effect is smaller than the lower required power to lead to a net benefit relative to a uniform inflow propeller. The paper does not elaborate on the propeller design and shows only radial distributions of induced velocity. The design procedure was briefly mentioned to be in accordance with the optimal distribution by Larrabee and French [25] and Goldstein [26], of which the theory applies for uniform inflow only. There was no mention of adapting this optimisation for a non-uniform inflow, which has a different optimal distributions as will be shown throughout this thesis. In addition, as validation the propeller design was only simulated using an Actuator Disk instead of a full three-dimensional blade.

### 1.4. RESEARCH OBJECTIVE

The previously mentioned research mainly use off-the-shelf propellers which are designed to operate in uniform flow or use a theoretical propeller to describe the change in flow quantities. Although the efficiency of propellers is highly dependent on the installation angle, advance ratio and twist distribution [27–29], little or no attention is paid on the propeller design. A propeller subject to a radially non-uniform inflow profile therefore requires to be specifically designed for that operating condition as different chord and pitch distributions are expected compared with uniform inflow propellers.

Previous research suggest that minimal power is required when the boundary layer or wake is fully recovered. However, ideal wake filling may not be reached due to limitations of a finite number of blades, airfoil properties with limitations in terms of lift and finite losses related to tangential velocities and viscous losses on airfoil sections. Therefore, next to 'high level' performance analysis on the integrated propulsor concept, an important step to further development of this configuration is to investigate what the optimal shape is for a propeller with the non-uniform inflow profile and what the installation effects are. As the potential power benefit is frequently determined and expressed by the flow quantities in the slipstream it is important to explain the benefit by the radial distributions on the propeller blade as well. Therefore the following objective of this thesis is formulated:

**OBJ** *'The objective of this thesis is to obtain a better understanding of the power benefit of an installed pusher propeller operating in the boundary layer of an aft-fuselage by developing a numerical method to design the aerodynamic shape of the propeller and validate the design by means of CFD simulations'*

This objective may be decomposed into several goals which are to be fulfilled throughout the research:

- G1** Develop a propeller analysis and design code for non-uniform inflow in radial direction and validate the results using reference propellers.
- G2** Identify the differences in required power and radial distributions of a propeller designed for non-uniform inflow compared with a propeller optimised for uniform inflow.
- G3** Validate the design by means of CFD simulations.
- G4** Analyse the mutual interference effects between the propeller and the fuselage.

## 1.5. SCOPE OF THESIS

Only pure propellers are considered throughout this thesis. As indicated in Kim and Felder [22], the performance of gas turbines is degraded when the inflow total pressure is reduced due to the viscous effects of the boundary layer. It is therefore assumed that the power supplied to the propeller is not a function of the inflow conditions, e.g. an electric motor may be used as power supply.

The previous sections indicate that theoretically minimal power is achieved when the boundary layer is recovered. Aerodynamic limitations may lead to a propeller which is not capable of reaching that objective. The three dimensional shape is sought for which provides minimum power, hence the design objective in this thesis is minimal power and no objective is imposed to 'fill the boundary layer'. An analysis of the slipstream is provided after the design has been finished.

Installation effects are an important factor when integrated propeller are taken into account and are analysed to a moderate extent. However, no optimisation of the aft fuselage and spinner is performed and these geometries are kept constant throughout the research. An important aspect which is not taken into account is a variation of the flow quantities in circumferential direction. These variations originate from any upstream surfaces such as control surfaces and wings. Angle of incidence changes during the flight also affect the flow in circumferential direction at the plane of the propeller. These effects need to be well understood before full scale tests are to be performed. However, circumferential variations on the propeller flow are expected not to be detrimental to the concept as they can be minimised using smart positioning of the control surfaces and flow can be guided using a duct (e.g. [5]). Installation effects of upstream surfaces of the LearFan have shown relatively low levels of vibrations [13] which indicates that the configuration is not unrealistic.

Although noise production and structural considerations influence the loading distribution and thereby the propeller performance [30–33], no noise and structural considerations are taken into account in this thesis. These limitations on propeller design may be imposed in subsequent optimisations and later design stages.

## 1.6. OUTLINE OF THESIS

This thesis consists of eight chapters including this introduction. Chapter 2 first considers the effect of a reduced uniform inflow velocity on the required power with an actuator disk analysis. A qualitative discussion follows on installation effects of the propeller on the system force balance. Furthermore the non-uniformity of the inflow profile on the propeller vortex sheets and on the efficiency distribution along the blade is briefly discussed.

A non-uniform inflow propeller analysis is presented in Chapter 3. Also the design tool including optimisation method and optimisation objective is discussed. The analysis tool is validated using experimental data on two reference propellers and Computational Fluid Dynamics (CFD) simulations performed by the author in Chapter 4. These simulations will give insight in the validity of the analysis method and what quantitative deviations exist with respect to CFD simulations which are also used to validate the non-uniform inflow design.

A fuselage is chosen in Chapter 5 which is used as a reference case to compare the optimal radial distributions of an installed non-uniform inflow propeller with a uniform inflow propeller. An initial analysis of interference effects is performed as well. Optimisation results on the optimised non-uniform inflow propeller are presented in Chapter 6. To validate these results, a CFD simulation is performed of this optimised propeller in Chapter 7 which also results in a more detailed analysis on the interference effects.

Conclusions and recommendations formulated throughout the research are presented in Chapter 8. These conclusions include findings on the optimal distributions, power savings, interference effects and modelling methods.

# 2

## PRELIMINARY ANALYSIS OF NON UNIFORM INFLOW EFFECTS ON PROPELLER PERFORMANCE

This chapter provides an overview of a primarily qualitative analysis of a non-uniform inflow on a propeller. The following sections should be considered as an introduction to a number of concepts which will be discussed in more detail in the following chapters.

### 2.1. SIMPLIFIED ANALYSIS OF A REDUCED INFLOW

Before a three dimensional propeller including individual blades is considered, it is useful to consider a simplified model of a propeller to understand the flow field through the propeller disk. Figure 2.1 shows what a propeller does to the flow by considering a only axial flow. The purpose of a propeller is to create a thrust, i.e. a change in momentum, by having a pressure distribution such that there is a lower pressure on the upstream side of the propeller and a higher pressure on the downstream side of the propeller. The axial velocity is increased in a smooth manner such the axial induced velocity  $V_{i,a}$  at the propeller disk is half of the induced velocity far downstream the propeller [28]. At the propeller disk there is a jump in total pressure which is the result of the propeller induced velocity and pressure. The two dimensional representation is known as an Actuator Disk (AD) and often neglects the induced tangential velocity which is a result from the torque of the propeller. When the radial and tangential induced velocities are assumed to be zero the total pressure is increased by the pressure jump because at the plane of the AD there is no finite axial velocity change but only a velocity gradient such that:

$$p_{t,downstream} - p_{t,upstream} = \Delta p_s \quad (2.1)$$

The value of the total pressure behind a real propeller is changed by not only the radial and tangential induced velocity but also by the total pressure losses due to the viscous losses in the propeller boundary layer. The integral of the pressure jump over the disk is equal to the thrust. The thrust can also be expressed in a change in momentum between the flow far upstream of the propeller relative to the momentum far downstream of the propeller:

$$\begin{aligned} T_{momentum} &= \Delta M \\ &= \dot{m}(2V_{i,a} + V_\infty - V_\infty) \\ &= 2\rho A_d (V_\infty + V_{i,a}) V_{i,a} \end{aligned} \quad (2.2)$$

The above equation directly shows that for a given thrust requirement and with density  $\rho$  and disk area  $A_d$  given, the axial induced velocities increase with decreasing freestream velocity  $V_\infty$ . According to the momentum theory, the required power is the increase of kinetic energy relative to the kinetic energy far upstream of

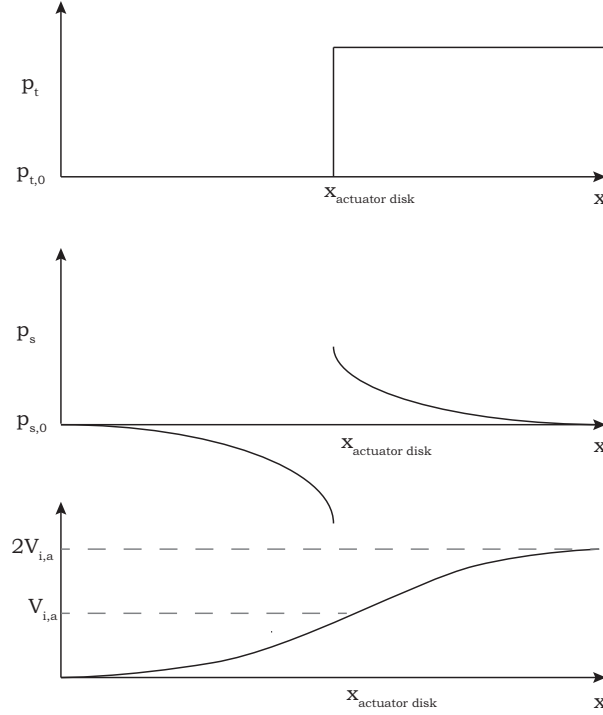


Figure 2.1: Schematic representation of a simplified propeller as an Actuator Disk.

the propeller:

$$\begin{aligned}
 P_{momentum} &= \frac{1}{2} \dot{m} [(V_{\infty} + 2V_{i,a})^2 - V_{\infty}^2] \\
 &= 2\rho A_d (V_{\infty} + V_{i,a})^2 V_{i,a}
 \end{aligned} \tag{2.3}$$

A frequently used quantity to express the performance of a propeller is the propulsive efficiency  $\eta_p$  which is the ratio of useful work done by the propeller per unit time to the total power required to do that work. The efficiency is obviously a function of the propeller geometry and operating condition, hence it is a convenient parameter to compare the performance between two propeller geometries. Absolute agreement on the definition of this efficiency is not present [12], but for a propeller with a uniform inflow  $\eta_{propeller}$  is often expressed as:

$$\eta_{propeller} = \frac{TV_{\infty}}{P_{shaft}} \tag{2.4}$$

For a given thrust requirement, propeller diameter, density and  $V_{\infty}$ , a certain induced velocity is required which leads to a required power. The power required is therefore a function of the axial velocity at the propeller disk and this relation is an important factor for the propeller operating in a boundary layer which has a relatively low axial velocity. To analyse the relation of  $\eta_{propeller}$ ,  $P_{momentum}$  and  $V_{\infty}$  a number of boundary conditions are assumed:

- Thrust requirement  $T$  is constant ( $T = 74.20 [N]$ )
- Radius  $R = 0.2404 m$  and hub radius  $R_{hub} = 0.0530 [m]$
- $\rho = 1.225 [kg/m^3]$

These particular values are related to the results in the subsequent chapters and are used for consistency. For these input values, the  $P_{momentum}$  is plotted against  $V_{\infty}$  in figure 2.2 (a) and the corresponding  $\eta_{propeller}$  is plotted in figure 2.2 (b). The important observation is that the power is proportional to  $V_{\infty}$ ; a relatively low power is required to create the same change in momentum when the free stream velocity is relatively low. This means that the ratio of thrust to power  $\frac{T_{momentum}}{P_{momentum}}$  is relatively high.

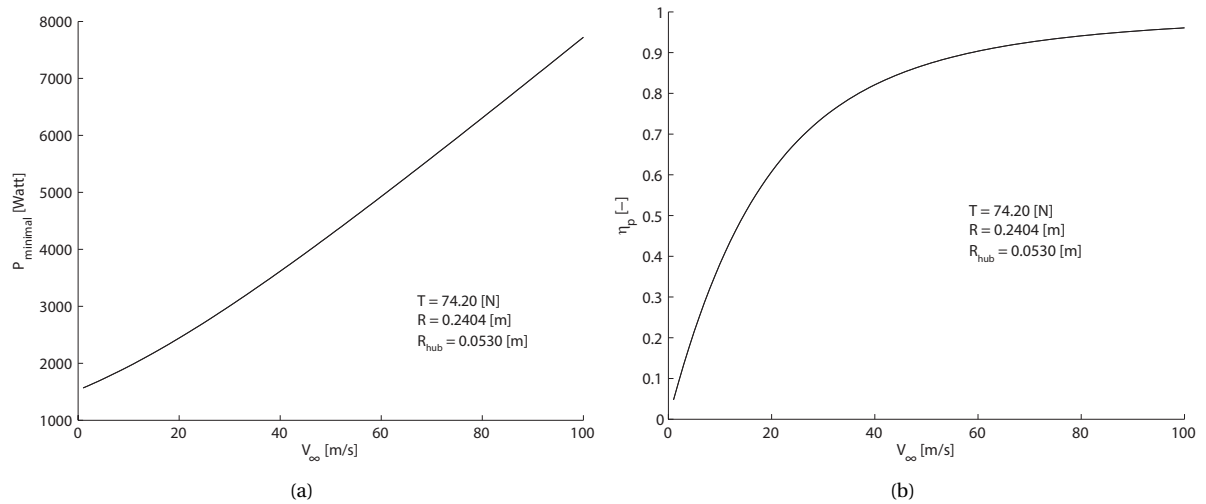


Figure 2.2: Effect of  $V_\infty$  on the power in (a) and efficiency in (b) with a constant thrust, propeller disk area and density according to axial momentum theory.

However  $\eta_{propeller}$  is reducing with reducing  $V_\infty$  indicating that useful work done on the fluid is more efficiently done at higher velocities, which is also found in Glauert [28]. This indicates that the power- $V_\infty$  curve contradicts the  $\eta_{propeller} - V_\infty$  curve. This simplified analysis indicates that when there is a choice between positioning a propeller in a low or high axial velocity field with only a thrust requirement to be met, one should not look at the efficiency but rather the power requirement.

## 2.2. PROPELLER VORTEX SYSTEM

It is important to analyse the vortex system of a propeller because there are implications of the non-uniform flow on this vortex system.

First consider a typical propeller blade section with its forces and local flow angles as depicted in figure 2.3. To understand the flow field around this blade section, potential flow theory may be used. The lifting line theory by Prandtl [34] describes the potential flow about three-dimensional lifting surfaces in which a lifting surface is represented by a line with a bound circulation distribution  $\Gamma_B$  and Betz (e.g. [10]) extended this theory to propellers. The variation of this circulation in radial direction causes the bound vortex to shed free vortex lines  $\gamma$  with a value equal to the variation of bound circulation, i.e.  $\gamma(r) = -\frac{d\Gamma}{dy}$ . In potential flow, the strength of these vortices have a constant strength along the vortex lines. In a 2D case the upwash of an airfoil is equal to the downwash behind the airfoil induced by the bound vortex. However, the trailing vortices change the velocity field around the airfoil such that there is a larger downwash than upwash due to the downward induced velocity. These finite induced velocities (shown in figure 2.3) are generally divided in an axial and tangential component,  $V_{i,a}$  and  $V_{i,t}$  respectively.

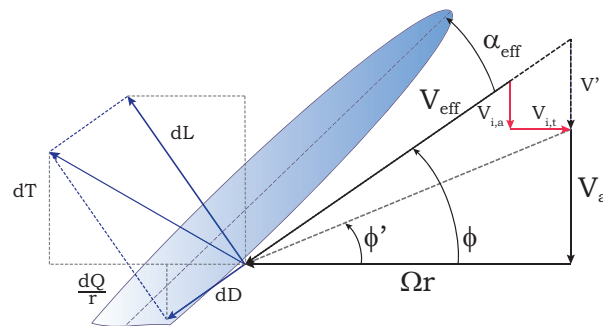


Figure 2.3: Definitions of relevant velocities and corresponding angles at a propeller blade section

A typical vortex architecture is depicted in the left schematic of figure 2.4 (a). For moderately loaded

propellers, the vortex sheets follow the local flow direction and have a pitch equal to  $\phi(r)$  just behind the propeller [35]. When this vortex system is split into the bound vortex and vorticity in the axial and tangential direction, the effect of each of these components to the induced velocity field can be understood. This division is schematically shown in figure 2.4 in which the tangential vorticity is represented by vortex rings. The direction of the separate vortex components constrain the direction in which velocities are induced. At the propeller disk the bound circulation cannot induce an axial flow component due to the symmetrical distribution of this circulation to any point on the disk [10] and only contributes to the tangential flow component. Upstream of the propeller the fluid does not contain vorticity and hence the (average) tangential velocity is zero. Therefore the tangential velocity (or swirl) is induced by the propeller as a jump. This boundary condition dictates that the vortex system downstream of the propeller cancels the upstream effect of the bound circulation. Axial vorticity  $\gamma_a$  can not induce a velocity in the direction of flight; it contributes to the swirl velocity. It is this component which cancels the upstream effect of the bound circulation. The tangential vorticity  $\gamma_t$  however only induces an axial velocity. The two vorticity components are graphically determined to be:

$$\gamma_t(r) = -\frac{d\Gamma_B}{dy} \sin \phi \quad (2.5)$$

$$\gamma_a(r) = -\frac{d\Gamma_B}{dy} \cos \phi \quad (2.6)$$

It may be observed that the local outflow angle  $\phi(r)$  dictates the relative values of axial and tangential vorticity distribution along the radius. It may be expected that the sectional thrust and torque are also functions of this angle because of this vorticity distribution.

The local advance ratio  $\frac{V_a}{nD}$  (with  $n$  being the rotational speed and  $D$  the diameter) of a propeller with uniform inflow and a boundary layer shape inflow are compared in figure 2.4 (b). In this figure the induced velocities are assumed to be zero. It is observed that the propeller subject to an boundary layer shape inflow has a distribution of advance ratios such that the direction of the vortex sheets is more in the plane of rotation. Compared with the propeller with uniform inflow, it may be expected that the ratio of  $\gamma_t(r)$  to  $\gamma_a(r)$  is relatively large in the non-uniform inflow case. From the angle  $\phi'$  alone one cannot conclude on this distribution because also the induced velocities should be taken into account.

### 2.3. INSTALLATION EFFECTS OF AN INTEGRATED PROPELLER

Compared with the isolated fuselage case, an installed propeller changes the flow field around the fuselage and this interference effect has been noted by several authors to be non-negligible [10, 36–38]. This section provides a qualitative discussion of this interference effect because it is an important factor for the propeller design.

Figure 2.5 (a) shows an isolated propeller with a thrust equal to the drag of an isolated fuselage which results in a net force balance. In figure 2.5 (b) the force balance of an integrated propeller is shown. The reduced upstream pressure of an integrated propeller brings an additional drag to the fuselage with respect to the isolated fuselage because the increased axial velocity leads to a larger velocity gradient at the fuselage surface which increases the skin friction. The pressure field is changed by the propeller with the lower upstream pressure increasing the pressure drag on the upstream body. The higher pressure behind the propeller is providing a thrust force on the downstream fuselage surface. However, a tapered aft fuselage generally results in a net drag force as the upstream suction region often acts on a larger surface than the downstream pressure region.

Another effect that changes the flow field and may add to the interference drag is related to a finite circulation at the propeller root which may be present. A finite hub radius leads to a wall effect and allows for a finite circulation at the hub and is often referred to as the hub effect. This circulation sheds a strong vortex from the junction of the blade root with the spinner or fuselage resulting in a locally high induced velocity close to the spinner surface. In Wang [39] and Wald [40] it was noted that this hub vortex results in a strong additional drag on the spinner downstream of the propeller. This effect is elaborated in section 7.3.

The increased required thrust to maintain equilibrium can be referred to as 'thrust deduction' [12]. Based on the division of interference drag and drag from the isolated body (proposed in Rowse [41]) the thrust requirement by of the installed propeller to maintain equilibrium is higher than the isolated case and is equal to:

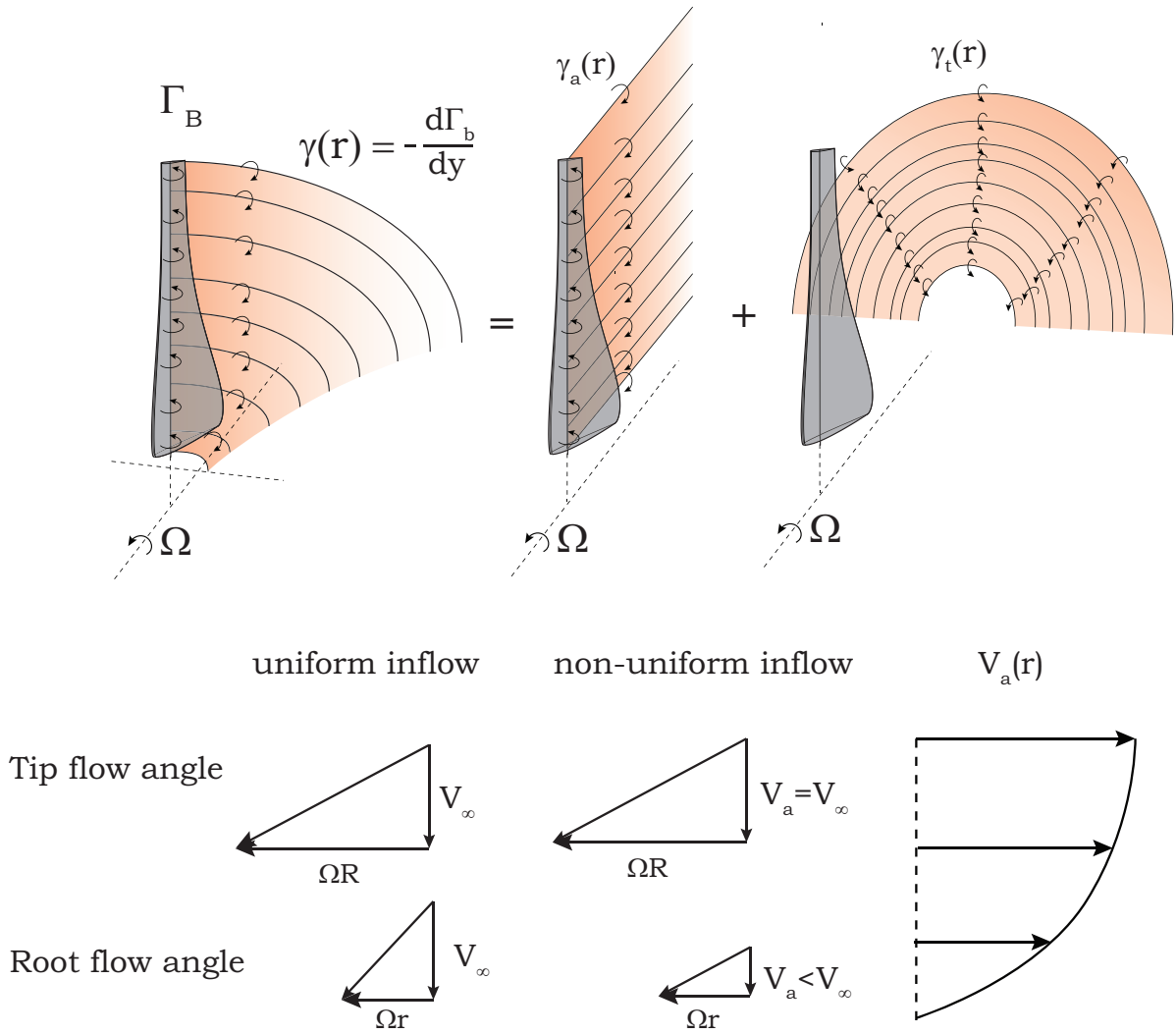


Figure 2.4: The decomposition of the vorticity shed from a lifting line representation of the propeller (top left) into line vortices (top center) and ring vortices (top right). The  $\gamma_a$  only induce velocities in the tangential direction while the  $\gamma_t$  result in axially induced velocities. In the lower figure: a comparison of the local flow angles for a propeller with uniform in flow and a propeller with a boundary layer shape inflow.

$$\begin{aligned}
 T_{shaft,installed} &= D_{isolated} + \Delta D_{skin} + \Delta D_{pressure} \\
 &= D_{installed}
 \end{aligned}
 \tag{2.7}$$

### 2.4. LOCAL PROPELLER EFFICIENCY

Instead of considering the total propeller efficiency, one can look at the efficiencies of propeller blade sections. The optimal efficiency distribution for a uniform inflow propeller is well known. From the brief analysis in section 2.1, the question arises whether the optimal efficiency distribution along a blade of a uniform and non-uniform inflow propeller is the same, which is briefly discussed in this section. It should be noted that this analysis is only to indicate the phenomena of a non-uniform inflow on the efficiency distribution. Any observations made in this section are not proposed as a design objective.

For an isolated propeller-fuselage configuration, the fuselage is flying at  $V_\infty$  with a certain  $D_{isolated}$  and the propeller experiences the same  $V_\infty$ . This means that the propeller does work on the flow which has a relative velocity of  $V_\infty$  with respect to the propeller. However, for an integrated propulsion system this situation changes as the propeller experiences the velocity of the boundary layer  $V_a(r)$  instead of  $V_\infty$  as sketched in figure 2.6. For a propeller operating an airflow with a lower velocity than free stream, the actual work done

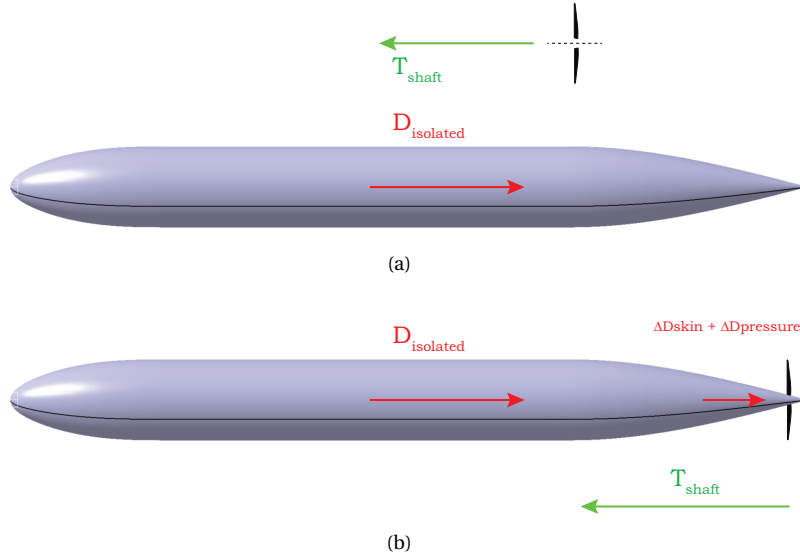


Figure 2.5: In (a) the force balance of an isolated fuselage and an isolated propeller. In (b) a force balance of an integrated propeller inducing an additional drag term consisting of skin friction and pressure drag due to the installation of the propeller.

on the fluid is on the 'reduced inflow field' rather than on the flow with  $V_\infty$ . However, the propeller is still attached to the body which has a velocity  $V_\infty$ .

This leads to the introduction of a local efficiency  $\eta_{local}$ , defined as in equation 2.8. It is the ratio of the local useful work to the local required shaft power  $dQ\Omega$ . This definition indicates what the effectiveness of a section at position  $r/R$  is to produce useful work on the local flow. As the propeller performance in the non-uniform flow is considered in this thesis, the local efficiency  $\eta_{local}(r) = \frac{dT V_a}{dQ\Omega}$  is used in the remainder of this thesis. As discussed in section 2.1, the efficiency alone is not a relevant quantity to compare with when different axial velocities are considered.

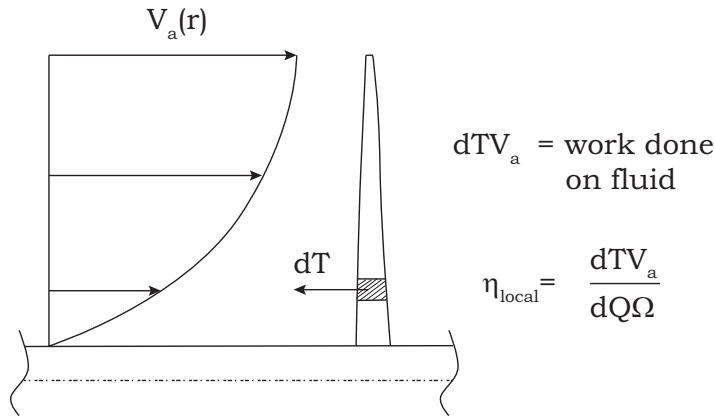


Figure 2.6: The effect of a non uniform flow on the work done on the fluid and the local efficiency.

$$\eta_{local}(r) = \frac{dT V_a}{dQ\Omega} \quad (2.8)$$

It is now interesting to express the section efficiency by the flow field quantities at a particular section. For now, only induced effects are taken into account, i.e.  $C_d = 0$ . Using figure 2.3, one can decompose the thrust and torque components to be functions of  $dL$  and  $dQ$  and then relate to the Kutta-Joukowski theorem. However, these components can also directly be related to the circulation at that radial location as:

$$\begin{aligned} dT &= \rho d\Gamma(\Omega r - V_{i,t}) \\ dQ &= \rho d\Gamma(V_a + V_{i,a})r \end{aligned} \quad (2.9)$$

Therefore the section efficiency is equal to:

$$\begin{aligned} \eta_{propeller} &= \frac{dT V_a}{dQ \Omega} \\ &= \frac{(\Omega r - V_{i,t})}{(V_a + V_{i,a}) \Omega r} \\ &= \frac{\tan \phi'}{\tan \phi} \end{aligned} \quad (2.10)$$

This relation shows that when  $\phi = \phi'$ , hence there are no induced velocities, the efficiency  $\eta_{propeller} = 1$ . An analogy can be made with the efficiency in the momentum theory of a purely axial flow; when the axial induced velocity is 0 [m/s], the efficiency is 1. The question now is, what is the distribution of  $\frac{\tan \phi'}{\tan \phi}$  which leads to the highest total efficiency? A relevant case is to first consider uniform inflow and the theory which is developed there. Munk [10] argued that the efficiency of a uniform inflow propeller should be constant reasoning as follows. The bound circulation varies along a blade with finite radius and if the geometry at a radial location is changed which gives a change in circulation  $\delta\Gamma$ , then the efficiency is slightly changed by  $\delta\eta_{local} = \frac{\delta T V_\infty}{\delta Q \Omega}$  due to the small changes in thrust and torque. If now this  $\delta\eta_{local}$  varies along the radius then it is favourable to increase the circulation at locations where  $\delta\eta_{local}$  is large and reduce the circulation in regions where  $\delta\eta_{local}$  is small. This procedure leads to a constant value  $c$  of efficiency along the blade. As the local efficiency is directly related to the flow angles, the following relation holds for uniform inflow:

$$\frac{\tan \phi'}{\tan \phi} = c \quad (2.11)$$

Betz [42] (elaborated in [10]) investigated what this condition means for the development of the vortex sheets downstream of the propeller. It was found that the axial velocity of the vortex sheet  $v'$  is constant over the blade and is visualised in figure 2.7.

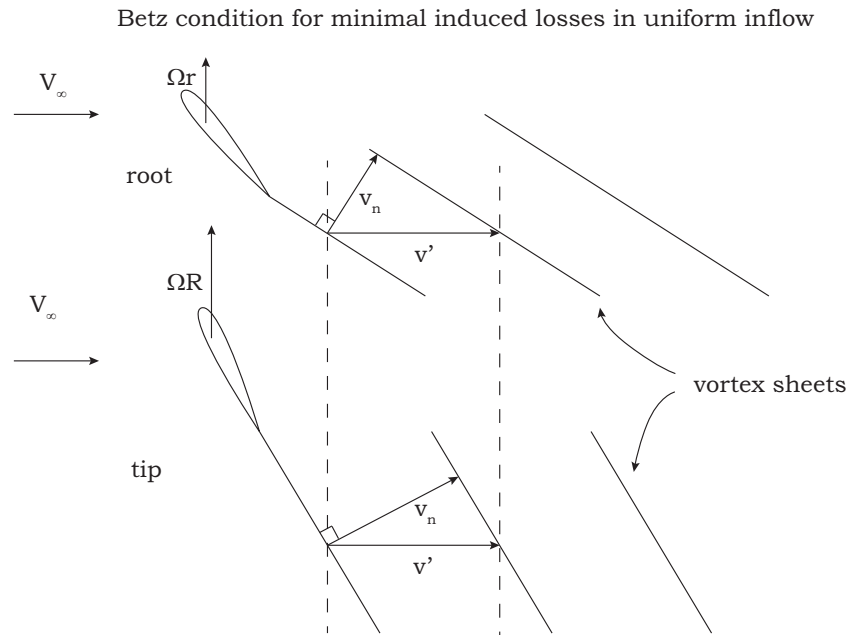


Figure 2.7: Betz' condition of minimal induced losses for a propeller with uniform inflow. The vortex sheets have a constant axial displacement velocity  $v'$  over the radius.

Now consider non-uniform inflow. As shown in section 2.1 the maximum efficiency of a uniform inflow propeller reduces with reducing axial velocity. This may indicate that the local efficiency along the blade also varies. Analogously with the momentum analysis in section 2.1, a blade with a varying axial velocity along the radius may be expected to have a low efficiency in the low axial velocity regions but these regions have a high ratio of  $\frac{dT}{dQ\Omega}$ .

If the quantity  $\frac{dTV_\infty}{dQ\Omega} = c$  in which  $c$  is a certain constant but is a to be determined value, one can rewrite this to:

$$\begin{aligned}\frac{dTV_\infty}{dQ\Omega} &= c \\ \frac{dTV_a}{dQ\Omega} \frac{V_\infty}{V_a} &= c \\ \frac{dTV_a}{dQ\Omega} &= c \frac{V_a}{V_\infty}\end{aligned}\tag{2.12}$$

A similar result is found when the vortex sheets do not move backward with a constant speed relative to each other but relative to the free stream flow,  $V_a + v' = c$  (in which  $c$  is a constant and not equal to equation 2.11). In that case, the local efficiency  $\eta_{local}$  can be written as

$$\begin{aligned}\eta_{local} &= \frac{\tan \phi'}{\tan \phi} \\ &= \frac{V_a}{V_a + v'} \\ &= \frac{V_a}{c}\end{aligned}\tag{2.13}$$

Several authors have proposed distributions of  $\frac{\tan \phi}{\tan \phi'}$  for radially non-uniform inflow, including Lerbs [43], Helmbold [23], Balhan and van Manen [44] and van Manen [45]. Balhan and van Manen [44] found the same distribution as in equation 2.12. Lerbs found a distribution of  $\frac{\tan \phi}{\tan \phi'}$  (or local efficiency) by using the same principle as Munk did for uniform inflow propellers by using small variations of  $\Gamma_B$  along the blade. Lerbs neglected the higher order terms which arise from the induced velocities. These authors included a term to correct for the velocity at the propeller tip, which is not necessarily equal to  $V_\infty$ .

To indicate that the optimal efficiency distribution is not constant but rather has a decreasing value towards the root, a numerical method can be used. A very simple and quick analysis of a non-uniform inflow and its efficiency distribution leading to the lowest power can be done using a non-uniform Actuator Disk. When the following quantities are set a-priori:  $R$ ,  $R_{hub}$ ,  $V_a(r)$  and  $T_{shaft}$ , one can vary the axial induced velocity along the blade and calculate the total thrust and power using momentum theory. The distribution of  $V_{i,a}$  is varied using shape functions and a gradient based optimiser is used to find the lowest required power. A more detailed discussion on the shape functions and the optimisation algorithm is provided in section 3.4. Figure 2.8 (a) shows distributions of  $\eta_{local}$  for a non-uniform inflow field for different thrust settings. In addition, the distributions by Lerbs [43] and van Manen [45] are indicated. The corresponding radial distribution of induced velocity is shown in (b). For the flow condition, propeller geometry and thrust setting, refer to Chapter 6. The distributions of the numerically optimised solution shows a decreasing efficiency and increasing induced velocity towards the root. The trends follow the predicted curve by Lerbs [43] fairly well but at higher thrust settings the curve of van Manen [45] is approached. The curves show that in the tip region the induced velocity is (close to) zero as in that region the thrust to power ratio is relatively high. Another observation is that the shape of the curves change with thrust setting. It should be stressed that this highly simplified analysis does not include tip losses, hub effects, tangential velocities, the effect of the induced field of neighbouring sections and limitations with respect to the airfoil properties. These results should only be considered as illustration. Because there is no definite optimal distribution found for non-uniform inflow, there is no distribution prescribed in this thesis.

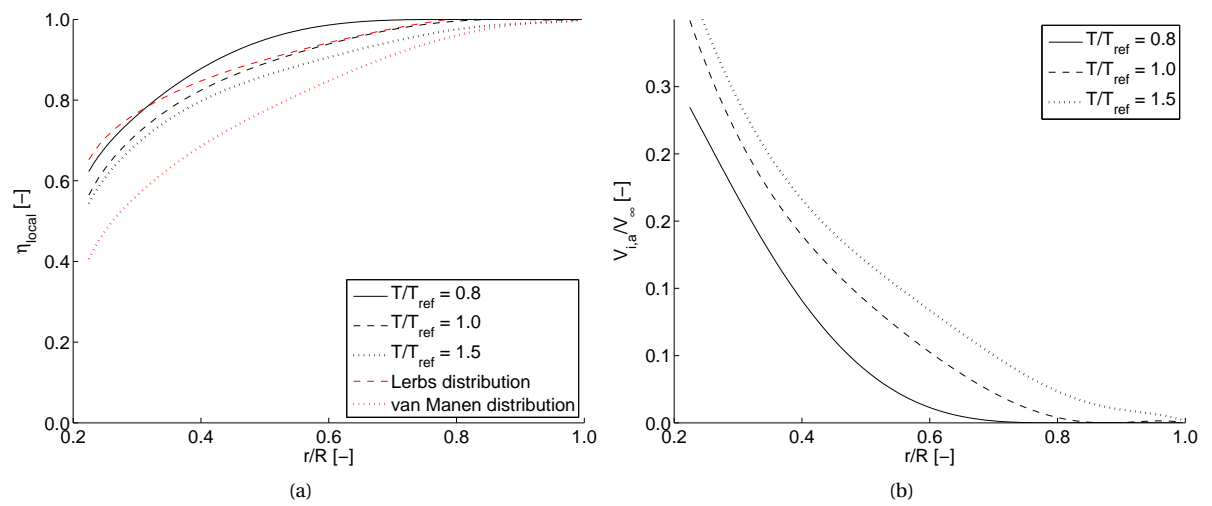


Figure 2.8: In black: results from an optimisation of an Actuator Disk with radially non-uniform inflow with different thrust settings. The distribution of axial induced velocity is the design vector. For the inflow condition, disk area and thrust setting, refer to Chapter 6. In red the distributions of efficiency as proposed by Lerbs [43] (dashed) and van Manen [45] and equation 2.12 (dotted). Due to the simplification of the propeller representation, these results should only be considered as illustration of the efficiency distribution.



# 3

## N-XROTOR: PROPELLER DESIGN TOOL FOR NON-UNIFORM INFLOW

In this chapter the propeller analysis tool using a non-uniform inflow and the optimisation routine is discussed. First the choice for the propeller analysis method is explained in section 3.1. Section 3.2 explains the analysis tool followed by section 3.3 which discusses the assumptions related to the inflow. The optimisation routine and a test case is discussed in sections 3.4 and 3.5 respectively.

### 3.1. CHOICE OF PROPELLER ANALYSIS METHOD

Various propeller analysis methods exist to calculate the performance of a propeller subject to a non-uniform inflow with different levels of accuracy. The choice for the particular analysis method is based on a number of requirements, including:

- The method should be able to use a non-uniform profile in axial direction as inflow and should account for the accompanying local aerodynamic effects of this reduced flow.
- The propeller should have any (feasible) shape including a finite hub radius, varying chord and pitch angle distributions and the airfoil properties should be taken into account.
- The computation time should be in the order of seconds to minutes per operating condition in order to be used inside an optimisation loop.
- The setup of a single analysis point should allow for an implementation such that limited involvement of the user is required.
- The precision of the performance quantities should be such that an optimisation algorithm can distinguish a search direction and an optimum.
- It is preferred that the method is implemented in a tool which has been used by others and is available to be used for this thesis.
- For comparison purposes the tool should be able to include compressibility effects of a moderate helical tip Mach number, but there is no priority to model transonic effects.
- The method does not necessarily require to have the capability to analyse swept propellers because it is shown in Succi [46] and Miller and Sullivan [30] that sweep is especially of interest for noise reduction, which is not part of this thesis.

The requirement of a limited computation time per operating point and geometry excludes the use of Computational Fluid Dynamics (CFD) as analysis tool in the design process. Both the setup of a CFD simulation in terms of mesh generation and the analysis itself requires a significant amount of computational resources and is not suited to be used in an optimization routine. Therefore the choice of analysis methods is limited to lower order methods methods.

Lifting surface methods such as the Vortex Lattice Method (VLM) are lower order methods as they are potential flow methods. The lifting surface is divided into elements with control points and at the surface or at the mean camber line the potential flow is solved. The contribution of profile drag can be added using airfoil data to improve the prediction of the torque calculation [47]. The variation of the induced velocity over the chord which results in a virtual change in effective angle of attack is captured by lifting surface methods

and therefore relatively low aspect ratio propeller can be analysed [40, 48]. As the shape of the propeller is taken into account, lifting surface methods are able to analyse swept propellers [47].

Other lower order methods include Blade Element (BE) methods which are popular because of their simplicity, accuracy and their low computational cost [49, 50]. BE models are based on dividing each blade into small segments and the two-dimensional aerodynamic loads are calculated based on effective inflow velocity and two-dimensional data for  $C_l$  and  $C_d$ . A summation over all the segments determines the total thrust and power of the propeller. The calculation of the induced velocities at the blade can be done in various ways. One of the methods is using momentum theory, in which the propeller disk is divided in cellular rings and momentum theory is used to find the induced velocities. This method neglects the loading of the neighbouring sections of a section at location  $r$  which affect the induced velocity at that position. A finite number of blades shed a finite number of vortex sheets (depicted in figure 2.4). Around the edge of the vortex sheet the flow tends to flow around the edge causing a significant radial flow component. This component is especially present for a low number of blades. In BEM models, a correction should be made to account for this effect. Prandtl [42] estimated this effect with a 'tip loss factor' which can be used to correct for the finite number of blades. However, using such model prescribes part of the radial loading distribution.

Another method are lifting-line methods in which a high aspect ratio lifting surface is represented by a vortex filament (the bound circulation  $\Gamma_B$ ) along the quarter chord line. Because there is only one vortex per radial location, the variation of circulation in chordwise direction is neglected. Contrary to a BE method based on momentum theory, the lifting line method does take the contribution of neighbouring blade elements into account in the induced velocity computation. In Schulten [47] several variations of lifting surface methods and lifting line methods are compared with experimental results of the unswept SR-2 propeller which has a moderate aspect ratio. The lifting surface showed only marginally better results at moderate advance ratios compared with a lifting line code. Because the ability to analyse swept propellers is not a priority, the lifting line method is considered to be a valid method to analyse propeller geometries for design and comparison purposes.

A fast analysis tool which does comply with the above mentioned requirements is the program XROTOR by Mark Drela [1] which has been used by a number of authors [24, 32, 51–53] for uniform and non-uniform inflow and is a common tool used within the Faculty of Aerospace Engineering at the Delft University of Technology. The capabilities and limitations of XROTOR including its implementation in a complete propeller analysis tool is discussed in the next section.

## 3.2. N-XROTOR: PROPELLER LIFTING LINE CODE

The software developed for this thesis is named N-XROTOR and is a collection of Matlab functions and external programs which can be used inside an optimisation loop as well as an isolated propeller analysis program. For the latter operation a small amount of code is required to interact with N-XROTOR. Figure 3.1 shows a schematic of the flow of the program. The program consists of four main modules; a definition module, an aerodynamic module, the propeller analysis module and a post-processing module. First the definition of the propeller geometry in terms of  $c/R$ ,  $\beta(r)$ ,  $R$ ,  $R_{hub}$ ,  $B$  and  $\Omega$  (or  $J$ ) should be specified. In addition, the flow condition in terms of  $V_\infty$ ,  $V_a(r)/V_\infty$  and properties such as  $\rho$  are required as input. Furthermore some computational settings and plotting settings should be set. The aerodynamic module is called to generate airfoil data for each radial position (elaborated in section 3.2.2). The airfoil data is analysed and provided to the propeller analysis module which calculates the propeller performance quantities and radial distributions. The results are then processed to provide useful output. The following sections give a more detailed overview of each module.

### 3.2.1. XROTOR

The core of N-XROTOR is the propeller analysis software XROTOR developed by Drela [1]. XROTOR is a lifting line code which iteratively calculates the circulation distribution, induced velocity field at the lifting line and the thrust and power using airfoil properties.

The velocity at the propeller lifting line is calculated from the bound vortex and discrete line vortices on the rigid helicoidal wake surface which trails from the lifting line into the far-field downstream. The direction of this vortex sheet needs to be known in order to calculate the induced field. There are three frequently used methods to describe the direction of the vortex sheet from the lifting line; a prescribed wake model, a semi-rigid wake model and a free wake model. In a pre-scribed wake model the sheet is assumed to follow the known quantity  $\phi'(r)$  and will therefore not change during the calculation. A semi-rigid model iteratively

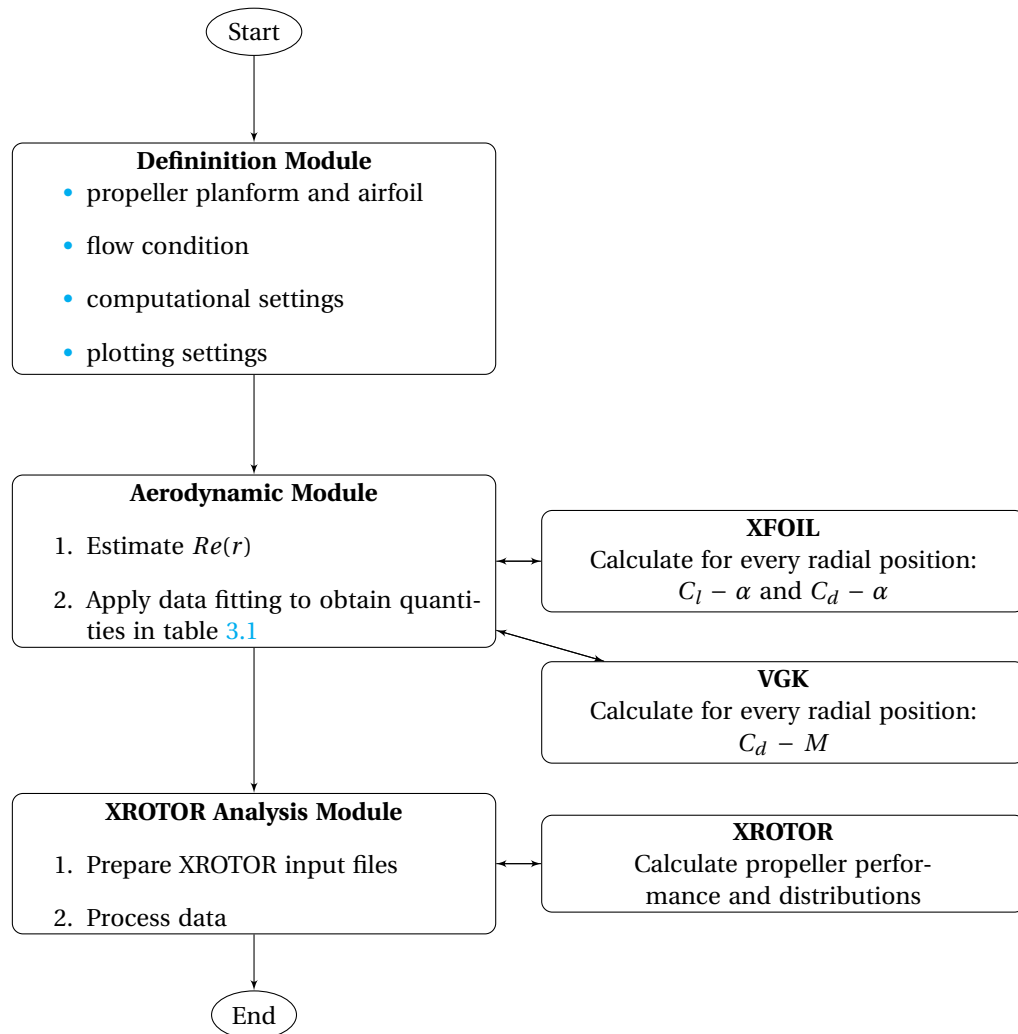


Figure 3.1: Overview of N-XROTOR sequence. N-XROTOR is a Matlab function which requires a 'main' function to be operated. The 'Start' and 'End' blocks are therefore not part of N-XROTOR but merely serve as an indicator for the flow of the program.

calculates the direction of the trailing vortex sheet which ignores wake contraction and wake roll-up but includes the induced velocities. A free wake model calculates the complete geometry of the vortex sheet from the lifting line. This method is not included in the XROTOR program and therefore the semi-rigid wake is used. The effect of a semi-rigid wake compared with a free wake model has shown not to be significant for moderately loaded propellers [40]. The assumption of a constant slipstream radius is indicated in Durand [10]. The contraction of the slipstream is a direct result of the increased axial velocity. As there is no dissipation modelled, the circulation remains constant in the slipstream. A ring of fluid at radius  $r$  has a circulation of  $2\pi V_{i,t} r^2$ . Downstream the radius of this ring is decreased due to contraction and therefore the tangential induced velocity is increased. However it is expected that this has limited impact on the propeller performance.

The XROTOR code is compiled by the author for Windows operating systems and a few minor changes have been applied to the original XROTOR code. The performance outputs of the default XROTOR code have a precision of three significant numbers. The code has been changed by such that the outputs have a precision of six significant numbers which is more favourable in optimisation routines when a search direction has to be determined. In addition, some velocities slipstream velocities have been added to the default output file.

Airfoil section properties are required to compute the induced velocities and forces at each blade section. XROTOR uses a number of airfoil parameters (summarised in table 3.1) to construct the section  $C_l - \alpha$  and  $C_d - C_l$  curves including a relatively good prediction of the airfoil stall properties. These curves are used in XROTOR to quickly calculated airfoil properties during the iterations. The critical Mach number is required

Table 3.1: Airfoil properties required as input for XROTOR.

Quantity	Description
$C_{d,0}$	Minimum drag coefficient
$Re_{ref}$	Reference $Re$ at which drag data is computed
$\frac{dC_d}{dC_l^2}$	Derivative of $C_d$ to $C_l^2$
$C_{l,0}$	Lift coefficient at $C_{d,0}$
$\alpha_0$	Angle of attack at $C_l = 0$
$f$	Exponent to express effect of Reynolds number on drag curve [1]
$M_{crit}$	Drag rise Mach number
$k[-]$	Scaling factor [1]
$n$	Exponent to express drag rise as function of $M$ [1]
$C_{l\alpha}$	Lift curve slope
$C_{l,max}$	Maximum lift coefficient
$\Delta C_{stall}$	$C_{l,max} - C_{l,non-linear}$

which for propeller may be an important factor for high helical tip Mach numbers.

XROTOR uses the Prandtl-Glauert compressibility correction for the  $C_{l\alpha}$  and accounts for Reynolds effects and drag rise at Mach numbers beyond the critical Mach number on the  $C_d$  by making use of equation 3.1 [1]. The equation corrects for the Reynolds effect using an exponent  $f$  in the case that the particular airfoil experiences a different  $Re$  than the reference value at which  $C_d$  is computed. In principle one could compute the airfoil data at one  $Re_{ref}$ , but a closer estimate of the airfoil data is at the correct  $Re(r)$ . In this way also estimates for  $C_{l,max}$  and  $C_{l\alpha}$  correspond to the local section.

$$C_{d,XROTOR} = [C_{d,0} + b(C_{l,0} - C_l)^2] \left( \frac{Re}{Re_{ref}} \right)^f + k(M - M_{crit})^n \quad (3.1)$$

The consequence of using such a quadratic relation for the  $C_d$  is that it does not capture a different  $C_d - C_l$  behaviour which might be unique to a certain airfoil geometry. In e.g. Abbott and von Doenhoff [54] it is shown that the  $\alpha - C_d$  (and consequently also  $C_l - C_d$ ) is not necessarily a quadratic relation. Especially cambered airfoils have a relatively flat  $C_d - C_l$  curve for a range of lift coefficients and their benefit is not correctly captured with a quadratic relation as implemented in XROTOR.

### 3.2.2. AIRFOIL SECTION DATA

There are different methods to predict two-dimensional airfoil data ranging from CFD to panel methods. As noted in Chapter 6 the airfoil geometry is included in the design optimisation and each iteration new airfoil data is computed. Therefore a fast analysis method is required with acceptable accuracy and flexibility. Two-dimensional data computed with CFD generally requires a significant amount of computational resources, especially when the shape of the airfoil is changed during the optimisation and a new mesh should be (automatically) generated. The use of high-fidelity tools can typically be employed in a final design phase of a propeller and as verification of the method. For comparison purposes and initial performance computations, lower fidelity tools are preferred.

A combination of the analysis tool Viscous Garabedian and Kern (VGK) [55] and XFOIL [2] is selected for the analysis of arbitrary airfoil shapes. VGK is a Fortran code which predicts two-dimensional airfoil data using an iterative approach to solve coupled finite-difference equations for the inviscid flow region and integral equations for the viscous region. VGK is suited to analyse airfoils at transonic flows and has been thoroughly validated by several authors (e.g. Cheung [55]) at various Reynolds and Mach numbers. The advantage of VGK is that it can calculate section properties at relatively high Mach numbers and is therefore used to calculate the value of  $M_{crit}$ . However, the default code can not predict the airfoil properties at and close to stall. Therefore XFOIL is used to construct the main aerodynamic properties as it can predict stall behaviour which is an important phenomena to take into account. In XFOIL the transition from a laminar to a turbulent boundary layer is predicted using the  $e^N$  method by van Ingen [56]. The critical amplification factor  $N_{crit}$  is based on a number of flow field parameters and external excitations. The prediction of transition on propeller blades is a detailed field of study due to the extra rotational accelerations and three-dimensional flow over the propeller blade [57, 58] and does not receive special attention in this thesis. Only 2D transition is considered. A useful property of the  $e^N$  method is the relation of the turbulence level [56] with respect to the freestream velocity:

$$Tu = \frac{\sqrt{\frac{1}{3}(u'^2 + v'^2 + w'^2)}}{V_{eff}} \quad (3.2)$$

The value of  $Tu$  is changing through the boundary layer [59] which is also shown in Chapter 5 with values requiring a low  $N_{crit}$ . For the computation of the airfoil data for the propeller in the boundary layer a relatively low  $N_{crit} = 0.01$  is chosen for all radial positions because of two reasons. First XFOIL has shown to be reasonably stable at this value and significantly higher or lower values can lead to a non converging solution. Secondly, as indicated in Chapter 4, the results of the CFD simulation are computed with a fully turbulent boundary layer and therefore it is considered to improve the comparability of the output of N-XROTOR and the CFD simulations when transition occurs close to the leading edge. In section 4.3 the effect of 2D transition on propeller performance is shown for an undisturbed uniform inflow propeller.

An arbitrary airfoil geometry is used as input for XFOIL. For a range of angles of attack the  $C_l - \alpha$ ,  $C_d - \alpha$  and  $C_l^2 - C_d$  curves are constructed with a sufficient number of analysis points. In some angle of attack and airfoil combinations, XFOIL does not converge for a certain angle of attack while both smaller and larger  $\alpha$  do lead to a converged solution. The implementation is done such that these non-converged solutions do not lead to a termination of the program and are excluded from the airfoil data set. The non-linear part of the lift curve for a propeller section is underpredicted in a 2D analysis due to three dimensional effects. Three-dimensional effects includes centrifugal forces on the boundary layer which is pronounced for separated flow [57]. A Coriolis force is acting on the flow with  $V_r \neq 0$  stabilising the boundary layer and hence a higher maximal lift coefficient is obtained at a higher angle of attack. This Coriolis force is the driving force for separated flow (where the chordwise pressure gradient is essentially zero). Therefore the non-linear part of the lift curve is corrected using an empirical model. An overview of methods which correct the  $C_{l,2D}$  is provided in Lindenburg [60] and Snel et al. [57] and are generally based on empirical models. In N-XROTOR a model by Snel et al. [57] is chosen and given in equation 3.3 in which  $A$  and  $B$  are scaling components:

$$C_{l,2D,rot} = C_{l,2D} + \tanh \left[ A \left( \frac{c}{R} \right)^B \right] (C_{l,lin} - C_{l,2D}) \quad (3.3)$$

The local Reynolds and Mach number at each radial location on the blade vary because of variable chord length and magnitude of effective velocity. Because  $C_d$  and to a lesser extend also  $C_l$  depend on  $Re$ , the airfoil data is generated for each radial location at the corresponding flow condition. Because the compressibility effect on the lift coefficient and Reynolds effect are uncoupled [54], the airfoil data is computed for an incompressible flow at the Reynolds number present at the particular radial position. The local  $Re(r)$  depends on  $\Omega r$ ,  $V_a(r)$  and the induced velocity field. However, the local Reynolds number is estimated using a  $V_{eff} \approx \sqrt{V_a^2 + (\Omega r)^2}$ .

### 3.3. SIMPLIFICATION OF THE INFLOW PROFILE

It is required to make a number of simplifications with respect to the inflow of the propeller which is simulated in N-XROTOR because of the assumptions used by the lifting line method. This section provides an overview of these simplifications.

The most important assumption for the analysis of the integrated propulsor is that the flow field induced by the propeller and the flow field induced by the fuselage are decoupled. This assumption is linked to the potential flow theory in which two solutions of the velocity potential and therefore velocity may be added to obtain the complete solution, as is indicated in e.g. Anderson [61]. The induced velocities and pressures by the fuselage develop downstream and the induced flow field of the propeller is added. The induced upstream effect of the propeller as discussed in section 2.3 is approximated in section 5.4 and therefore is taken into account. The assumption of isolating the flow field of the propeller, the assumptions related to the lifting line method and assumptions set by the author lead to the following constraints on the flow field description:

- The contraction of the aft fuselage induces a radial flow component at the plane of the propeller (sketched in figure 3.2). The radial component with respect to the local axial flow is pronounced towards the propeller hub. This radial flow components is neglected by the limitations of the lifting line method and only the axial flow component of the boundary layer is used in the calculation.
- At the wall the (axial) velocity is 0 [m/s] due to the no slip condition. A velocity of 0 [m/s] does not lead to a converged solution by N-XROTOR. Therefore a finite velocity is taken at the propeller root

by simulating a part of the fuselage as a slip wall, which essentially 'releases' the boundary layer as sketched in figure 3.2. This is discussed in Chapter 5.

- The pressure at the location of the propeller is not equal to freestream conditions due to the presence of the fuselage. This effect is not taken into account.
- The effect of the axial and radial pressure gradient induced by the fuselage is not taken into account. The effects of these pressure gradients are discussed in section 4.3.
- The turbulence intensity is considered to be constant along the radius and is considered relatively high such that there is a primarily turbulent boundary layer on the airfoil and enhances the stability of the XFOIL program.
- Because there is a body upstream of the propeller it effectively limits the propeller to induce an axial flow. This blockage effect is not taken into account.

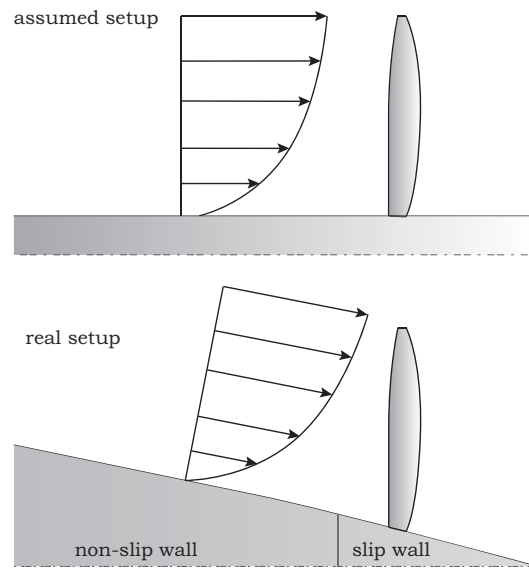


Figure 3.2: Comparison of the CFD setup with a boundary layer parallel to the tapered aft fuselage and the assumed setup with only the axial component of the boundary layer and no tapered spinner/hub.

### 3.4. DESCRIPTION OF OPTIMISATION PROBLEM

This section describes the structure of the optimisation setup. The actual optimisation for the non-uniform inflow and uniform inflow is performed in Chapter 6.

#### 3.4.1. OPTIMISATION SETUP

A design procedure which is used by a large number of authors is to first determine the optimal circulation distribution for minimum induced losses and then determine the blade geometry in terms of the blade pitch and chord distributions and the airfoil properties. It is shown by Klesa [62] that the optimal circulation distribution for the sum of induced losses and profile drag is not equal to the distribution for minimum induced losses only. Therefore an approach is chosen in which both the airfoil and propeller planform is optimised at the same time.

Because of the number of variables, their complex interaction and a number of non-linear constraints an algebraic solution procedure is not straight forward. Therefore the optimisation of the propeller shape is done using a numerical optimisation method. This leads to the choice of two main groups of optimisation procedures; gradient based optimisation and other methods such as genetic algorithms. A genetic algorithm has the advantage that there is a greater probability that a global minimum is found instead of a local minimum. However, it takes a relatively large number of iterations to reach a minimum. Gradient based methods

may have difficulties in finding a global minimum but generally converges faster than the genetic algorithm. Therefore a gradient based method is selected and different initial design vectors are used to increase the chance of finding a global optimum.

The general description of the optimisation is to minimise the objective function  $J(\bar{x})$ . The choice of the objective function is a minimal required power  $P$  for all optimisations discussed in this thesis. The minimisation problem is subject to non-linear equality and inequality constraints  $h(\bar{x})$  and  $g(\bar{x})$  respectively:

$$\begin{aligned} J(\bar{x}) = \text{minimise } P(\bar{x}) \text{ subject to} \\ h(\bar{x}) = 0 \\ g(\bar{x}) \leq 0 \end{aligned} \quad (3.4)$$

The design vector is discussed in the next section and the constraints are discussed in section 3.4.3. Matlab provides a number of optimisation toolboxes including 'fmincon' for constrained optimisation. This function is used for its flexibility.

A schematic of the optimisation process is shown in figure 3.3. A parallel optimisation setup is used to allow for relatively fast optimisations. Because N-XROTOR uses the same executables of XFOIL and XROTOR, a unique identifier is provided to each data file such that these files are linked to the correct design vector. Note that there is no feed back of the upstream and downstream effects of the propeller on the fuselage drag into the optimisation routine, i.e. the design condition is not changed during the optimisation.

### 3.4.2. DESIGN VARIABLES

The geometry is characterised by the distribution of  $\beta(r)$ , the distribution of  $\frac{c}{R}(r)$ , airfoil contours, the radius  $R$  and the hub radius  $R_{hub}$ . The latter is a given value for a given propeller location and is therefore not considered as a design variable. The value of  $R$  can be chosen to be equal to the boundary layer thickness or a fraction of this value. The propeller geometry is parametrised such that with a limited number of design variables a wide range of propeller geometries can be obtained with a smooth shape.

Both the chord and pitch distributions consist of a linear distribution with a value at the root and a value at the tip and an intermediate distribution as shown in figure 3.4 (a). The intermediate distribution is described with the method from Kulfan [63] in which a shape function and Class Shape Transform (CST) coefficients are used. A non-dimensional coordinate  $\zeta$  with  $\zeta = 0 \dots 1$  is used as the radial location with  $\zeta = 0$  at the propeller hub. The non dimensional function value  $\Psi$  represents either a value for  $\beta$  and  $\frac{c}{R}$ . The non linear intermediate distribution is then given in equation 3.5 in which  $\bar{A}$  are the CST coefficients. This distribution is then mapped to the hub to tip region. The values of  $N1$  and  $N2$  represent a measure of the gradient at the root location and tip location respectively and vary between 0.5 and 1. The effect of these exponentials and the coefficients  $A_{i \dots n}$  on the intermediate distribution is illustrated in figure 3.4 (b) and it is shown that a wide range of shapes can be constructed.

$$\zeta = \Psi^{N1} (1 - \Psi)^{N2} \sum_{i=0}^N A_i \Psi^i \quad (3.5)$$

The airfoil contour could also be described using CST coefficients. However, a lower number of variables describing the airfoil is preferred. Therefore the NACA 4-series airfoil geometry is used for the airfoil description. The upper and lower surface distributions are a function of the maximum camber  $m$ , the location of the maximum camber  $p$  and the maximum thickness  $t$ . The airfoil geometry descriptions can be found in e.g. Abbott and von Doenhoff [54] and are not repeated here. To simplify the analysis and to limit the number of design variables, a single airfoil is used along the radius. The effect of using only one airfoil is discussed in Chapter 6. The location of the maximum thickness is set to 30% of the chord length to reduce the number of airfoil parameters to two.

As the design variables are not necessarily of the same order, the variables are normalised with respect to their initial value. This ensures that the sensitivity of the variables with respect to the objective function is not influenced by their absolute values. Table 3.2 lists the design variables.

Appropriate initial reference values are important for convergence of XROTOR and XFOIL. When N-XROTOR does not converge because the initial design vector represents an unrealistic design, the optimiser might experience difficulties in finding a solution. One of the values which is dependent on the operating condition is the  $\beta_{root}$  and  $\beta_{tip}$ . It is suggested that these angles, at least for symmetric airfoils, are equal to or larger than the local flow angle  $\phi'$ . Therefore their value is based on this local flow angle as the reference value. For

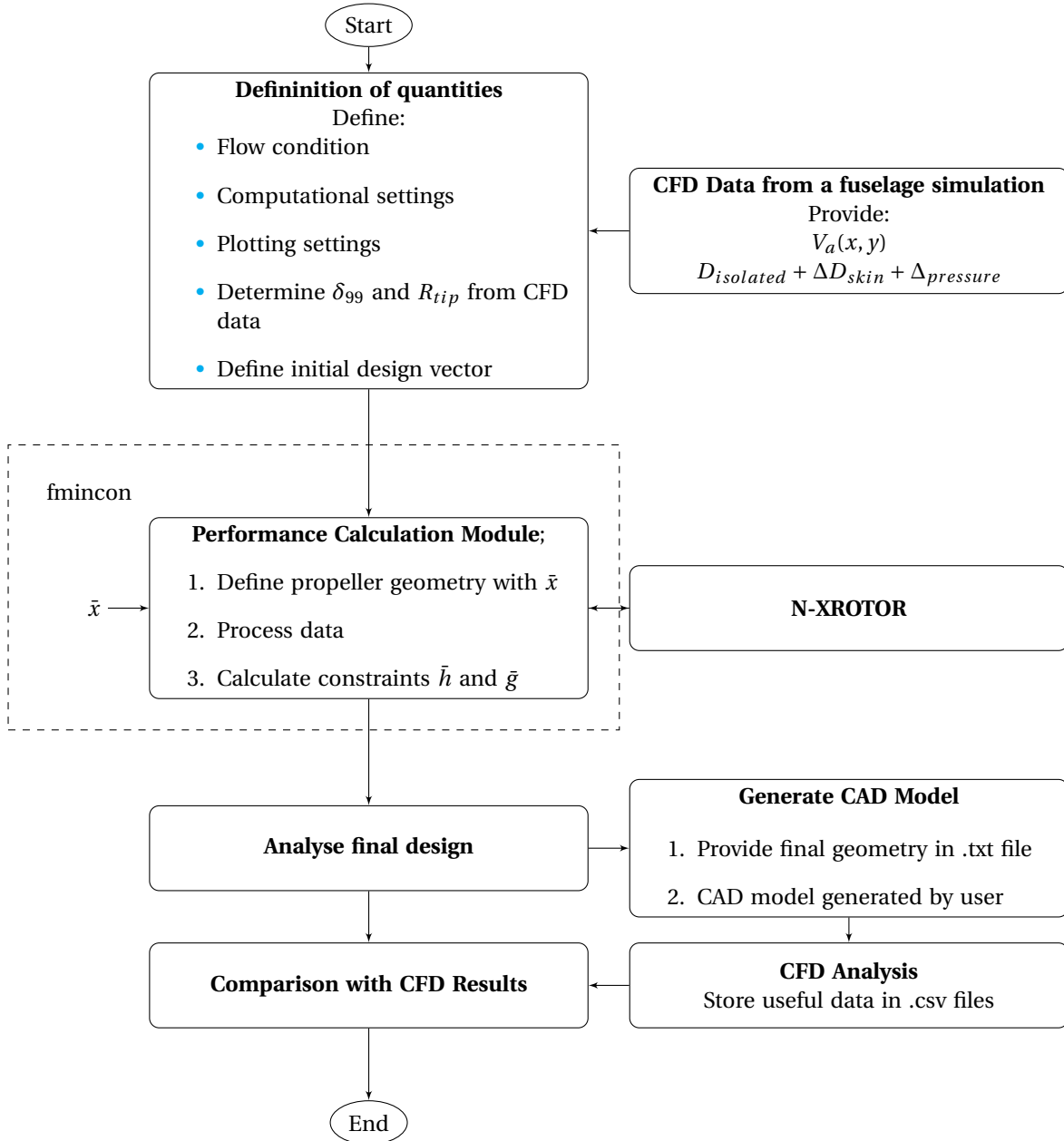


Figure 3.3: Overview of optimisation sequence in which the use of CFD is indicated.

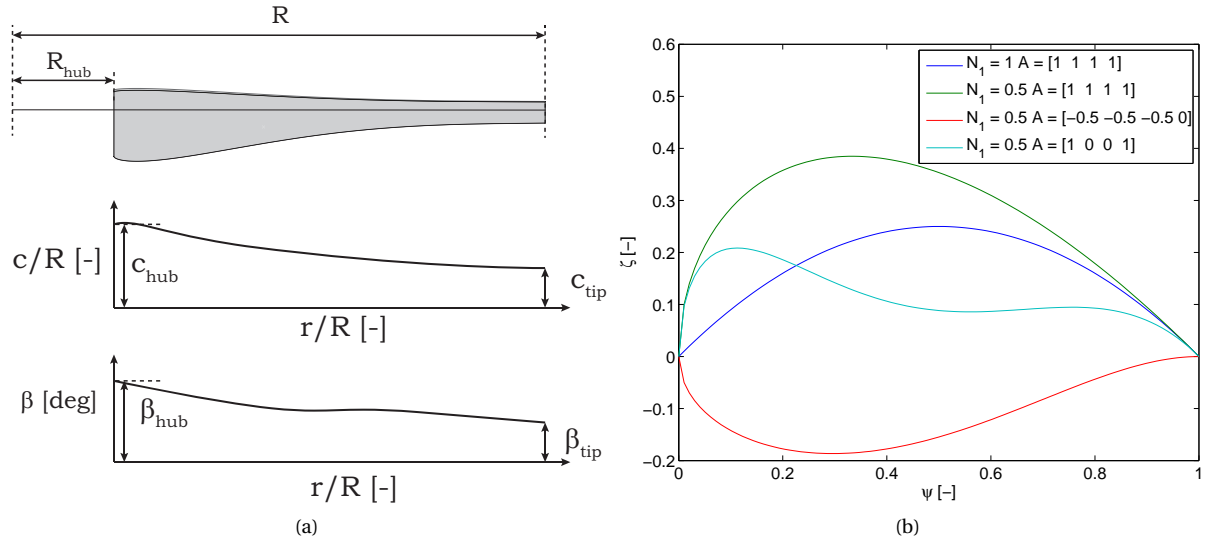


Figure 3.4: The definition of the propeller geometry in (a) using a hub and tip value of the  $\frac{c}{R}$  and  $\beta$  with an intermediate distribution. This distribution is constructed using shape functions in which several examples are shown in (b)

the other reference values, first an optimisation is performed without airfoil data to approximately estimate a distribution which provides a reasonable propeller geometry with relatively low computational resources. This is used as a starting condition for the optimisation including airfoil shape parameters.

### 3.4.3. CONSTRAINTS

There are a number of equality constraints ( $\bar{h} = 0$ ) and inequality constraints ( $\bar{g} \leq 0$ ) implemented for a number of reasons: to describe the design condition, to constrain the optimiser from non smooth geometries and to avoid unwanted effects such as trailing edge stall at some radial locations for the design condition.

The first equality constraint  $h_1$  is to ensure that the thrust of the propeller balances the drag force of the fuselage, as defined in equation 2.7, and should therefore be equal to a reference thrust  $T_{ref}$ . This is the design condition which is different for the (isolated) uniform and (integrated) non-uniform inflow propellers.

$$h_1 = T_{ref} - T \quad (3.6)$$

The maximum allowable deviation on this equality constraint is set to 0.1%. A smaller value results in a significant computation time and larger values are considered to be unsuited for comparison purposes. The other two equality constraints are introduced to ensure that only results are produced with both XFOIL and XROTOR converged. Convergence of XFOIL in this context means that most of the airfoil data is computed. When there is no convergence, the optimiser is setup as such that the optimisation will continue, but the equality constraint(s) get(s) a finite value:

$$h_2 = 0 \quad \text{if XFOIL is converged, else} \\ = 1 \quad (3.7)$$

$$h_3 = 0 \quad \text{if XROTOR is converged, else} \\ = 1 \quad (3.8)$$

The inequality constraints  $g_1$  and  $g_2$  are related to the geometry. The optimisation routine may provide a geometry (chord and pitch angle combination) that is not feasible because (1) it may be insensitive to local flow effects near the tip and (2) because two combinations of  $\frac{c}{R}$  and  $\beta$  can yield nearly similar results in terms of  $dT$  and  $dQ$  of which only one combination is desired. In general, rapid changes in geometry near the root and the tip result in structural problems which should be avoided. Therefore a decreasing  $\beta(r)$  towards the very tip region ( $\frac{r}{R} = 0.90 \dots 1.00$ ) is set as a constraint. Also, the outer region of the propeller tip is forced to have a only decreasing  $\frac{c}{R}$  value. These constraints ensure a smooth geometry. The third inequality constraint is related to the airfoil performance. Because the prediction of the airfoil data in the non-linear  $C_l$  regime

Table 3.2: List of design variables, their reference values and their upper and lower bounds

Vector index	Variable	Reference value $x_{ref}$	Upper bound	Lower bound
$x(1)$	$\frac{c}{R}$ CST coefficient	0.25	0.00	1.5
$x(2)$	$\frac{c}{R}$ CST coefficient	0.25	-0.5	1.5
$x(3)$	$\frac{c}{R}$ CST coefficient	0.25	-0.5	1.5
$x(4)$	$\frac{c}{R}$ $N_1$ coefficient	1.00	0.50	1.0
$x(5)$	$(\frac{c}{R})_{root}$	0.15	0.40	1.5
$x(6)$	$(\frac{c}{R})_{tip}$	0.10	0.40	2.0
$x(7)$	$\beta$ CST coefficient	1.00	-1.0	3.0
$x(8)$	$\beta$ CST coefficient	1.00	-1.5	3.0
$x(9)$	$\beta$ CST coefficient	1.00	-1.5	3.0
$x(10)$	$\beta$ $N_2$ coefficient	1.00	0.5	1.0
$x(11)$	$\beta_{root}$	1.00 $\beta_0$	0.8	2.0
$x(12)$	$\beta_{tip}$	1.00 $\beta_0$	0.8	2.0
$x(13)$	$t$ airfoil thickness	0.06	0.7	1.5
$x(14)$	$m$ airfoil camber	0.04	0.0	2.0
$x(15)$	$R$ (if applicable)	$\delta_{99}$	0.8	1.5

is relatively uncertain, for the design condition it is preferred to have a  $C_l(r)$  distribution which is still in the linear lift curve slope regime and therefore constraint  $\bar{g}_3$  is implemented.

$$g_1 = \beta_{tip} - \beta_{1\dots N-1} \quad (3.9)$$

$$g_2 = \frac{c}{R_{tip}} - \frac{c}{R_{1\dots N-1}} \quad (3.10)$$

$$g_3 = C_{l,nonlinear} - C_l \quad (3.11)$$

### 3.5. REFERENCE CASE: OPTIMISATION FOR UNIFORM INFLOW

This section describes the results from the optimisation routine for a propeller with uniform inflow. The relevance of these results is that the theory of optimal propeller performance of a uniform inflow propeller without profile losses is well established which makes the uniform flow case a relevant test case for the optimisation routine. This test case provides insight in how well the setup performs.

For comparison purposes the operating conditions are similar to the operating conditions established in Chapter 5. These conditions are used in the remainder of the thesis to compare the performance of the uniform and non-uniform inflow propellers. In this optimisation the following design condition is prescribed:

- $V_\infty = 70$  [m/s].
- $R = 0.2404$  [m],  $R_{hub} = 0.053$  [m] and the tip advance ratio  $J = 1.50$
- $T = D_{isolated} = 74.20$  [N].
- The number of blades is set to 2
- Standard atmospheric conditions are used.
- Only induced losses are taken into account (i.e.  $C_d = 0$ ).

It has been checked that different initial conditions lead to the same converged design vector. The values of the design vector range 0.15 to 1.5 which indicates that the normalised variables have the same order of sensitivity to the objective function. The efficiency distribution of the optimised propeller is shown in figure 3.5. The figure shows an almost constant distribution of efficiency, which is in line with the theory of Betz [42], except for the tip and root region. In these regions the induced velocities computed in the lifting line tool are very large and the blade parametrisation does not allow for significant changes in geometry in these regions. However the result is an indication that the optimiser yields acceptable results.

XROTOR has a design routine to design a propeller for minimum induced losses. The inputs for this routine include  $R$ ,  $R_{hub}$ ,  $J$ ,  $V_\infty$ ,  $T$  and  $C_l(r)$  and the outputs are  $\beta(r)$  and  $\frac{c}{R}$ . The optimisation routine described in this thesis does not require a prescribe  $C_l(r)$  and therefore the results from XROTOR cannot directly be used to compare with the 'full' optimised propeller.

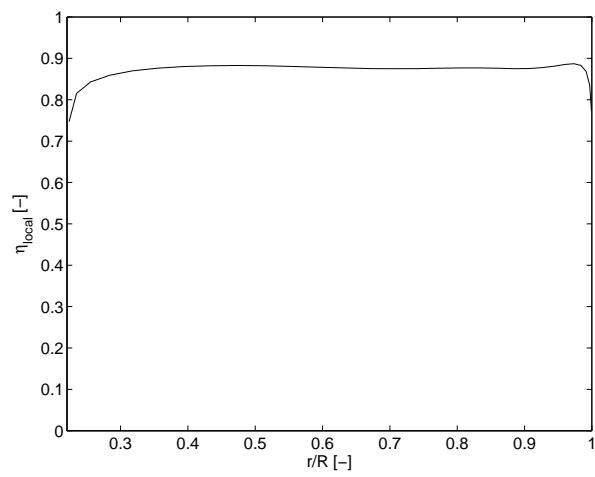


Figure 3.5: Results of a uniform inflow propeller optimisation for comparison with known distributions of such propeller. The local efficiency distribution which should be constant according to Betz [42].



# 4

## VALIDATION OF N-XROTOR FOR UNIFORM INFLOW

This chapter describes the validation of N-XROTOR using experimental results and Computational Fluid Dynamics (CFD) results. Uniform inflow propellers are compared because experimental data for non-uniform inflow propellers at relevant Reynolds numbers, flow conditions and relevant (unswept) propeller geometries is not readily available. First a comparison is made with experimental data for two reference propellers in section 4.1. A CFD analysis of the N250 propeller is performed in section 4.2 with the results being discussed in section 4.3. The purpose of these CFD simulations are to compare the results of N-XROTOR with a higher order numerical method to determine how well N-XROTOR predicts the performance of a propeller with a more complex flow than is assumed. The results will give an indication how much N-XROTOR deviates from the CFD simulations, which is important for the analysis of the non-uniform inflow propeller in CFD in Chapter 7. Also some of the findings with respect to the computational settings will be used for the CFD simulation of the non-uniform inflow propeller.

### 4.1. COMPARISON OF N-XROTOR RESULTS WITH EXPERIMENTAL RESULTS

Experimental data of the performance quantities of two reference propellers designed for uniform inflow is used to compare with results produced by N-XROTOR. The 'N250' propeller [64] and the 'NACA Prop III' [65] are considered propellers with relevant geometry and operating condition; they have unswept blades, they have moderate to high helical tip Mach numbers and have varying  $\frac{c}{R}$  and  $\beta$  distributions. The geometry descriptions of these propellers are summarised in Appendix A.

#### N250 PROPELLER

The N250 propeller has a distribution of cambered airfoils with varying airfoil sections along the radius. Figures 4.1 (a) and (b) show a comparison of the  $C_T$  and  $C_P$  respectively for different values of  $J$  and  $\beta_{0.70}$  computed with N-XROTOR against experimental data. The performance curves are computed with a constant rotational speed and standard atmospheric conditions are assumed. The figure shows that N-XROTOR predicts the trends of the thrust and power coefficients relatively good. Two observations may be made when looking at the  $C_T$  curves. For all blade angles, the lower values of  $J$  result in an over prediction of  $C_T$ . A possible cause for this could be an over prediction of the  $C_l$  at high angle of attack due to the over prediction of  $C_{l,max}$  by XFOIL or an over prediction of the lift production beyond stall. The finite chord length results in an effectively lower angle of attack compared with the lifting line because of the variation of circulation in chordwise direction, which may explain the higher slope of the  $C_T$  curve by N-XROTOR. The over prediction may also be the result of separated flow which affect unstalled sections. The slightly higher slope of the  $C_T - J$  curve for all but the smallest  $\beta_{0.70}$  could be a result of an over prediction of  $C_{l_\alpha}$  as is further elaborated in this Chapter 7. Contrary to the wind tunnel experiments, the CFD simulation of the N250 prop does not simulate a finite spinner length and consequently the additional mass flow of  $\rho V_\infty \pi R_{hub}^2$  does not flow through the propeller disk in the CFD simulation. This reduced mass flow leads to a slightly increased angle of attack in the root region in the N-XROTOR simulation compared with the experiments which may partially explain the higher predicted performance in the N-XROTOR simulation. This effect is essentially a reduction in advance

ratio. Also the  $C_P$  curve of N-XROTOR shown in figure 4.1 (b) compares relatively good with the experimental results. The trend of all advance ratios and blade angles is followed. The most distinct effect that is observed is an almost constant off-set of the power w.r.t. experimental data. The slightly larger under prediction of  $C_P$  at all advance ratios could be a result of a constant under prediction of the skin friction by XFOIL.

It should be noted that these results are computed with a  $N_{crit}$  of 5. The effect of the critical amplification factor is elaborated in section 4.3 and has shown quite significant effects on the performance. Also, it may be expected that the operating conditions do not exactly match in terms of rotational speed and velocity.

The effect of the number of radial stations on the performance quantities is shown in Appendix B in figure B.1 for a propeller discussed in section 4.1. It is shown that for approximately 60 radial sections the solution is reasonably converged and this number is chosen for all simulations.

### NACA PROP III

Evans and Liner [65] conducted wind tunnel tests on the full-scale NACA 10-(1.5)(062)-057 propeller (denoted as 'NACA Prop III') and is a two-bladed propeller with symmetrical NACA 16-series airfoil sections and a design advance ratio of  $J = 2.0$ . The chord and lift coefficient distributions were selected to meet the Betz loading distribution at the design operating condition. The operating conditions of this experiment were a constant  $\Omega$  for a varying  $J$ . Figures 4.1 (c) and (d) show the comparisons of the performance quantities with N-XROTOR. The slope of the  $C_T$  curve is very well captured for all blade angles. The constant offset may be related to the geometry and operating condition. The lag of a spinner in N-XROTOR actually causes a reduced advance ratio for N-XROTOR, which would shift the curves to a higher advance ratio relative to the experimental results. The operating condition and uncertainty in force determination may have caused a deviation. Also, when the blade is slightly twisted during the experiment due to a non zero moment coefficient, the thrust and torque are reduced in the experiment, although this is expected especially to be present at higher thrust settings, which does not explain the constant off set. The  $C_P$  curves show relatively good agreement for the higher advance ratios for all blade angles. However, the low advance ratios N-XROTOR shows an earlier non-linear behaviour than in the experiment.

## 4.2. CFD ANALYSIS OF N250 PROPELLER

As shown in section 4.1, N-XROTOR shows good agreement for the  $C_T$  over a range of advance ratios and a reasonable agreement for  $C_P$  compared with experimental data for the N250 propeller. A CFD analysis on this propeller is done because the geometry is readily available within the Delft University of Technology.

Because the calculation results depend on the domain, mesh setup and computational settings, some information is provided on the various choices related to the CFD model in sections 4.2.1 to 4.2.5. A comparison of two different computational approaches for the rotating domain (Multiple Reference Frame and sliding mesh) is performed in section 4.3.4. To limit the number of simulations only the  $\beta_{0,7R} = 27.5^\circ$  is simulated for a range of advance ratios to construct the  $C_T - J$  and  $C_P - J$  curves. The results are discussed in section 4.3.

### 4.2.1. COMPUTATION METHOD AND SOLVER

The Navier-Stokes equations describe the state of a flow and to solve these equations on a discretised domain several approaches exist. Direct Numerical Simulation solves all time and length scales. However for large meshes at relatively high Reynolds numbers, this approach requires a significant amount of computational resources [66] and is not suited for propeller design studies. For comparison studies with the relatively low fidelity tool, DNS may provide a too detailed flow description. Large Eddy Simulations (LES) models the smaller scales and calculates the larger scales. For propeller simulations, LES is generally not applicable for design studies either due to the computational cost (e.g. [67]). The main stream propeller simulation method is Reynolds Averaged Navier-Stokes equations in which the mean values of the fluctuations of all scales are modelled. This approach is used throughout all simulations described in this thesis.

The choice of a software package is limited to the availability of software at the Delft University of Technology and to the capability of simulating a rotating domain with interfaces to a stationary domain. The latter criteria is not readily available in  $SU_2$  and this software package is therefore not used. The CFD package of ANSYS™ is available and has been used for propeller simulations by several authors (e.g. [68]). This package is chosen for both setting up the mesh with ANSYS Meshing and for the flow simulations ANSYS Fluent is used.

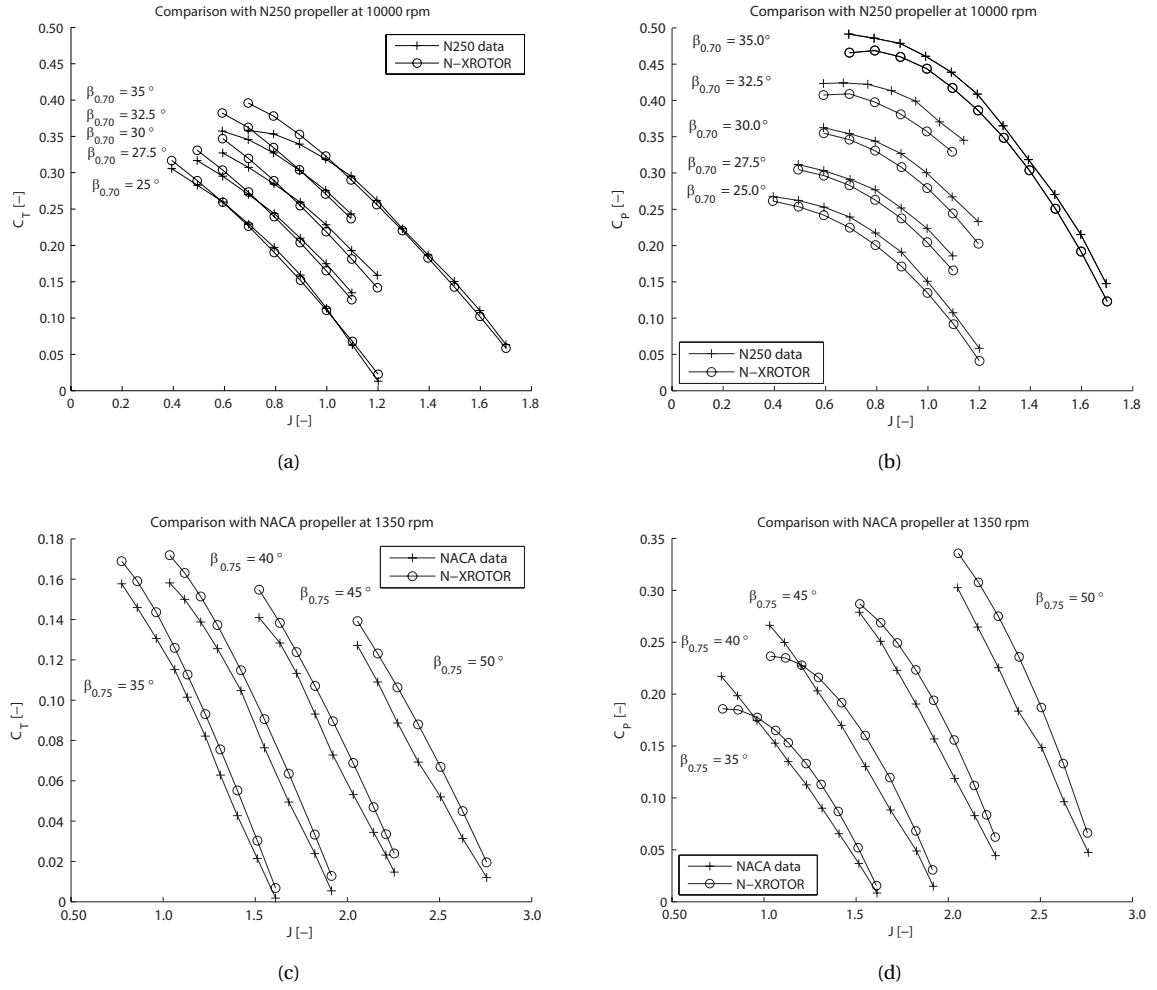


Figure 4.1: Comparison of results from N-XROTOR and experimental data of the N250 propeller in (a) and (b) and the NACA PropIII in (c) and (d) with a  $N_{crit} = 5$ . The effect of the number of radial elements used in XROTOR on the  $C_T$  and  $C_p$  of the N250 propeller at  $J = 0.79$ .

#### 4.2.2. TURBULENCE MODEL

To solve the Reynolds Averaged Navier-Stokes equations a turbulence model is required to represent the Reynolds stress tensor. An often used relation between the Reynolds stresses and the mean velocity gradients is the Boussinesq hypothesis:

$$-\overline{u'_i u'_j} = 2\nu_T S_{ij} - \frac{2}{3}k\delta_{ij} \quad (4.1)$$

where the turbulence kinetic energy  $k = \frac{1}{2}\overline{u'_i u'_i}$  and  $\nu_T$  the kinetic eddy viscosity. The terms on the right are solved using a turbulence model. The selection of an appropriate turbulence model is important for the prediction of the propeller performance for both uniform flow in the N250 simulation as well as the highly turbulent simulation of the non-uniform inflow propeller simulation. In the following paragraphs a brief discussion is provided on the selected turbulence model.

A commonly used assumption for propeller CFD simulations is a 'fully' turbulent boundary layer, such as done by e.g. [67, 69, 70]. This assumption eliminates the need of a transition model and thereby simplifying the problem. In this comparison study, N-XROTOR uses a turbulent boundary layer over the majority of the airfoil surface to calculate the airfoil properties. However, care should be taken when a fully turbulent simulation is compared with the experimental results. Some notes on the behaviour of the selected turbulence model near the leading edge is provided at the end of this section.

A turbulence model should be selected which is reasonably accurate in wall bounded flows with an ad-

verse pressure gradient and also is reasonably accurate in free-shear flows to capture the flow in the propeller slipstream. Different turbulence models exist for RANS simulations to describe the Reynolds stresses. An approach to describe the Reynolds stresses is to use a turbulent-viscosity model using an algebraic relation, a single model transport equation or by describing turbulence quantities such as  $\kappa$  and  $\epsilon$  (two-equation models). In Reynolds-stress models, modelled transport equations are solved for the Reynolds stresses and there is no need for a turbulent viscosity [59] and the consequence is a significant increase in computation time with respect to eddy viscosity models. Each of these models provide a fuller description of the turbulence. Algebraic and one-equation models (such as Spalart - Allmaras) omit the last term in equation 4.1. Two-equation turbulence models solve both the turbulent length and time scales with two different equations. One of these models is the standard  $\kappa - \epsilon$  model which has been widely used for practical flow calculations and has reasonable accuracy for a wide range of flows [59, 66, 71]. However, according to Wilcox [66] the  $\kappa - \epsilon$  model has shown to be inaccurate when adverse pressure gradients are present and has a tendency to predict the onset of separation too late. In addition, at the edge of the boundary layer, the transition from turbulent flow and non-turbulent flow is very abrupt. A number of models developed to solve these problems, such as the  $\kappa - \omega$  models, have shown a significantly more accurate prediction of separation and the boundary layer in adverse pressure gradients in a number of test cases [59, 66, 72]. The  $\kappa - \omega$  Shear-Stress-Transport (SST) model was designed to give a highly accurate predictions of the onset and the amount of flow separation under adverse pressure gradients by the inclusion of transport effects into the formulation of the eddy-viscosity. The performance of this model has been demonstrated in a number of (general) validation studies [66, 73]. The SST model uses a blending of the standard model  $\kappa - \omega$  in the inner region of the boundary layer with the  $\kappa - \epsilon$  model in the outer part of the boundary layer. These features make the SST model more accurate and reliable for a wider class of flows than the standard  $\kappa - \omega$  model.

A frequently used turbulence model for propeller simulations is the one-equation Spalart-Allmaras turbulence model [67, 70, 74, 75]. Also examples have been found in which the  $\kappa - \omega$  SST turbulence model is used for propeller simulations including:

- Ruiz-Calavera and Perdonés-Díaz [68] for transient simulations on a propeller-wing configuration.
- Ortun et al. [69] for a transient simulation of the APIAN propeller at both  $M = 0.2$  and  $M = 0.7$ .
- In Meheut [76] and Falissard et al. [77] for counter rotating open rotor configurations.

As this model has shown better performance than the Spalart Allmaras, the  $\kappa - \omega$  SST is chosen with the default values from Fluent for the modelling constants. In Rumsey and Spalart [78] it is recognised that a 'fully turbulent' turbulence model does not necessarily yield a fully turbulent solution through the complete boundary layer. Often there is a region close to the leading edge in which the eddy viscosity produced is low as the local Reynolds number is low and there is effectively a small region of flow which does not behave like a turbulent boundary layer. The N250 propeller has a  $Re_c(r)$  varying between  $1 \cdot 10^5$  to  $4 \cdot 10^5$  at the reference advance ratio which is considered to be relatively low. Fluent has implemented an option to model the effects of a low Reynolds number in the  $\kappa - \omega$  SST model via a 'low-Reynolds number correction'. With this correction the turbulent viscosity is damped depending on the local Reynolds number and thereby suppressing the development of turbulent kinetic energy in the boundary layer. The effect of this option is discussed in section 4.3.

It can be expected that the local flow velocity near the propeller surface varies significantly in chordwise direction and varies in radial direction. It is well known that the turbulent boundary layer can be subdivided into an inner and a outer layer [59]. The inner layer (characterised  $\frac{y}{\delta_{99}} < 0.1$ ) is characterised by the so-called law of the wall [59]. The inner layer has three regions; the viscous sub-layer ( $y^+ \leq 5$ ), the log-law layer  $30 \leq y^+ \leq 350$  and a buffer region in between [59]. Therefore an appropriate near-wall treatment should be applied to ensure that the approximations of the particular turbulence model hold over the complete propeller surface. A near wall treatment is required as the first layer height is constant over the surface but the  $y^+$  changes significantly along the surface for a given first element height. In order for the model to use the approximations in the sub layer of the boundary layer, automatic scalable wall functions are used to artificially shift the local small values of  $y^+$  to a fixed value. This removes the requirement of local first layer heights and simplifies the meshing procedure. The  $\omega$  based models do not require a certain  $y^+$  value in Fluent as Fluent blends the viscous sub-layer formulation and the logarithmic layer formulation [71], however the lowest values should be below this threshold.

### 4.2.3. DISCRETISATION SCHEMES

Fluent uses a pressure-velocity coupling to solve the discretised Navier-Stokes equations. Fluent provides several algorithms for the iterative calculation of the pressure and velocity including the SIMPLE, SIMPLEC, PISO, Fractional Step Method (FSM) and Coupled methods. The steady state solution is obtained by using an initial condition and iteratively finding the solution using under relaxation factors to limit the maximum growth of the solution per iteration. The SIMPLE scheme is the default algorithm in Fluent. It is recommended by ANSYS [71] to use the PISO method for transient calculations. For steady-state calculations, the PISO algorithm does not provide a noticeable advantage over SIMPLE or SIMPLEC [71]. In Jang et al. [79] a comparison was made between these algorithms for a number of reference flows. The difference in these algorithms is the convergence time required for equal convergence levels. No significant differences between the methods have been found between the (revised) SIMPLE method and SIMPLEC. PISO shows in some cases a lower required computational resources but is less robust than SIMPLE and SIMPLEC. Therefore SIMPLE is chosen as the algorithm throughout the simulations. Most of the under relaxation factors are set to their default values in Fluent as they result in a good and stable convergence for a wide range of flows [71]. Only the under relaxation factor on the energy equation is slightly decreased as the default value of 1 results in an oscillation and divergence on the residual of the energy equation and its value is reduced to 0.9 to avoid this behaviour.

For the spatial discretisation, several methods exist including first order upwind, second order upwind and third order upwind (QUICK). Higher order simulations lead to a better representation of the propeller slipstream as artificial dissipation becomes smaller with increasing order. First order upwind schemes result in significant artificial dissipation and is therefore not used. The second order spatial discretisation is a frequently used method for propeller simulations, e.g. by [49, 68, 69, 77]. For the transient sliding mesh simulation a second order discretisation on the time is used which is the same approach as in [49, 69]. In order to begin the transient simulation with a reasonably good solution, the results from the MRF method are used as the initial condition of the sliding mesh simulation. This has been suggested by e.g. [71]. The sliding mesh simulation has a time step of  $1^\circ$  of propeller rotation, based on time steps found in [67, 69, 74, 75] ranging from  $1 - 4^\circ$ . The maximum number of iterations per time step is set to 20.

### 4.2.4. DOMAIN AND BOUNDARY CONDITIONS

An overview of the domain is provided in figure 4.2. The N250 propeller is simulated on a cylinder with constant radius throughout the domain. This setup differs from the experimental setup in which a spinner with finite dimensions is used. However, the N-XROTOR results are produced with a similar setup as this CFD setup. This cylinder/hub is modelled as a slip wall, i.e. there is no boundary layer formed on this surface which influences the flow field close to the propeller.

The dimensions of the domain are assumed to be large enough to have no influence on the flow field induced by the propeller. Indications of the domain size are found in e.g. Ortun et al. [69] in which a multiblock domain is used with boundaries located approximately  $4R$  in the upstream, downstream and radial direction of the propeller. Similar dimensions are used in Ruiz-Calavera and Perdonés-Díaz [68]. The rotationally periodic nature of the problem allows for a reduced domain of one propeller blade ( $60^\circ$ ) compared with a full  $360^\circ$  domain [49, 74, 80–83] using periodic boundary conditions.

Far from the spinner and hub in radial direction the flow is parallel to the freestream flow. Therefore a symmetry boundary condition is used on this surface. Because the propeller geometry encounters moderate Mach numbers, a compressible flow simulation is performed. For compressible flows the density variations are accounted for in the mass conservation equation using the energy equation and therefore uses more computational resources than an incompressible flow. An ideal gas is assumed throughout all simulations in this thesis. The inlet and outlet boundary conditions for the compressible flow simulation consists of an inlet total pressure, inlet total temperature and an outlet total temperature and (averaged) static pressure as suggested in [71]. Their values are determined using the isentropic relations with a gage total pressure of  $p_{t,0} = \frac{1}{2}\rho V_\infty^2$  which leads to a total temperature  $T_t$  and temperature  $T$  with the reference (static) pressure being  $p_{s,0} = 1.01325 \cdot 10^5 [Pa]$ . These values lead to an inlet velocity of  $V_\infty$  and are listed in table 4.1.

The mesh consists of a rotating domain in which the propeller and spinner are located and a stationary domain in which the hub located. Different methods exist in ANSYS Fluent to model the rotating domain including a steady method (Multiple Reference Frame method (MRF)) and a transient methods (e.g. sliding mesh). The MRF model is a steady-state approximation in which individual cell zones can be assigned different rotational speeds. The flow in each moving cell zone is solved using the moving reference frame equations including Coriolis- and centrifugal forces. At the interfaces between cell zones, a local reference frame trans-

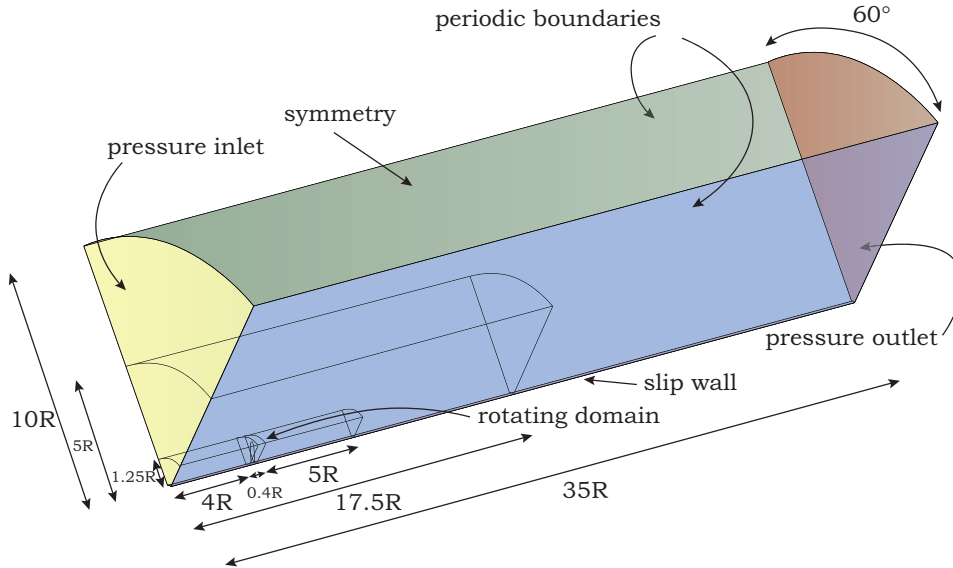


Figure 4.2: Domain setup of the N250 CFD propeller simulation with dimensions and boundary conditions indicated.

Table 4.1: Boundary Conditions for the N250 isolated propeller simulation at  $J = 0.79$

Face	Type of Boundary Condition	Value
Inlet Face	Pressure inlet w.r.t $p_a$	$p_{t,0} = 1773.64 [Pa]$ $T_t = 291.288 [K]$ $T = 289.847 [K]$ $Tu = 0.1\%$ $\frac{v_t}{v} = 2 [-]$
Outlet Face	Pressure w.r.t. $p_a$	0 [Pa]
Side faces (2x)	Periodic Boundary Condition	-
Top face	Symmetry Boundary Condition	-
Propeller	No Slip Wall	-
Spinner and hub	Slip Wall	-

formation is performed to enable flow variables in one zone to be used to calculate fluxes at the boundary of the adjacent zone. This means that the mesh itself does not rotate and this method can be referred to as a 'frozen rotor' approach. In the sliding mesh approach the mesh is physically rotating with each time step with respect to the stationary domain. At the non-conformal interfaces the flow quantities from the one domain are interpolated at the interface and transferred to the other domain. As the MRF method is a steady method, it uses significantly less computational resources compared with the transient sliding mesh method. It is recommended by Shankaran and Dogruoz [84] that the rotating domain is slightly larger than the rotating components. This is applied for the N250 domain as shown in figure 4.2. In Veldhuis and Luursma [83] it was shown that both time dependent and steady methods have relatively good agreement. The predicted axial induced velocity distribution by the sliding mesh method was slightly lower than the quasi-static method. To quantify the effect of using a simplified model for the N250 simulation, both the MRF method and the sliding mesh method are used to compute the results.

In Spalart and Rumsey [85] the importance of the correct choice of the turbulent kinetic energy and the turbulent eddy viscosity ratio  $\frac{v_t}{v}$  for inlet boundary conditions is discussed for the  $\kappa - \omega$  SST model. Excessive eddy viscosity ratios can lead to the production of turbulence in regions where no turbulence should exist. The inlet conditions effect the location of transition (e.g. [56]) and hence fully turbulent simulation have a lower sensitivity to inlet turbulent quantities. When the upstream mesh has a significant element size, the decay is not resolved accurately and hence the turbulence quantities the geometry experiences may be very different from the specified inlet conditions. In Spalart and Rumsey [85] it is shown that higher values of turbulence intensity  $Tu$  the more rapid the decay from the inlet towards the geometry and the lower the value of  $v_t$  the more rapid the decay. It is recommended to use either very low levels of  $Tu$  or very high

levels of  $\nu_t$  to achieve reasonable decay rates. For large decay rates, a coarse mesh makes the solver unable to compute the decay rate accurately and the decay may be underestimated. Recommended values for the  $\kappa - \omega$  SST model are  $Tu = 0.1\%$  and  $\frac{\nu_t}{\nu} = 2 \cdot 10^{-7} Re_L$  in which  $Re_L$  is the Reynolds number based on the length of the geometry of interest. The  $Re_c$  of the propeller is changing along the radius; for the N250 propeller at the selected operating condition ranging from  $Re_c = 1.0 \dots 4.0 \cdot 10^7$ . Therefore an intermediate value of  $\frac{\nu_t}{\nu} = 2$  is chosen. The value of turbulence intensity at the inlet plane is set to  $Tu = 0.1\%$ .

#### 4.2.5. MESH AND MESH REFINEMENT STUDY

Previous propeller simulations show quite a range in the number of cells per blade domain, in the order of  $10^5$  to  $10^6$  cells per blade domain [67, 70, 82], depending on the objective of the research. In this research a reasonable description of the propeller slipstream and a relatively good prediction of performance is required for comparison purposes.

Figure 4.2 shows the multiblock domain. The hybrid mesh consists of a unstructured grid throughout the domain with an inflation layer consisting of prismatic shaped elements normal to the propeller surface and hexahedral shaped in the parallel direction. Refinement is applied towards the propeller such that the upstream, rotating, downstream domain blocks and a refinement box around these each have a refined mesh. The mesh close to the propeller blade requires special attention. When the region of the propeller boundary layer is not sufficiently resolved, both the thrust and power may show quite large deviations. On the suction side the larger displacement thickness of the boundary layer results in a decambering effect [86] which could lead to an under prediction of the thrust and power. Not all combinations of number of elements, first element thickness and growth rate result in a smooth inflation. The settings for the inflation layer are listed in table 4.2 and have the same order as found in e.g. [68, 71]. No inflation layer is used on the spinner and hub. Although the slip condition on the spinner and hub results in much lower gradients of the flow quantities compared with a slip wall, a refinement is specified as the flow in the root region of the propeller should still be modelled with sufficient accuracy.

As discussed in the previous section, the upstream domain should be sufficiently refined to obtain the flow turbulence quantities set as boundary condition on the inlet at the propeller location without a significant numerical dissipation. It can be expected that a more refined slipstream leads to a longer existence of the trailing vorticity from the blades, as the numerical dissipation is proportional to the element size. As the induced velocity field near the propeller is to a large extent the result of the trailing vorticity, also the propeller performance is affected by numerical dissipation.

A grid refinement study is performed to analyse the effect of a finer mesh on the propeller performance quantities, blade section pressure distribution and induced velocities. The number of inflation layers and first layer thickness is iteratively determined. This means that the inflation layer in normal direction is constructed first and then the size of the other elements is determined based on the grid refinement results. Because there is no geometry other than the hub downstream of the propeller, the development of the vortex structure is of secondary importance relative to the performance quantities. Four different meshes are considered with each having a more refined mesh. A summary of the meshes is given in table 4.3 and a full description is listed in Appendix B. The table shows that there is not significant change in the performance quantities with increasing number of cells.

In Appendix B the induced velocities in a plane behind the propeller are shown. The induced velocities in the tip region show quite a deviation w.r.t. the finest mesh. In this region the velocity gradients are largest due to the tip vortex and is better captured with a finer mesh. The difference between mesh 2 and mesh 3 is mainly the refinement of the volume surrounding the rotating and slipstream domains. This shows a relatively large effect of the mesh away from the propeller on the induced velocities in the tip region. The over prediction of the  $C_p$  of mesh 2 is also observable in the higher tangential induced velocity. The  $C_p$  distribution of the blade section at  $r/R = 0.70$  is shown in Appendix B. The meshes show only minor deviations on the  $C_p$  distribution and no conclusion can be made based on those distributions. The effect of a more refined propeller surface (between mesh 3 and 4) is a slightly lower thrust and torque. However, an increase of the number of cells of almost 18% results only in a 0.4% deviation in both  $C_T$  and  $C_p$ . Based on these results, mesh 3 is selected which is considered a balance between accuracy and computational time.

### 4.3. COMPARISON OF CFD RESULTS WITH N-XROTOR

In this section the CFD results of the N250 propeller are compared with experimental data and the results computed by N-XROTOR.

Table 4.2: Inflation layer settings for the N250 propeller simulation.

Mesh	Value
Number of inflation layers	12
Growth rate	1.05
First layer thickness	$8 \cdot 10^{-5} [m]$
$y^+$ (for $J = 0.79$ )	1 – 40

Table 4.3: Summary of grid refinement study on the CFD simulation of the N250 propeller using the Multiple Reference Frame approach at  $J = 0.79$ . The different meshes may be found in Appendix B.

Mesh	Number of elements	$C_T [-]$	$C_P [-]$
Mesh 1	6,473,833	0.2190	0.2469
Mesh 2	8,704,778	0.2214	0.2483
Mesh 3	9,129,987	0.2205	0.2480
Mesh 4	10,753,963	0.2195	0.2470

### 4.3.1. RADIAL DISTRIBUTIONS AND PERFORMANCE

The performance quantities computed with CFD and with N-XROTOR at an advance ratio of 0.79 are compared in table 4.4. Compared with the Multiple Reference Frame (MRF) simulation with the standard  $\kappa - \omega$  SST model, N-XROTOR shows an overprediction of the thrust by 5.25% and an overprediction of the power by 3.67%. The thrust and torque distributions computed with CFD and N-XROTOR at  $J = 0.79$  are compared in figures 4.3 (a) and (b). Overall the distributions predicted by N-XROTOR correspond quite well with the CFD data with the general trend well captured and the location of the maximum is captured approximately at the same location. The main observation is an over prediction of the thrust (and therefore also torque) at the highest loaded region on the propeller. The lower thrust and torque of the CFD simulation is also observed in the performance curves in figures 4.3 (c) and (d) as a constant offset in  $C_T$  with respect to N-XROTOR and an approximately constant offset with respect to experimental data. The following sections discuss this over prediction.

Next to the over prediction in the high loading region, a difference may be noticed in the hub region. The hub effect increases the circulation on the propeller blade and this effect is clearly visible in the CFD results as a slight increase in thrust and torque. The finite circulation leads to a hub vortex, which is shown in the axial vorticity behind the propeller in figure 4.7 in a concentrated vorticity near the propeller root. The N-XROTOR results have a finite loading at the hub radius, but the value is under predicted. However, the deviation will not have a significant effect on the performance quantities when the blade loading in this region is relatively small.

The induced velocities computed in N-XROTOR do not include the effect of viscosity on the development of the slipstream as the vortex structure in the CFD dissipates downstream. Additionally, the propagation of the low velocity wakes coming from the trailing edges of the propeller blades is not modelled in N-XROTOR. This latter effect has been recognised by Roosenboom et al. [67] in the comparison of an inviscid blade and a viscous blade CFD simulation. Therefore it can be expected that the induced velocities in the slipstream computed by N-XROTOR are slightly higher than the CFD result.

Table 4.4: Comparison of performance quantities as calculated by N-XROTOR, a steady CFD simulation (Multiple Reference Frame method) and a transient CFD simulation (sliding mesh) for the N250 propeller at  $J = 0.79$ .

Method	Turbulence model	$C_T [-]$	Deviation	$C_P [-]$	Deviation	$\frac{C_T}{C_P} J [-]$	Deviation
CFD - Sliding mesh	$\kappa - \omega$ SST	0.2228	-	0.2505	-	0.7064	-
CFD - MRF	$\kappa - \omega$ SST	0.2209	-0.85%	0.2480	-1.00%	0.7074	+0.10%
CFD - MRF	$\kappa - \omega$ SST with low $Re$ corr.	0.2220	-0.36%	0.2495	-0.39%	0.7066	+0.04%
N-XROTOR	-	0.2345	+5.25%	0.2597	+3.67%	0.7133	+0.98%

### 4.3.2. EFFECT OF AIRFOIL PROPERTIES

The overprediction of the thrust and torque may be a result of an over prediction of the airfoil properties in N-XROTOR which are computed with XFOIL. In figure 4.3 (c) and (d) the thrust and respectively the power coefficient are compared for different values of  $N_{crit}$  used in N-XROTOR to compute the airfoil data. The figure shows a quite significant effect of the transition prediction on the thrust and power and shows the range in which the result is influenced by 2D transition. In this case, a relatively high value of  $N_{crit} = 5$  corresponds best with the experimental data. This could indicate that a relatively large part of the propeller in the experiment had laminar flow. When the  $N_{crit}$  is reduced the transition points on both lower and upper surface move towards the leading edge causing a decambering effect on the boundary layer. This results in a reduced camber and a lower thrust. This can be readily observed in figure 4.3 (e) in a reduction in thrust over the complete blade computed by N-XROTOR. Appendix B shows the corresponding distributions of  $C_l(r)$  which is lower over the complete blade. The performance curves figure show almost a constant off-set over the complete range of  $J$ . The overall observation is that the N-XROTOR results compare better with the fully turbulent CFD with a forward movement of the transition point (in the next section more detailed discussion of the turbulence model in the CFD is given). The effect on the  $C_p$  with a larger region of turbulent flow is an increased profile drag which increases the torque. However, the reduced lift component causes a decrease in the total torque. Figure 4.3 (b) shows a net reduction in power when a larger portion of the blade has turbulent flow. Similar trends are found in e.g. Taranov and Lobachev [87] who shows several percent higher  $C_T$  and  $C_p$  predictions when a transition model is used in combination with the  $\kappa - \omega$  SST model and shows better agreement with experimental results.

A comparison of 2D CFD simulations on one of the airfoil sections of the non-uniform inflow propeller shows a relatively large deviation of airfoil properties between XFOIL and CFD. When the optimised propeller is calculated with CFD data instead of XFOIL data, a reduced thrust and torque has decreased several percent (further discussed in Chapter 7).

One of the reasons that the airfoil properties between XFOIL and the CFD simulation can vary is by the turbulence model. In XFOIL the transition occurs not exactly at the leading edge. In Rumsey and Spalart [78] it is discussed that the standard  $\kappa - \omega$  SST model does not correctly model the boundary layer near the leading edge for low  $Re_c$  flows. In table 4.4 it is shown that compared with the standard SST model, the SST model with low Reynolds number correction leads to slightly higher thrust and torque values. A comparison of the distributions of  $dT(r)$  and  $dQ(r)$  of these models is given in Appendix B and shows minor differences. The higher values show that in this case the modeling of the boundary layer near the leading edge has a definite but relatively small effect on the results. A further discussion on the cause of these deviations is given in Chapter 7.

### 4.3.3. RADIAL FLOW

One of the effects that is not captured in N-XROTOR is radial flow. To visualise the flow direction close to the propeller surface, wall shear streamlines on the surface can be used. Figure 4.4 shows the wall shear streamlines on the suction and pressure side of the N250 propeller. Figure 4.5 shows the velocity streamlines at a number of distances away from the propeller surface. A similar pattern of the velocity streamlines can be noticed compared with the wall shear streamlines and the radial flow relative to the chordwise flow is relatively high close to the surface. In figure 4.5 a quite large region outside the boundary layer on the low pressure side is shown to have a radial flow component. It can be noticed that at the trailing edge a radial flow component is present towards the propeller tip up and till approximately  $0.7R$ . In the tip region, a radial flow in opposite direction is present. Also, the radial flow is noticeable away from the surface but is pronounced within the boundary layer. There are a number of individual causes for radial flow which add together to the total radial velocity for the N250 simulation:

- The vorticity that is shed from the trailing edge has a tendency to create a radial flow on the suction and a radial flow in opposite direction on the pressure side. This behaviour can be clearly distinguished in figure 4.4 with the location of the maximum circulation indicated. From the hub to  $\Gamma_{B,max}$  the vorticity causes a flow towards the tip on the suction side. At  $\Gamma_{B,max}$  the shed vorticity  $\frac{d\Gamma}{dr} = 0$  and from that location to the tip the vorticity changes direction causing a radial flow towards the root on the suction side, as sketched in figure 4.4. The region of influence of this propeller is in the trailing region and does not significantly influence the upstream flow.
- The volume of air inside the boundary layer experiences a centrifugal acceleration which is proportional to the radial location and results in a radial flow component. Thereby the streamlines are bended

towards the tip. This effect is pronounced on boundary layers close to separation as the radial velocity component is relatively large and is therefore especially present on the suction side of the propeller [57]. This effect may be observed in figure 4.4. The radial acceleration is increasing towards the tip and consequently also the radial velocity is increasing. This results in a Coriolis force which becomes therefore larger towards the tip and bends the wall shear streamlines more in line with the chord direction.

- The contraction of the slipstream also causes a radial flow component, especially at high disk loadings [58]. This contribution will be noticeable in the tip region as a radial flow towards the root on both suction and pressure sides.

The effect of radial flow is expected to influence the magnitude of the local axial velocity and change the aerodynamic coefficients of the blade sections (noted in Zondervan [58]). The aerodynamic coefficients are slightly changed because the radial flow increases the boundary layer thickness on the airfoil and reduces the magnitude of the effective velocity in chordwise direction. In N-XROTOR the presence of radial flow is completely neglected in the computation of the induced velocities.

#### 4.3.4. COMPARISON OF MULTIPLE REFERENCE FRAME AND SLIDING MESH

The effect of the sliding mesh method compared with the Multiple Reference Frame (MRF) method is shown in table 4.4 as a slight increase in thrust and power. To determine what mechanism causes this change in thrust and power, one can observe the vorticity distribution in the propeller slipstream in figure 4.6. In the MRF approach the vorticity shed from the trailing edge moves downstream with the freestream flow plus the axial and tangential induced velocities and maintains relatively concentrated. The development of the slipstream in the sliding mesh shows a helical structure of the vortex sheets which includes  $\Omega$  due to the frame motion, in addition to the freestream and induced velocity field.

It can be expected that the vorticity distribution in the slipstream affects on the flow field in the vicinity of the propeller and thereby influencing the propeller performance. The sliding mesh results in a more averaged distribution of vorticity from the perspective of the propeller. The MRF approach may induce velocities in a more concentrated way. This effect is shown in figure 4.7 which shows the axial velocity in a plane behind the propeller. The sliding mesh approach has a much more constant distribution of  $V_a$  in circumferential direction than the MRF approach. In the latter the high induced velocities move in axial direction without significant mixing. The sliding mesh therefore shows a more constant contraction of the slipstream. When the distribution of  $\gamma_a$  is compared one can clearly observe a shift in circumferential direction of the vorticity. In addition, the deformation of the vorticity in the root region is not observed in the MRF simulation.

The upstream pressure shows quite a large deviation between the two methods. Where the axial velocity and vorticity behind the propeller are more concentrated in the MRF simulation, the opposite is the case for the upstream pressure. The magnitude of the lowest pressure in the sliding mesh simulation is lower around in the tip region. The lowest pressure is lower than in the MRF simulation, partially due to the slightly higher thrust. However, it may be expected that the time dependency has a larger effect. The pressure in an instance in time has larger variations in circumferential direction compared with the more averaged pressure in the MRF simulation. The upstream effect of the propeller on the non-uniform inflow simulation can be expected to be larger and more accurately when simulated with the sliding mesh approach.

An interesting observation is that at the periodic boundary conditions the vorticity of one boundary does not match the other boundary, especially visible in the MRF simulation. This means that these boundary conditions affect the solution, although the effect may be small. As the mesh at the boundaries is conformal, no spatial interpolation errors should be present. Other possible causes are not identified by the author. It should be mentioned that the sliding mesh simulation yields to significant improvement in the convergence of the residuals compared with the MRF approach. Especially the convergence of the residuals from the continuity equation is improved (from  $10^{-3}$  to  $10^{-5}$ ).

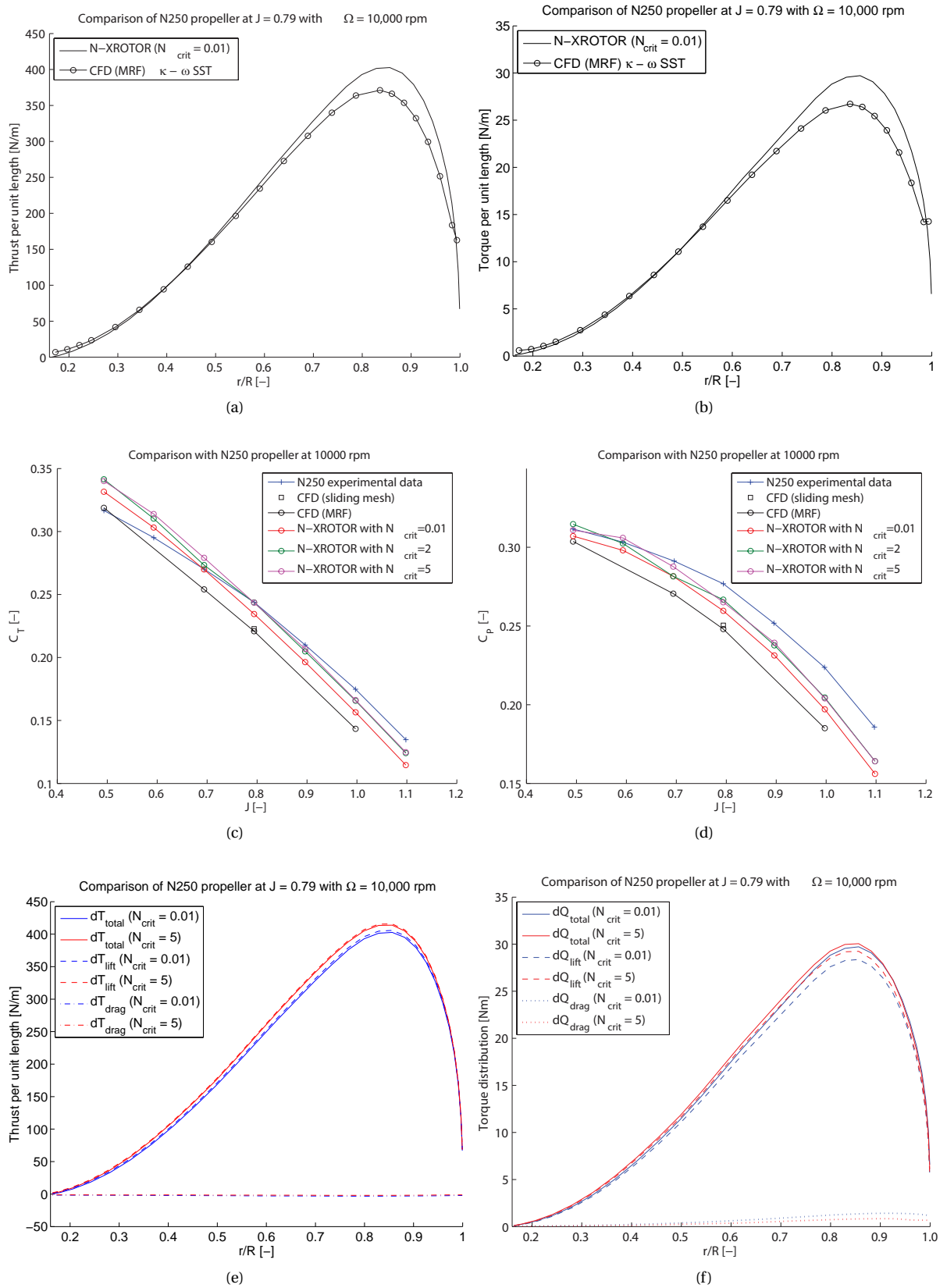


Figure 4.3: In (a) and (b) the comparison of N-XROTOR with CFD at  $J = 0.79$ . In (c) and (d) a comparison of results from N-XROTOR, experimental data and CFD. In (e) and (f) the effect of  $N_{crit}$  on the thrust and torque distributions

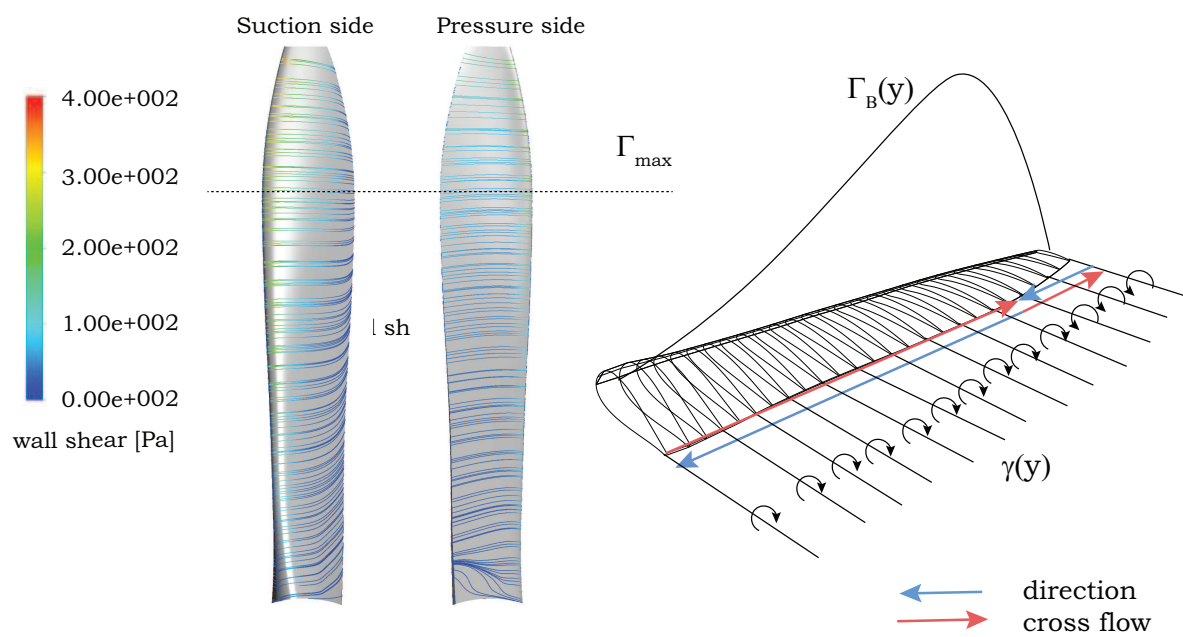


Figure 4.4: Left: radial flow visualised using wall shear streamlines on the propeller surface and the location of maximum circulation is indicated. In the right figure the effect of trailing vorticity on the induced radial flow component.

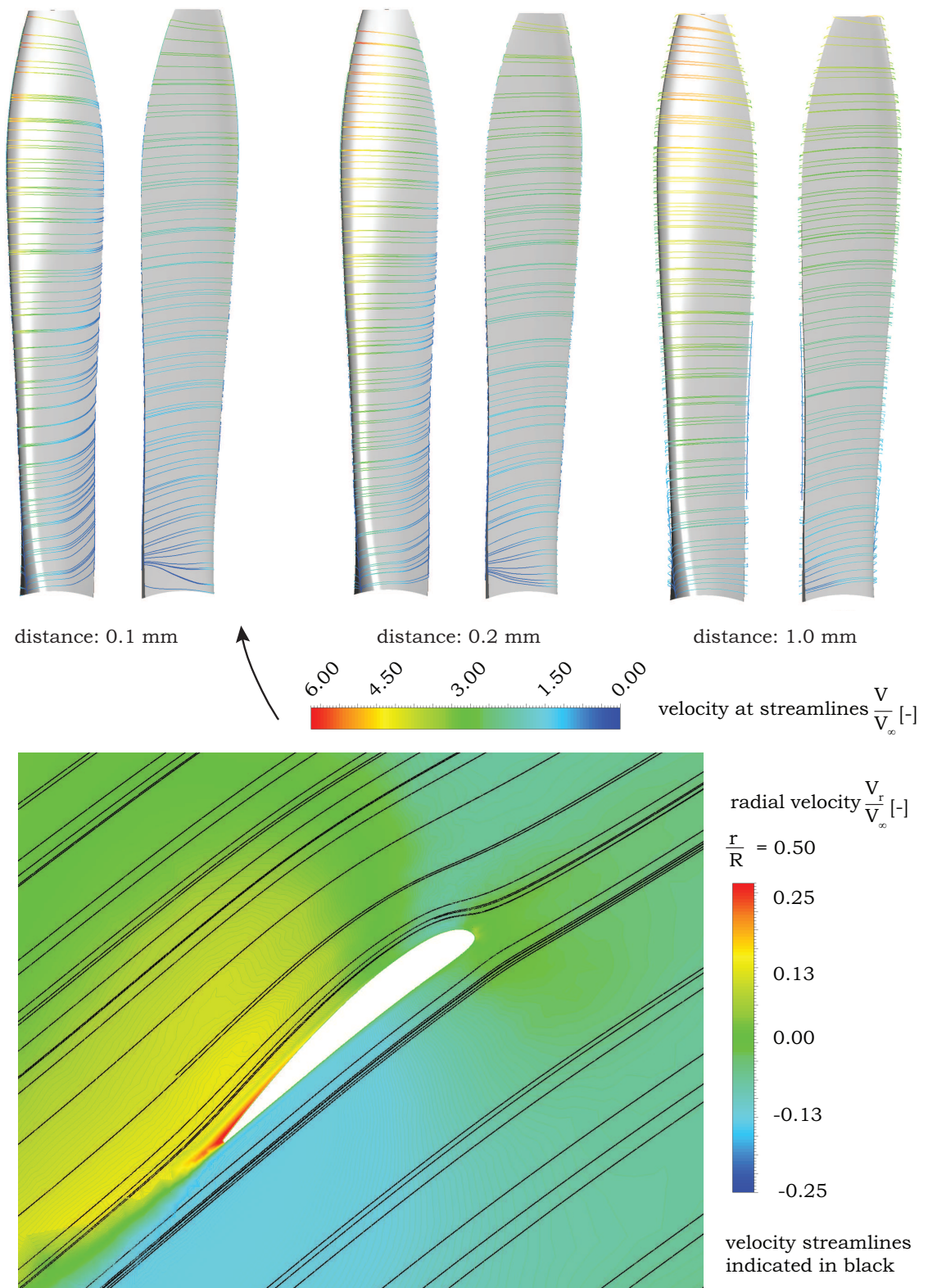


Figure 4.5: Top: velocity streamlines at a number of distances normal to the N250 propeller to visualise the radial flow over the propeller blade. Bottom: the radial flow at a plane at  $\frac{r}{R} = 0.50$  with the velocity streamlines indicated.

## Multiple Reference Frame

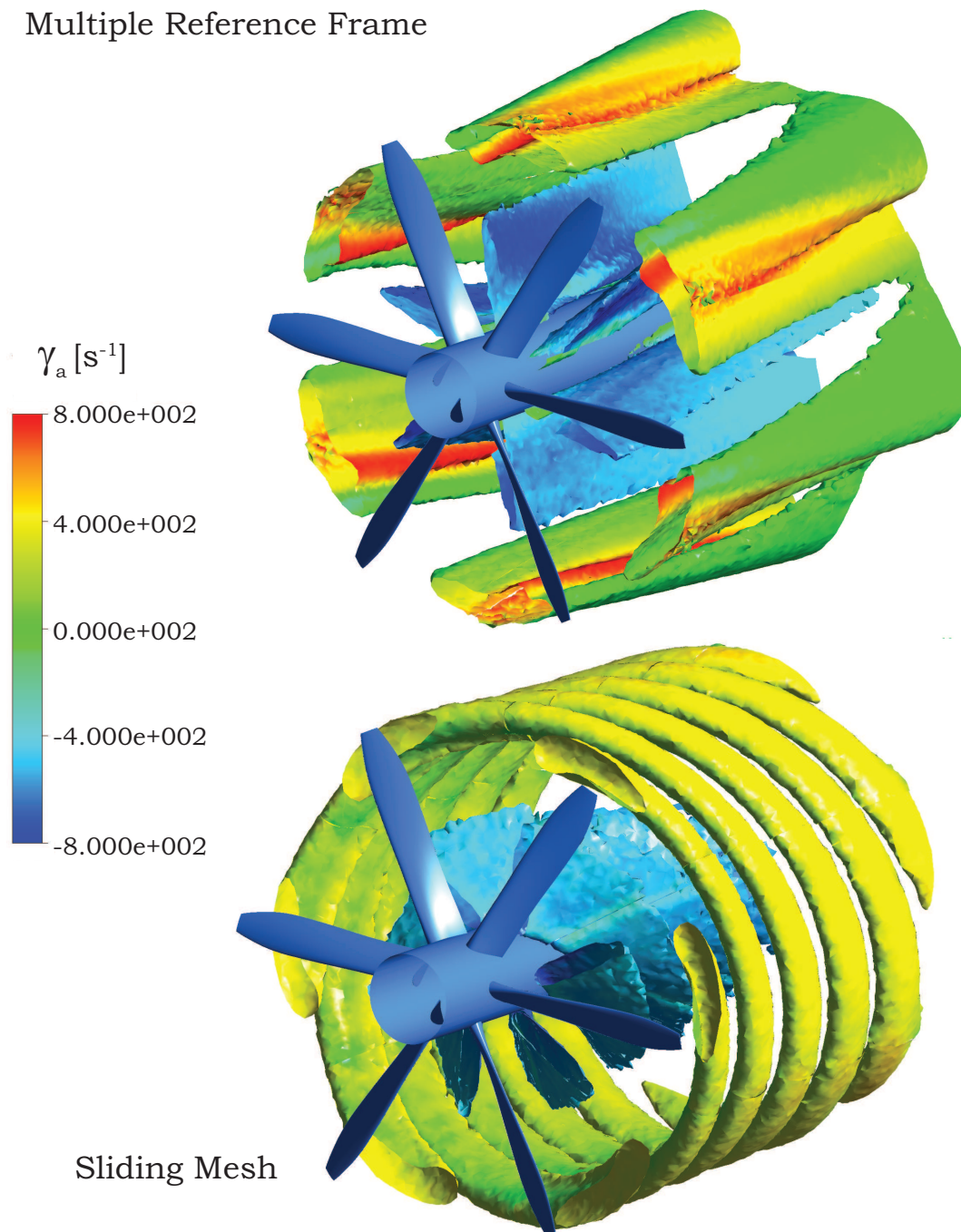


Figure 4.6: Isosurface of vorticity at  $\gamma = 800[s^{-1}]$  with the colors indicating the axial component of vorticity for both the Multiple Reference Frame simulation and the sliding mesh simulation of the N250 propeller at  $J = 0.79$  (the results are cut off at a distance behind the propeller for visualisation purposes).

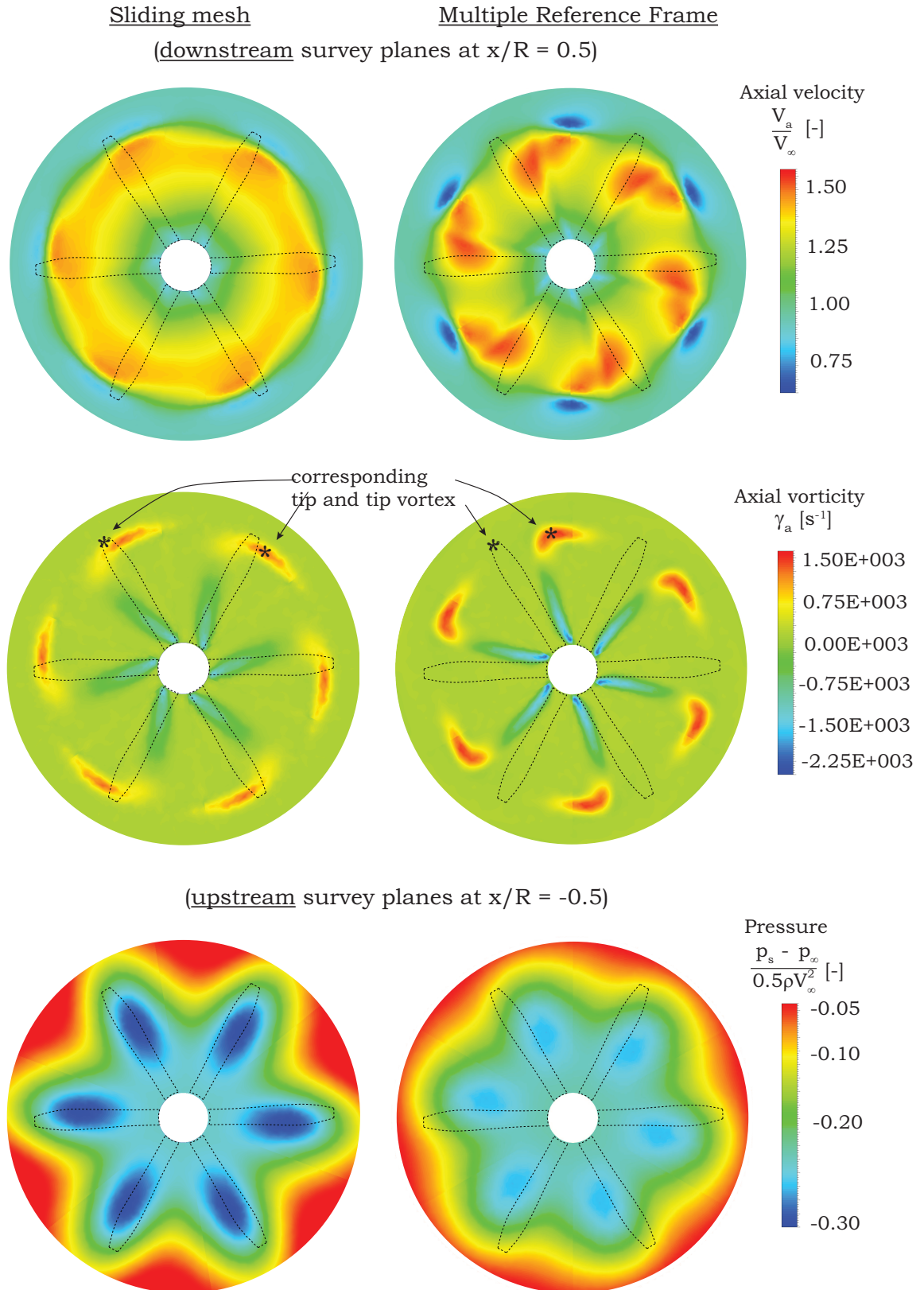


Figure 4.7: Comparison of axial velocity and axial vorticity in a plane behind the N250 propeller at  $\frac{x}{R} = 0.50$  for both the Multiple Reference Frame simulation and the sliding mesh simulation of the N250 propeller at  $J = 0.79$ .



# 5

## CFD SIMULATION OF A REFERENCE NON-UNIFORM INFLOW

For the analysis and design of a propeller in a non-uniform inflow, a thrust requirement and the inflow of the propeller should be known a priori as it is assumed that the inflow and drag do not change during the optimisation process (section 3.3). These quantities are obtained by modelling the viscous flow around a reference geometry and extracting the flow quantities at an aft location on this body at which the propeller is located. Two CFD simulations are discussed in this chapter, an isolate fuselage simulation and a fuselage with an Actuator Disk at the location of the propeller. The latter simulation is to estimate the interference drag of the propeller which is modelled as using an Actuator Disk. This chapter describes the reference body in section 5.1 followed by the setup of the flow domain to conduct Computational Fluid Dynamics (CFD) simulations in section 5.2. The results of these simulations are provided in section 5.3. An approximation of the effect of an installed propeller on the fuselage drag and inflow is discussed in section 5.4.

### 5.1. GEOMETRY OF REFERENCE FUSELAGE AND OPERATING CONDITION

The non-uniform profile of a boundary layer can be obtained by modelling a viscous flow over any curved or uncurved shape. The goal is to design and analyse the non-uniform inflow propeller for a relatively realistic flow condition to include a number of effects which are not present when a flow over a flat plate is simulated, including three-dimensional flow and interaction effects. The consequence of applying the design to one fuselage is that the fuselage shape influences the results and hence conclusions regarding the a propeller in the non-uniform flow need to be formulated carefully. However the advantage of using a realistic fuselage is that a more complete understanding of the non-uniform inflow condition can be achieved. The selection of the reference body is based on a number of requirements:

- The body should be an axisymmetric body of revolution to ensure no time-dependency of the propeller inflow. The effects of time-dependent inflow which originates from e.g. an upstream wing or non-axisymmetrical fuselage are considered to be a separate problem.
- The body should have a shape which resembles a fuselage shape, i.e. it has a rounded fore body, a cylindrical center body and a tapered aft body.
- In order to validate the CFD simulation of the isolated fuselage case, it is preferred that validation data or empirical data on the fuselage drag is available.

Chappell and Porter [88] documented a large number of front, center and aft body shapes of bodies of revolution including empirical profile drag predictions for combinations of these sub-bodies. Based on the above mentioned requirements, body 7 from Chappell and Porter [88] is chosen. A three-dimensional representation of the fuselage is shown in figure 5.1 (a) and the description of the shape can be found in Appendix C.

There are several considerations which might be important in the selection of the propeller location in axial direction including the pressure gradient of the boundary layer, the design of the aft fuselage (i.e. the 'boat tail angle'), hub radius and structural considerations. The axial location of the propeller on the tapered aft fuselage is not optimised for this study and is set to a fixed value. A finite hub radius is chosen because

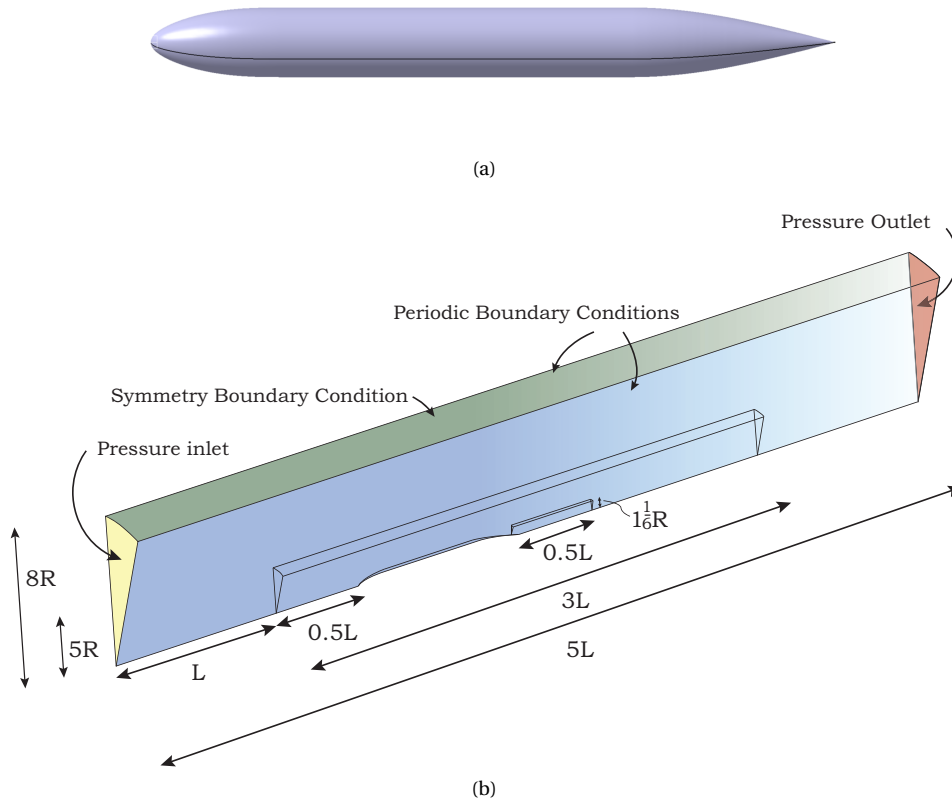


Figure 5.1: Reference fuselage based on Chappell et al. [88]. The fluid domain of the isolated fuselage is shown in (b) including the dimensions ( $L$  is the fuselage length and  $R$  is the fuselage radius). The different boundary conditions are also shown. The three domains (outer domain, refinement box and slipstream) can be distinguished as well.

it may be expected that the effectiveness of the propeller is increased when a finite hub radius is present as will be discussed in later chapters. To capture most of the fuselage boundary layer, the propeller should be positioned as far aft as possible with still an appropriate hub radius. A propeller location at  $\frac{x}{L_{fuselage}} = 0.967$  is chosen with being the fuselage length. This value gives a hub radius of approximately 20% of the radius when the propeller tip is just inside the boundary layer of this particular geometry and operating condition. This value is in line with several uniform-inflow propellers which have a hub radius in the order  $0.2R$  [64, 65, 89].

The length of the fuselage is based on the Reynolds number of (approximately)  $= 10^7$  [-] for which the drag is empirically determined by Chappell and Porter [88]. The free stream velocity of  $70$  [m/s] is chosen in combination with standard atmospheric conditions. With these conditions, a potential wind tunnel experiment to reproduce the results obtained in this report could be conducted. Table 5.1 summarises the operating conditions and fuselage length which are used in the remainder of this study.

## 5.2. CFD SIMULATION OF THE ISOLATED FUSELAGE

This section provides the setup of the CFD simulations of the isolated fuselage. Most of the settings are the same as for the N250 simulation discussed in the previous chapter. A brief discussion on the setup is given in section 5.2.1. Then the domain and boundary conditions are discussed in section 5.2.2. A mesh independence study is done in section 5.2.3 which also provides the chosen mesh.

### 5.2.1. COMPUTATIONAL SETTINGS

The choice of computational strategy is, where possible, kept the same as for the N250 propeller simulation discussed in section 4.2.1. Some additional remarks are listed in this section.

For the design and analysis a time average of quantities such as the fuselage drag and boundary layer profile are required. There is no time dependency on the flow on the body of revolution and therefore steady

Table 5.1: General flow quantities used in the simulation of the isolated fuselage

Quantity	Value
$V_\infty$	70[m/s]
$\rho$	1.225[kg/m <sup>3</sup> ]
$p$	1.01325 · 10 <sup>5</sup> [Pa]
$\mu$	1.780 · 10 <sup>-5</sup> [Pa · s]
$L_{fuselage}$	6[m]
$Re_L$	10 <sup>7</sup> [-]

simulations are performed. It is assumed that the flow over the fuselage is fully turbulent as the transition behaviour is considered not relevant for this research. The relatively low free stream Mach number of about 0.20 does not necessarily require a compressible flow simulation to achieve reasonable accurate results. However, the propeller tip Mach number is significantly higher than this free stream velocity and therefore the propeller-fuselage simulation is required to be compressible and for consistency the isolated fuselage simulation is also a compressible simulation.

For the isolated fuselage simulations equal considerations in terms of turbulence modelling as for the propeller simulation are important, such as the capability for adverse pressure gradients, the performance in the shear layer of the propeller slipstream and the general prediction of lift and drag. A number of examples of studies which use the  $\kappa - \omega$  SST model have been found for simulating a flow around an axisymmetric body. Barry and Boniface [90] uses the  $\kappa - \omega$  SST turbulence model for an actuator disk simulation (which is also performed in section 5.4) and good agreement with experiments is found in Kim and Rhee [72] in which several turbulence models are compared in simulations of an isolated ship hull. Although the Reynolds number for flow around ship hulls is different and no compressibility effects are present, their conclusions can be used as guidelines.

### 5.2.2. DOMAIN AND BOUNDARY CONDITIONS

The flow over an axisymmetric body of revolution can be simulated with either a three-dimensional (3D) domain or a two-dimensional (2D) domain with the appropriate boundary conditions. A 3D domain is chosen as it is preferred to use a similar domain as a starting point for the 3D blade simulation in Chapter 7. Similar to the N250 simulation, periodic boundary conditions are used due to the axisymmetric nature of the problem. To solve the flow over the fuselage, a wedge out of a 360° cylinder with an arbitrary angle of 20° is modelled with its axis of rotation aligned with the symmetry axis of the fuselage. Figure 5.1 (b) shows the contour of the domain. The inlet is  $1.5L_{fuselage}$  upstream of the fuselage nose and the outlet is  $2.5L_{fuselage}$  downstream of the fuselage tail. The radius of the slipstream is  $1\frac{1}{6}$  times the radius of the fuselage to capture most of the shear layer of the fuselage wake. The boundary of the domain is eight propeller radii from the fuselage center line. It is assumed that the flow at the fuselage is not influenced by the finite size of the domain.

The boundary conditions are also indicated in figure 5.1 (b). The upper face of the wedge is a symmetry boundary condition. The outlet face of the wedge has a pressure boundary condition equal to the ambient pressure as the influence of the fuselage on the pressure far down stream is assumed to be negligible. The inlet is a pressure inlet condition with a gage value equal  $p_{t,0}$  to the dynamic pressure of the free stream flow.

As discussed in section 4.2.1, inlet quantities of  $Tu$  and  $v_T/v$  are important. Recommended values for the  $\kappa - \omega$  SST model are  $Tu = 0.1\%$  and  $\frac{v_T}{v} = 2 \cdot 10^{-7} Re_L$  in which  $Re_L$  is the Reynolds number based on the length of the geometry of interest. These recommended values have been used in the fuselage simulations and correspond to the values of the N250 propeller. The boundary conditions are summarised in table 5.2.

### 5.2.3. MESH SETUP AND MESH INDEPENDENCE STUDY

To determine the effect of the mesh size in the different volumes on the flow at the location of a propeller and the drag of the fuselage, a mesh independence study is conducted. As Fluent is an element-based solver, the number of elements is an indicator of the accuracy. The definitions of the mesh types (coarse to extra fine) for each volume are given in table 5.3. The different combinations of the sub meshes which are considered are provided in table 5.4.

The domain is divided into three volumes to allow for grid refinement: an outer domain, a refinement

Table 5.2: Boundary Conditions for the isolated fuselage simulation to obtain an inflow profile for the isolated propeller simulation

Face	Type of Boundary Condition	Value
Inlet Face	Pressure inlet w.r.t $p_a$	$p_{t,0} = 3001.25[Pa]$ $T_t = 293.519[K]$ $T = 291.081[K]$ $Tu = 0.01\%$ $\frac{V_t}{V} = 2[-]$
Outlet Face	Pressure w.r.t. $p_a$	$0[Pa]$
Side faces (2x)	Periodic Boundary Condition	-
Top face	Symmetry Boundary Condition	-
Fuselage	No Slip Wall (symmetry condition)	-

box and a slipstream box. The refinement box close to the fuselage has a finer mesh than the outer domain as higher velocities and gradients are expected in that region. The slipstream box has a finer mesh than the refinement box to capture the wake of the fuselage.

First the volume mesh is generated in which the outer domain, refinement box and slipstream box are meshed as 'fine'. With this mesh the first layer thickness on the fuselage surface is iteratively determined based on the requirement of an acceptable  $y^+$  value for the  $\kappa - \omega$  SST model. A range of  $2.4 \leq y^+ \leq 30.7$  is used. The number of prism shaped elements in the inflation layer on the fuselage surface is iteratively determined by capturing most of the boundary layer in which the eddy viscosity is the quantity to visualise the boundary layer. A first layer thickness of  $3e^{-4}$  [m] and 20 inflation layer are used with a growth rate of 1.25.

Both the profile drag of the fuselage and the flow at the aft fuselage are compared for mesh 1 to mesh 5. Figure 5.2 shows at the location of the propeller the  $V_a/V_\infty$  velocity and  $p_t/p_{t,0}$  distributions. A small effect of the mesh size on the velocity and total pressure distributions can be observed but the general trend is that the distributions become smoother with increasing mesh size. The distributions from mesh 4 and mesh 5 are almost on top of each other, which means that the benefit of a finer refinement box is limited. Meshes 1 to 3 show a few irregularities which disappear with increasing mesh size. The profile drag of the isolated fuselage for each mesh is listed in table 5.4 with a drag coefficient defined as:

$$C_{d,fuselage} = \frac{D_{fuselage}}{\frac{1}{2}\rho V_\infty^2 S_{fuselage}} \quad (5.1)$$

The value of  $S_{fuselage}$  is determined using Chappell [91]. The table shows that the value converges towards a value of just over 74 [N] and is under predicted with approximately 8% compared with the value from Chappell [91] and shows a reasonable prediction by CFD. The offset with the reference value could be due to several reasons. The method is an empirical method and showed for a few comparisons with experimental data performed by Chappell [91] deviations of approximately 5%. The method is not able to capture local effects on the boundary layer shape for example and the value should be considered as an indication only. The predictions of the CFD simulation is highly dependent on the turbulence model, as shown in table 5.5. Based on the convergence of the drag and the distributions on the aft fuselage, mesh 4 is chosen.

### 5.3. SOME RESULTS

In this section some relevant results from the isolated fuselage simulation are presented. Figure 5.2 shows the total pressure distribution at the propeller plane. When the radius is set as the boundary at which the total pressure is 99% of the free stream total pressure, one gets a radius of 0.2404 meter. This value is used in the remainder of this report. It is clearly shown in figure 5.2 that the edge of the boundary layer does not correspond to the location at which the edge is close to the free stream velocity. Instead of the axial velocity, the total pressure as fraction of the free stream (gage) total pressure is a good indicator for the thickness of the boundary layer as the aft fuselage curvature does induce a velocity on the edge of the boundary layer and there is a radial flow component. In figure 5.2 (c) the normalised  $p_s$  value through the boundary layer of the viscous simulation is compared with the result of a fully inviscid simulation. Outside the boundary layer, a small off-set of the  $p_s$  can be noticed which is a direct result of the displacement thickness of the boundary layer. This off-set stays rather constant from outside the boundary layer towards  $y/R = 0.8$ . From that location on, the effect of the plane of interest not being perpendicular to the surface arises. The static pressure of a flat

Table 5.3: Definition of sub-meshes used in the grid convergence study of the isolated fuselage CFD simulation

Volume	Mesh Type	Element size [m]
Outer domain	Coarse	$5.0e-1$
	Fine	$4.0e-1$
Refinement box	Coarse	$1.0e-1$
	Fine	$8.0e-2$
	Extra Fine	$6.0e-2$
Fuselage surface	Coarse	$2.0e-2$
	Fine	$1.5e-2$
	Extra Fine	$1.0e-2$
Fan surface	Fine	$1.5e-2$
	Extra Fine	$1.0e-2$
Slipstream box	Fine	$4.0e^{-2}$
	Extra Fine	$3.5e^{-2}$

Table 5.4: Grid refinement study on the isolated fuselage CFD simulation. The different meshes can be constructed using table 5.3. The general flow settings are listed in table 5.1. For the drag computation the  $\kappa - \omega$  turbulence model with automatic wall functions are used. The drag values are for the complete fuselage. The drag coefficient prediction is compared with empirical data from Chappell [91] and the drag coefficient definition as equation 5.1

Mesh	Outer domain	Refinement box	Fuselage surface	Fan surface	Slipstream box	Number of elements	$D_p$ [N]	$C_{d,p} \cdot 10^{-3}$ [-]	$\Delta C_{d,p}$ ESDU
ESDU	-	-	-	-	-	-	-	2.7670	-
Mesh 1	Coarse	Coarse	Coarse	Fine	Fine	427,899	73.970	2.5548	-7.67 %
Mesh 2	Coarse	Coarse	Fine	Fine	Fine	533,640	73.761	2.5476	-7.93 %
Mesh 3	Fine	Fine	Fine	Extra Fine	Fine	637,369	73.818	2.5495	-7.86 %
Mesh 4	Fine	Fine	Extra Fine	Extra Fine	Extra Fine	939,320	74.107	2.5595	-7.50%
Mesh 5	Fine	Extra Fine	Extra Fine	Extra Fine	Extra Fine	1,171,989	74.022	2.5566	-7.60%

Table 5.5: Effect of turbulence model on isolated fuselage drag computed with mesh 4 (no-slip fuselage and spinner)

Turbulence Model	$D_p$ [N]	$C_{d,p} \cdot 10^{-3}$ [-]	$\Delta C_{d,p}$ ESDU
Standard $\kappa - \epsilon$	79.446	2.8613	+3.41 %
$\kappa - \omega$ SST	74.107	2.5595	-7.50%
Reynolds Stress Model	72.227	2.4946	-9.84%

plate boundary layer is approximately constant [92] but on a curved surface this is not necessarily the case. Especially if the plane of interest is not perpendicular to the surface, which in this situation is the case (figure 5.2 (c)).

Figure 5.2 (d) shows that through the boundary layer the velocity in radial direction is non-zero because of the curved aft fuselage. The maximum  $V_r$  is approximately 9% of the freestream flow. However, the radial flow component with respect to the axial component in the boundary layer is approaching  $V_r/V_a = 0.25$  towards the fuselage surface. This indicates a significant radial flow component.

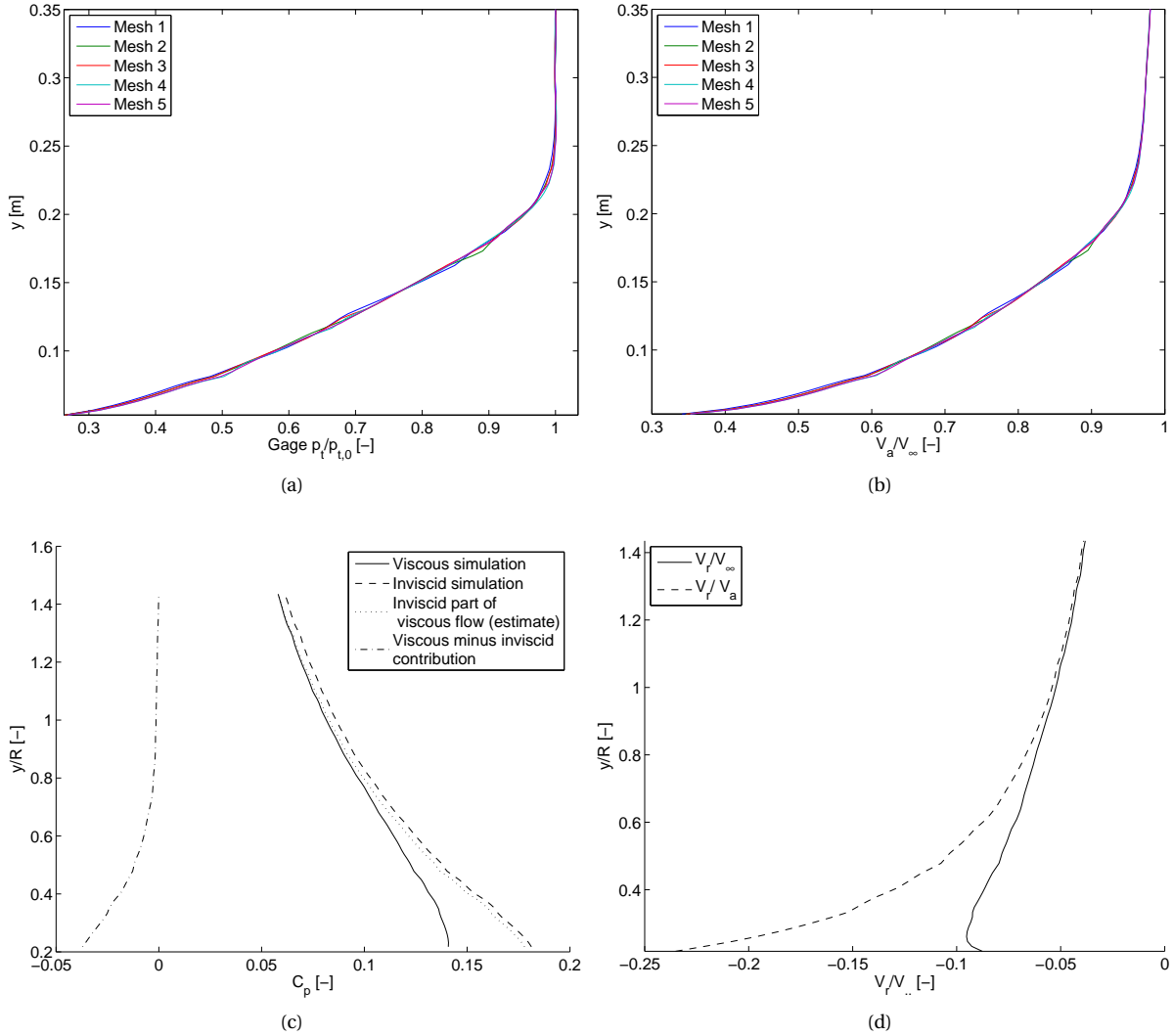


Figure 5.2: Comparison of the distributions of  $p_t$  in (a) and  $V_a$  in (b) at the propeller location for different mesh configurations. In (c) the pressure at the plane of the propeller is shown for a viscous simulation and an inviscid simulation, indicating which part of the induced pressure is a potential flow effect. In (d) the absolute and relative radial flow component at the plane of the propeller. As radius for (c) and (d),  $R = \delta_{99}$  is taken.

## 5.4. APPROXIMATION OF UPSTREAM EFFECTS PROPELLER

Both the inflow of the propeller and the thrust requirement change by the presence of the propeller as discussed in section 2.3. This section provides an approximation of these upstream effects.

The upstream effect can be quantified by a simplified Actuator Disk (AD) model of a propeller in the CFD setup discussed in the previous sections to determine the required  $T_{shaft,installed}$ . A similar approach has been used in Choi and Kinnas [93] and Barry and Boniface [90] to determine interference effects. The integral of the forces on the fuselage surface in the flight direction is equal to the total fuselage drag and therefore also equal to  $T_{shaft,installed}$  for a force balance. In ANSYS Fluent an AD condition can be imposed on a surface

in which a jump in pressure and/or a jump in swirl velocity can be specified. This is often referred to as the 'fan boundary condition'. Because the propeller geometry and its properties in terms of swirl velocity and pressure increase are not known yet, these quantities need to be assumed. It is discussed in section 2.2 that the tangential velocity upstream of the propeller is negligible and is therefore assumed to be zero. The assumption for the pressure jump should be such that the corresponding thrust is equal to the  $D_{total}$  and its profile should represent a propeller operating in the boundary layer of the fuselage. Lv [94] proposes a pressure-jump profile such that the total pressure defect is recovered by the propeller. This profile may lead to the lowest required power of the propeller. In Smith [12] it is indicated that the lowest power is obtained by a 'full recovery' of the boundary layer, although no mention was made on the total pressure. Betz [11] and Plas et al. [95] noted that a condition in which all axial velocity is recovered, the thrust is equal to the drag. For a first order approximation of the upstream effect of the propeller the specified pressure jump is therefore assumed to be:

$$\Delta p_{fan}(y) = p_{t,0} - p_t(y) \quad (5.2)$$

By applying this condition, the total pressure defect in the boundary layer is completely recovered. This condition is implemented in the Fluent simulation by making use of a User Defined Function (UDF), developed by the author, which describes the boundary condition at the fan surface by taking the free stream value  $p_{t,0}$  and subtracting the local  $p_t(y)$  one cell upstream of the fan surface. The value of  $p_t(y)$  is determined using the isentropic relation for the pressure.

At the fuselage surface the physical limitation of producing a pressure jump exists as the velocity parallel to the surface is 0 and at the surface no pressure jump can be achieved. Therefore the a small region of the fuselage upstream and downstream of the fan is modelled as a slip wall as depicted in figure 5.3 (a) and is referred to as the spinner of the fan. In the three-dimensional blade this part of the fuselage is the spinner and is also modelled as a slip wall. Figure 5.3 (a) shows the effect on the inflow with a non-slip spinner surface and a slip spinner surface. The figure shows a negligible effect on both the inflow and hence this assumption will not have a significant impact on the results.

The fan boundary condition approach has a number of assumptions:

- The pressure profile of the fan has the largest  $\Delta p$  at the root. The optimised propeller does not necessarily produce this  $\Delta p$  as the  $\Omega r$  in the root region is small and the potential pressure jump may be expected to be moderate. Therefore this assumption might lead to an over prediction the  $\Delta D_{skin} + \Delta D_{pressure}$  as the pressure effect close to the fuselage is expected to be dominant.
- The pressure jump influences the complete boundary layer in circumferential direction. The actual propeller and its associated pressure on the suction side will produce a local effect on the fuselage, as shown in the CFD simulation on the N250 propeller (figure 4.7). Therefore the circumferential pressure jump does not necessarily represent the actual effect of propeller installation as a non-linear relation may be present between the pressure jump and the fuselage drag.
- The swirl velocity is assumed to be zero.

Figure 5.3 (b) shows the  $p_t/p_{t,0}$  distribution with and without a slip wall condition on the spinner. Downstream of the fan (see figure 5.3 (a) for the definition) the  $p_t$  is almost constant and has the same value as the gage value  $p_{t,0}$ , except in the very near wall region, where the wall functions of the turbulence model could influence the results. Figure 5.3 (c) shows the pressure just upstream and downstream of the AD. It is shown that the total pressure behind the AD is the freestream value. The figure also indicates that upstream of the fan the total pressure defect close to the fuselage surface is larger with the fan BC indicating an increased skin friction upstream of the propeller. The thickness of the boundary layer is not significantly changed by the fan. The integrated  $\Delta p_s$  over an area from the hub to the edge of the boundary layer is in this particular case 82.47 N and the total profile drag on the fuselage is 82.29 N which approximately is states an equilibrium condition. The edge in this particular calculation is assumed to be the radial location at which the  $p_t = 0.999p_{t,0}$ . The individual and total drag forces on the spinner and fuselage are listed in table 5.6. The table shows a quite significant contribution of the skin friction to the total drag, which may be expected for a non-lifting surface. The skin friction is only slightly increased in the AD simulation which is a result of the higher velocities upstream of the AD. The major contributor to the drag increase is the pressure drag on the fuselage surface. On the spinner surface the force is almost the same in both simulations. A visualisation of the pressure distribution on the fuselage surface is shown in figure 5.3 (f). The lower pressure from approximately  $\frac{x}{L_{fuselage}} = 0.90 \dots 0.95$  is the cause of additional drag.

Table 5.6: Comparison of  $D_{fuselage}$  and  $D_{spinner}$  from a CFD simulation using an isolated fuselage and an Actuator Disk.

Method	Type of drag	$D_{spinner}$ [N]	$D_{fuselage} - D_{spinner}$ [N]	$D_{fuselage}$ [N]
CFD (isolated fuselage)	$D_{skin} + D_{pressure}$	-7.59	81.69	74.10
	$D_{skin}$	0.00	67.76	67.76
CFD (actuator disk)	$D_{skin} + D_{pressure}$	-7.44	89.64	82.29
	$D_{skin}$	0.00	67.83	67.83

To estimate the additional interference drag due to a higher thrust setting than a force balance, the same approach is used as described above with a larger pressure jump than the defect in total pressure:  $\Delta p_{fan}(y) = [p_{t,0} - p_t(y)]f$ . In this relation  $f$  is the fraction of additional thrust, i.e. 1.10 for a 10% higher thrust setting. This distribution assumes that the additional thrust distribution is proportional to the radial loading. A thrust to drag ratio of 1.50 did not lead to a converged solution of the CFD simulation, likely due to the very large pressure jump close to the fuselage surface. Thrust to  $D_{installed}$  ratios up to approximately 1.35 lead to a converged solution. It should be stressed that the  $D_{installed}$  is assumed to be constant in these simulations as in reality the drag is increased leading to a lower net force. Some values of the additional interference drag are listed in table 5.7. It may be observed that the increase in fuselage drag is significantly smaller than the additional thrust. There is no difference in additional interference drag between 25% and 35% excess thrust. Figure 5.3 (e) shows the  $C_p$  distribution along the aft fuselage for the different thrust settings. It is shown that the shape of  $C_p$  remains approximately the same for the larger pressure jumps and there is only a marginal deviation from the  $f = 1.00$  situation in the region  $\frac{x}{L_{fuselage}} = 0.90...0.95$ .

Table 5.7: Effect of an additional thrust requirement on the total fuselage drag modelled with an Actuator Disk in a similar approach as section 5.4 describes. The additional pressure jump is taken proportional to the total pressure defect.

$\frac{T}{D}$	$\frac{D_{fuselage}}{D_{fuselage, T=D}}$
1.00	1.000
1.25	1.015
1.35	1.015

Figure 5.3 (d) shows the distribution of  $Tu$  for with different reference velocities. The figure shows that especially close to the root the turbulence intensity is high and transition can be expected very close to the leading edge. It is shown that the turbulence intensity is reduced when the fan is installed. This is primarily the result of the higher axial velocity induced by the fan which reduces the relative fluctuations.

A number of marine propeller design studies (e.g. [93, 96]) and aircraft propeller design studies (e.g. [24]) have use the concept of an 'effective wake'. The effective wake is the corrected inflow which models the interaction between the propeller and nominal (or uninstalled) inflow by taking the uninstalled inflow and subtract the induced velocity by the propeller. This method indicates that the propeller not only changes the boundary layer by the induced velocities but there can be an additional effect which deforms the boundary layer. In e.g. Choi and Kinnas [93] the effective wake is computed with an AD and good agreement with experiments was found. A similar method can be used in this setup. Figure 5.3 (f) shows the velocity profiles upstream and downstream with and without the AD. In addition the estimated induced velocities based on the  $\Delta p(r)$  are calculated using momentum theory [28]. The figure shows that downstream of the AD the induced velocities are slightly different than these predicted values. Therefore the effective wake is the uninstalled velocity profile corrected for this small deviation, as shown in the figure. The effective wake has a slightly higher axial velocity than the uninstalled case. The deformation of the velocity profile may therefore be considered as a secondary effect. For design purposes, the uninstalled velocity profile is used instead of the effective wake. The effective wake is only used for comparison purposes explain differences in the computational fluid dynamics simulation of the actual designed blade.

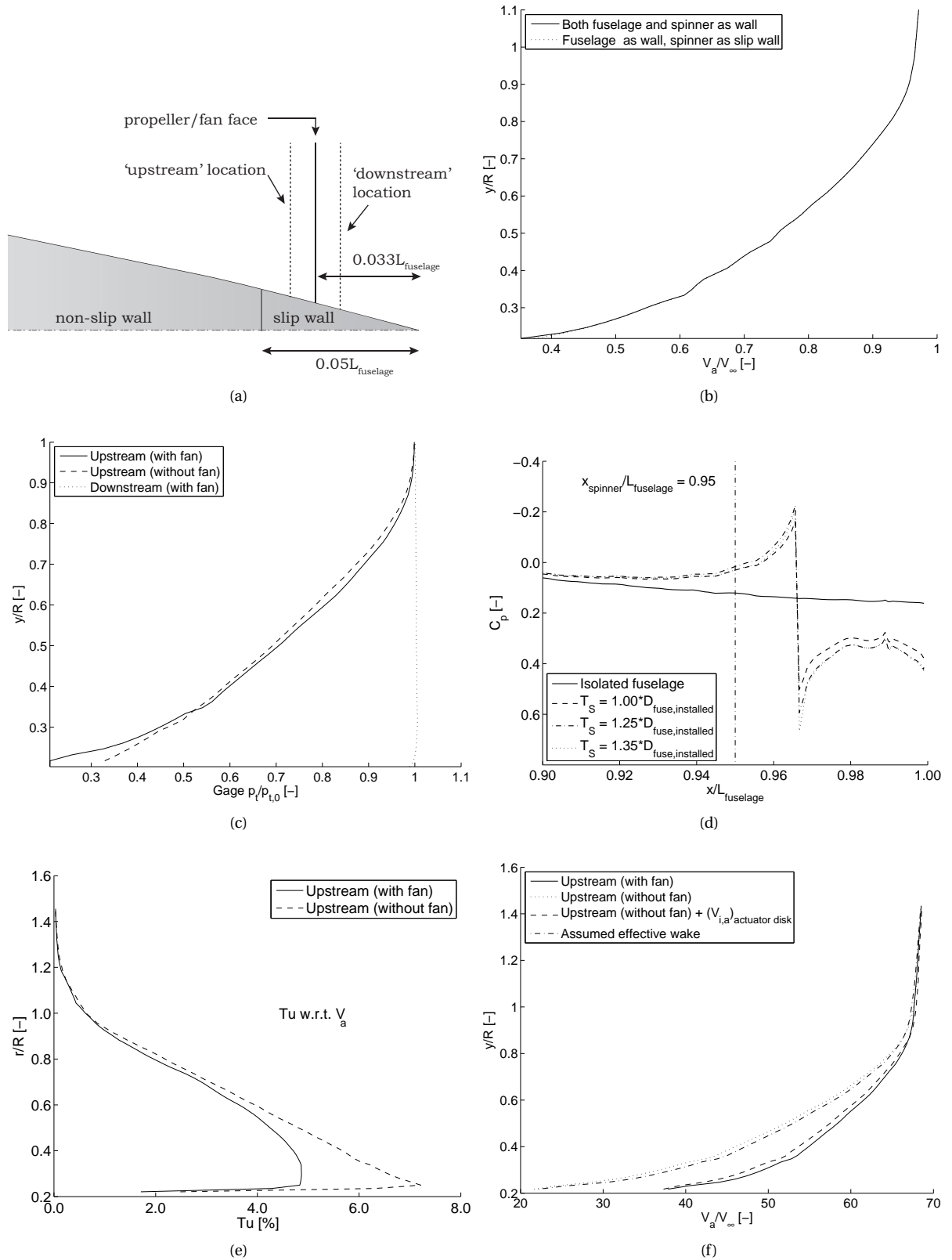


Figure 5.3: The effect of a non-slip wall boundary condition at the aft-fuselage and a slip wall boundary condition in (a). The effect of a fan boundary condition on the total pressure (b) and the velocity profile (c) just upstream of the propeller location. The propeller is modelled by a pressure jump equal to the defect in total pressure. The pressure values are gage pressures. In (d) the effect of the fan on the  $C_p$  distribution. The effect on the turbulence intensity is shown in (e) and the effective wake is shown in (f).



# 6

## OPTIMISATION RESULTS

This chapter describes the optimisation results of the non-uniform inflow propeller subject to the reference inflow described in the previous chapter. The results are compared with a propeller with uniform inflow. As both uniform inflow and non-uniform inflow have a design thrust equal to the fuselage drag, they have different design thrusts. First the case discussed in section 2.1 in which the effect of a reduced uniform inflow of  $V_\infty$  on the propeller performance is investigated in more detail in section 6.1. Those optimisations have close relation with the remaining optimisations in this chapter. The design condition is summarised in section 6.2. Section 6.3 then describes the results obtained for non-uniform inflow. Some additional results related to design variables such as the number of blades, thrust requirement and radius are compared for uniform and non-uniform inflow in section 6.5.

### 6.1. EFFECT OF UNIFORM $V_\infty$ ON REQUIRED POWER

In section 2.1 it was shown that for a given thrust, propeller diameter and  $\rho$  the power reduces with reducing  $V_\infty$  based on the momentum and kinetic energy relations. These curves do not include effects as profile drag, swirl and the effect of a finite number of blades which limits the loading at in the tip region by tip loss effects. An interesting question is whether optimised propellers follow the same trend as predicted by the momentum and kinetic energy relations.

A series of optimisations are performed to compare with the curves plotted in section 2.1 with the same boundary conditions:

- The design thrust  $T$  is kept constant with  $T = D_{isolated} = 74.20 [N]$ .
- A NACA0006 airfoil is used.
- The radius  $R = 0.2404 [m]$  and hub radius  $R_{hub} = 0.0530 [m]$  are taken as the radii of the propeller of interest.
- Standard atmospheric conditions are used.
- A constant  $J = 1.50$  is used.

Figure 6.1 (a) shows the required power for a number of optimised propellers at different design  $V_\infty$ . Each data point represents an individually designed propeller. The same trend is followed as the predicted performance by the momentum theory and all optimal designs require a slightly higher power than the simple momentum theory predicts, which is expected as losses due to tangential velocities and profile drag are induced. The momentum theory provides the lower limit on the  $P - V_\infty$  curve. As expected, the induced velocities are increasing with reducing advance ratio as shown in figure 6.1 (c). Figure 6.1 (a) shows that the optimal designs lie approximately on a linear trend, but this trend has a higher slope compared with the simple momentum theory. A possible way to explain this different slope is by looking at the relative distributions of the axial and tangential trailing edge vorticity as discussed in section 2.2. The ratio of  $\frac{\gamma_a}{\gamma_t}$  is shown in figure 6.1 (c). For the higher freestream velocities, the axial vorticity  $\gamma_a$  relative to the tangential vorticity  $\gamma_t$  is significantly higher. Therefore the vorticity inducing a swirl is relatively high for high  $V_\infty$ .

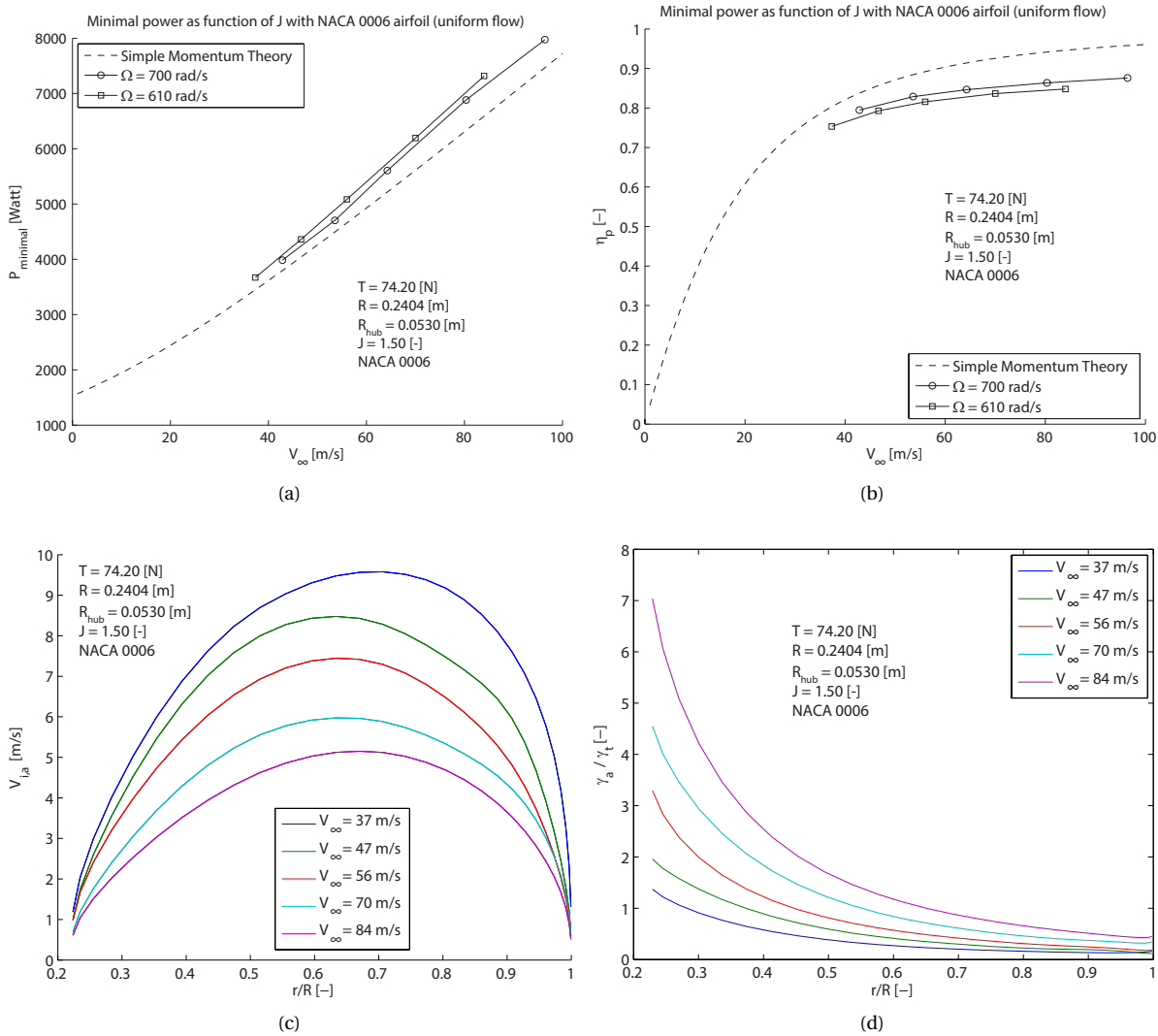


Figure 6.1: The effect of  $V_\infty$  on the power (a), efficiency (b), axial induced velocity (c) and axial to tangential vorticity ratio in (d) for uniform inflow propellers. Each data point and distribution corresponds to a unique design. The power and efficiency are compared with momentum theory.

## 6.2. DESCRIPTION OF DESIGN CONDITION

To make the comparison between the two propellers, the following quantities are kept the same for both optimisations:

- The **radius**  $R = \delta_{99}$  and  $R_{hub} = 0.0530$  [m] for both cases. The  $\delta_{99}$  is determined by the total pressure profile in the boundary layer at the plane of the propeller. This condition is set for the design condition as it is expected that a reduced velocity leads to a good thrust to power ratio and all relatively low velocity is 'used' to produce thrust. A finite hub radius of approximately  $0.20R$  is a reasonable value for uniform inflow propellers and shows a feasible position at the aft fuselage as discussed in section 5.1.
- The **advance ratio**  $J = 1.50$  for both cases. The reason for keeping the advance ratio, i.e. in this case the  $\Omega$ , equal is that the previous section showed that in general a higher tip speed leads to a lower power for the same thrust. Tip speeds also limit the operational use due to noise production [30] and drag divergence. This means that both propellers have the same limit in terms of tip Mach number. The actual axial speed in the non-uniform inflow case is  $0.98V_\infty$  due to the induced velocity of the fuselage and a tip advance ratio may be used to correct for this small effect. However, the  $\Omega$  is not corrected to have exactly the same helical tip Mach number. A particular value of  $J = 1.50$  is chosen as

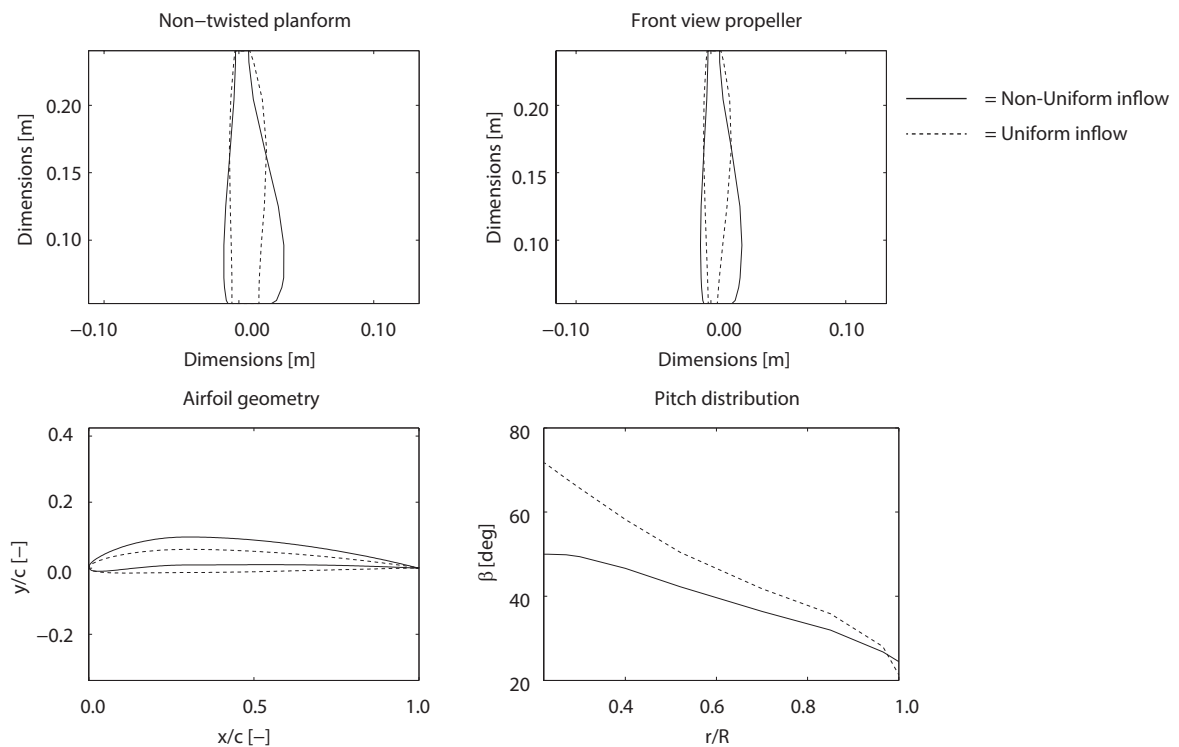


Figure 6.2: Optimised geometry of the non-uniform inflow propeller

it represents a reasonable helical tip Mach number of approximately 0.50, in which the Prandtl-Glauert compressibility correction is still reasonably accurate. A further analysis of the effect of  $J$  is provided in section 6.5.

- The **number of blades**  $B = 4$ . This will lead to a higher loading per blade in the non-uniform inflow case. By keeping the number of blades equal, the effect of this higher thrust requirement can be observed in the distributions. The effect of the number of blades on the propeller performance is discussed in section 6.5.

### 6.3. DISCUSSION OF RESULTS

This section discusses the optimisation results for the Non-Uniform Inflow (NUI) propeller compared with the optimised propeller for uniform flow. Table 6.1 shows the required power for the optimised propeller in uniform flow and the NUI propeller. A power benefit of 6.93% is predicted by N-XROTOR. To put this value in perspective, if the estimated interference drag of 11% (section 5.4) would have been zero, the estimated power benefit could have been in the order of 18% when a linear relation between power and thrust is assumed. However, a benefit of almost 7% shows a considerable advantage of placing the propeller in the non-uniform and reduced velocity field. The geometries of the optimised propellers are shown in figure 6.2. The chord distribution is such that there is a significant increase of  $\frac{c}{R}$  in the root region with respect to the uniform inflow design. The corresponding airfoil is a NACA 5309 which is a highly cambered airfoil and is relatively thick and this allows for a high maximum lift coefficient. The benefit of camber, which is a  $C_{d,0}$  at a non-zero  $C_l$ , is clearly utilised.

Table 6.1: Results of optimised propellers for uniform and non-uniform inflow with  $B = 4$ ,  $J_{tip} = 1.50$ ,  $V_\infty = 70[m/s]$  and  $R = \delta_{99}$ 

Inflow	Power [watt]	Benefit [%]
Uniform inflow	5986	-
Non-uniform inflow	5567	6.93

Some relevant radial distributions are shown in figures 6.3 (a) through (f). In (a) the distributions of  $\Gamma_B$  are shown and the ratio of thrust to power is shown in (b). The location of the maximum circulation of the NUI propeller is shifted inboard compared with the uniform inflow propeller and its magnitude is increased. The thrust to power ratio  $\frac{dT}{dP}$  or  $\frac{dT}{dQ\Omega}$  is higher over the majority of the radius and is significantly higher in the root region compared with the distribution of the uniform inflow. The circulation is increased towards the hub because in this region the low  $V_a$  results in a favourable high thrust to power ratio. This is in line with the theory discussed in section 2.1. In order to shift the loading towards the root and benefit most from the high thrust to power ratio, a high lift is required. Because the local velocity is relatively low, a high circulation is required as the thrust is proportional to  $\rho\Gamma V_{eff}$ . To accomplish the high circulation towards the root, the  $\frac{c}{R}$  is relatively large in this region as shown by the geometry. In figures (c) the local efficiency over the blade is plotted. The local efficiency of the NUI propeller is decreased in the root region, in line with the predicted trend in section 2.1. The local efficiency distribution for the uniform flow is (nearly) constant, as expected from optimal flow for uniform inflow. Minor differences may be the result of design freedom, set by e.g. the number of coefficient as shape function.

The axial and tangential induced velocities with respect to  $V_\infty$  are shown in figures 6.3 (d) and (e). As may be expected from momentum theory, the axial induced velocity of the NUI propeller is higher in absolute sense to meet the thrust requirement. The distributions are very similar to the  $\Gamma_B$  distributions. The tangential induced velocity shows a maximum very close to the hub. This can be explained by a relatively large  $\frac{d\Gamma_B}{dr}$  which leads to a region of increased vorticity which induces a tangential velocity. It may be observed that the ratio of  $\frac{V_{i,a}}{V_{i,t}}$  is in favour of the NUI propeller in the root region. This is closely related to the direction in which the vorticity is shed, which is visualised in figure 6.3 (f). The ratio  $\frac{\gamma_a}{\gamma_t}$  shows to be relatively constant for the NUI propeller and shows a great rise for the uniform inflow propeller in the root region. This means quite a large axial vorticity is present (leading to tangential velocities) relative to the axially induced velocities (induced by  $\gamma_t$ ).

The beneficial thrust to power ratio of the NUI propeller can also be seen in the thrust and torque distributions, in figures 6.4 (a) and (b) respectively. The position of largest thrust is shifted inboard and is slightly decreased in magnitude, even though the thrust of the propeller is 11% higher. From the hub to  $\frac{r}{R} \approx 0.6$  the torque is only slightly higher in the NUI case but the thrust is clearly significantly larger.

Besides the increased fuselage drag caused by the propeller, there is also benefit in positioning the propeller close to the fuselage by looking at the potential flow induced by the fuselage. The fuselage induces a radial flow component which reduces the axial flow component at the propeller location. In the tip region of the NUI propeller the  $\frac{dT}{dQ\Omega}$  is slightly higher than the uniform propeller shows. This is because the velocity at the edge of the boundary layer is not equal to  $V_\infty$  but is slightly lower, as sketched in figure 6.5.

The airfoil of the NUI propeller is relatively thick compared with the airfoil of the uniform inflow propeller. The lift coefficient distribution is shown in figure 6.4 (c). The figure shows a relatively high lift coefficient for the NUI propeller. To obtain the high circulation in the root region, the quantity  $C_{l,c}$  should be high. When a high  $C_l$  is desired by the optimiser, the airfoil should allow for this value. The constraint of  $C_l \leq C_{l,nonlinear}$  results in a relatively thick airfoil, which have the property of high  $C_{l,nonlinear}$ . The lift to drag ratio of the designed airfoil at the location of the highest circulation ( $\frac{r}{R} = 0.52$ ) is shown in figure 6.4 (d) and the lift coefficient at that radial location is indicated. The figure shows a favourable  $\frac{C_l}{C_d}$  at relatively high lift coefficients and the designed blade has a  $C_l$  close to the highest lift to drag ratio and is limited by the constraint on  $C_l$ . In general, it is desired that all airfoil sections operate at their optimum lift to drag ratio [97]. The figure shows that this is not the case at  $\frac{r}{R} = 0.52$ . This may be explained by a number of effects. First the highest  $C_l$  along the blade is slightly higher than the value at the highest circulation. In addition, profile drag is only a minor contributor to the total torque. Hence the optimal solution is much more sensitive to the  $C_l$  distribution along the blade than the  $C_d$  distribution. The optimiser tries to find a reasonably good airfoil which has a good  $\frac{C_l}{C_d}$ , but it is likely that any changes to the airfoil geometry do lead to a better  $\frac{C_l}{C_d}$  value along the blade but is not recognised by the gradient based optimiser. Also, when the changes are finite but small, rounding off errors in e.g. XROTOR and XFOIL can lead to no changes in the gradient of the airfoil properties to the design vector. In addition, it may be suggested that multiple airfoils are used instead of one airfoil such that the distribution of a non constant  $C_l$  results in a better  $\frac{C_l}{C_d}$  distribution.

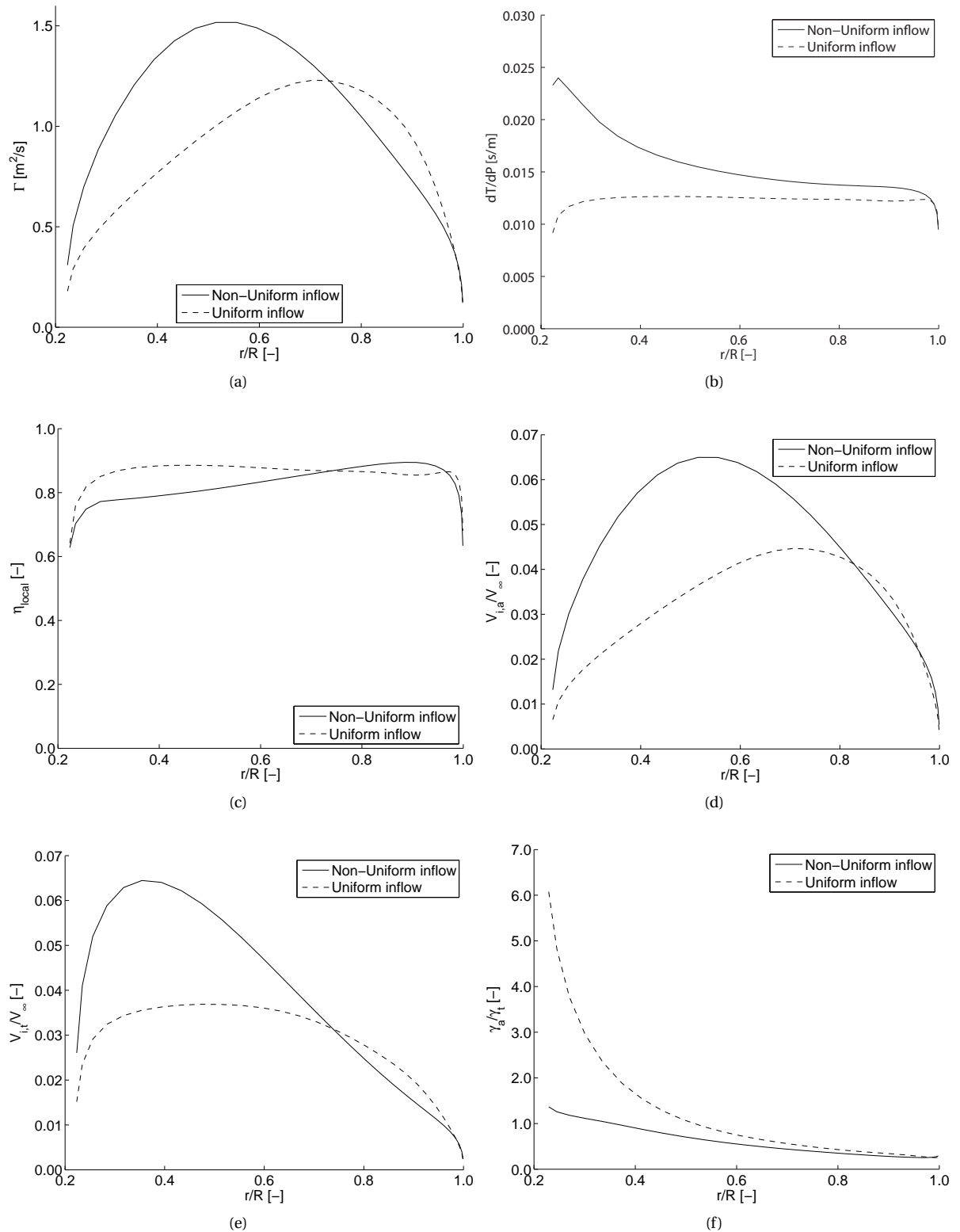


Figure 6.3: Distributions of a propeller optimised for uniform inflow and a propeller designed for non uniform inflow.

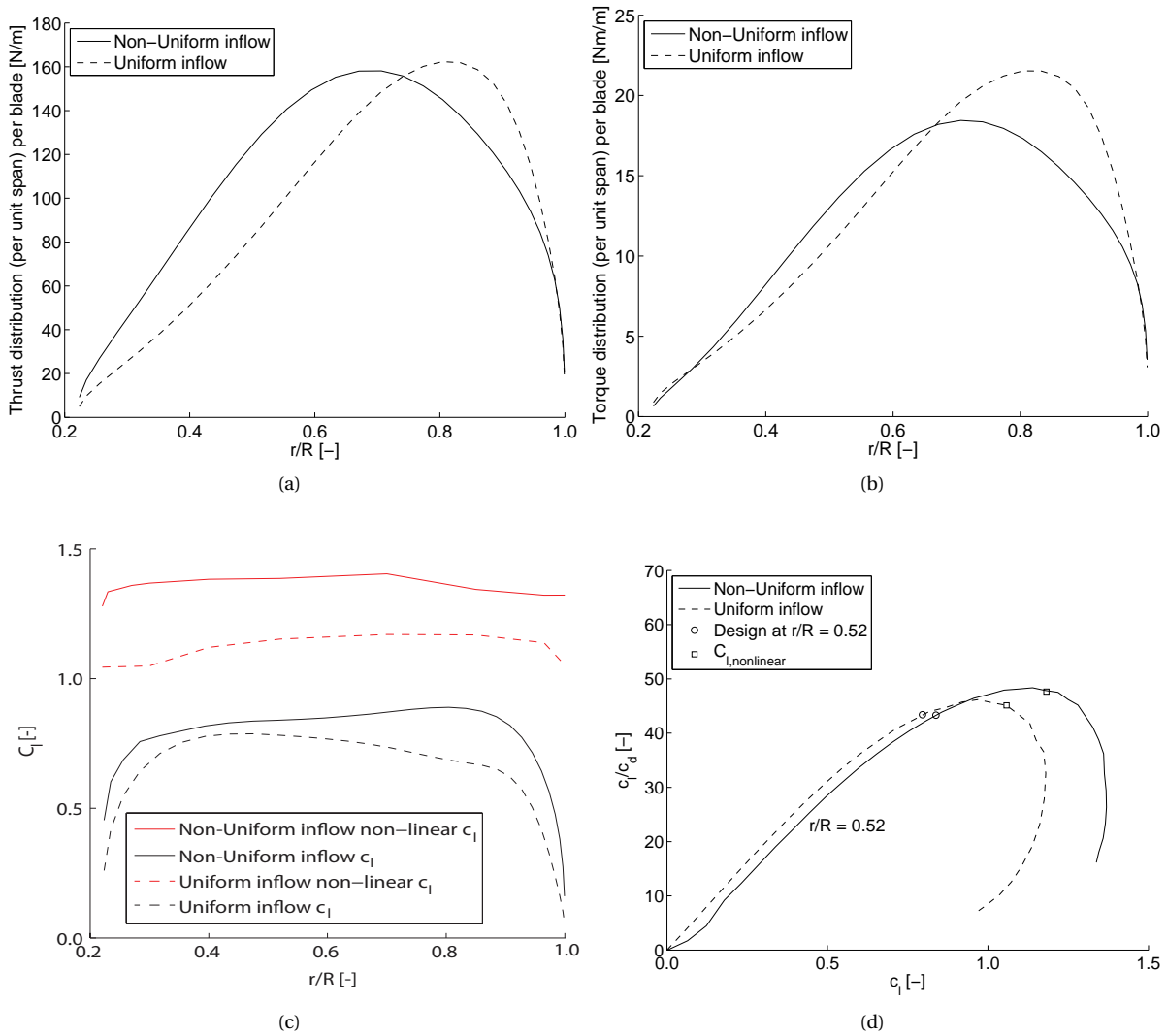


Figure 6.4: Comparison of thrust (a) and torque (b) distributions of the designed propellers for non-uniform and uniform inflow. The distributions of lift coefficient distribution in shown in (c). The lift to drag ratio of the airfoil at  $r/R = 0.52$  is shown in (d) with the lift coefficient at that position indicated.

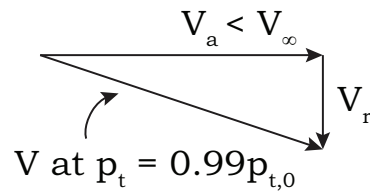


Figure 6.5: Effect of the radial flow on the axial flow at the edge of the boundary layer. The radial flow component at the edge of the boundary layer causes the axial flow to be lower than the free stream flow.

## 6.4. PERFORMANCE GRAPHS

The performance of the propeller in off-design condition is considered in this section. By varying  $J$  for the same propeller design a performance map can be created for both the uniform and non-uniform inflow propellers. These curves indicate the sensitivity to off design conditions. A variation in  $\Omega$  is chosen as parameter to vary  $J$ .

Figures 6.6 (a) and (b) show the performance maps. The general observation is that both designs have a large range of advance ratios in which the thrust coefficient is linear. The slope of the  $C_T$  curve is higher for the uniform inflow propeller. Generally this can be considered as a higher lift curve slope when the rotational speed is varied. The uniform inflow propeller experiences a higher Mach number on average over the blade. When the Mach number is increased due to increasing  $\Omega$ , the compressibility correction leads to a relatively high lift curve slope for the uniform inflow case. This is because  $C_{l,\alpha}$  is not linear with Mach number. The non-uniform inflow propeller also increases its lift curve slope, however at a lower rate than the uniform inflow propeller. The  $C_P$  curve is strongly linked to the  $C_T$  curve and therefore shows a diverting curve due to this effect.

The thrust to power curve shown in figure 6.6 (c) shows that the uniform inflow propeller is designed close to the highest value of  $\frac{T}{P}$ . The non-uniform inflow propeller shows an offset which is approximately constant for  $J \leq 1.50$ . For higher advance ratios, the thrust to power ratio increases which is increasing the offset.

In figure 6.6 (d) the quantity  $\frac{C_T J}{C_P}$  is plotted. For the uniform inflow propeller this is generally the same as the propulsive efficiency. For the non-uniform inflow propeller, this definition leads to values above unity, as shown in the figure. This figure shows that the definition yields to unrealistic values as the propeller does work on the local flow and not on the free stream flow.

## 6.5. ADDITIONAL OPTIMISATION RESULTS

This section provides additional optimisation results to provide insight in the effects of an additional thrust requirement, the number of blade, tip advance ratio and propeller radius on the required power. The results include optimisation results for both uniform and non-uniform inflow propeller designs. It is noted that each of the data points represent a unique propeller design. For each parameter the most prominent and relevant distributions are shown to explain the phenomena.

### 6.5.1. DESIGN WITH EQUIVALENT VELOCITY

An interesting case is to compare the distributions and when the non uniform inflow is converted to a uniform inflow profile with equal mass flow. This comparison provides insight in the benefit of the shape of the boundary layer inflow, in addition to the reduced inflow field.

With the density assumed to be constant, the equivalent velocity is:

$$V_{equivalent} = \frac{2}{R^2 - R_{hub}^2} \int_{R_{hub}}^R V_a(r) dr \quad (6.1)$$

In table 6.2 it is shown that a propeller designed for uniform flow and with the free stream flow equal to the equivalent velocity results in a reduction in power of 3.87% compared with the propeller designed for  $V_\infty$ . This means that the non-uniformity of the inflow is beneficial for the propeller. It is expected that this benefit comes from the direction of the vortex sheets which are more constant along the blade (section 2). Figure 6.7 shows the distributions of thrust to power for these three conditions.

Table 6.2: Effect on the power by designing a propeller with a uniform inflow which has the same mass flow as the non-uniform profile of the boundary layer.

Design condition	Benefit w.r.t. uniform inflow
Non-uniform	6.93 %
Uniform with $V_{equivalent}$	3.87 %

### 6.5.2. EFFECT OF ADDITIONAL THRUST

In addition to the fuselage more drag producing components are fitted to the fuselage such as wings and tail planes. Therefore an interesting case is to compare the required power for the uniform and non uniform inflow propellers when they are designed for a higher thrust than the drag of the fuselage.

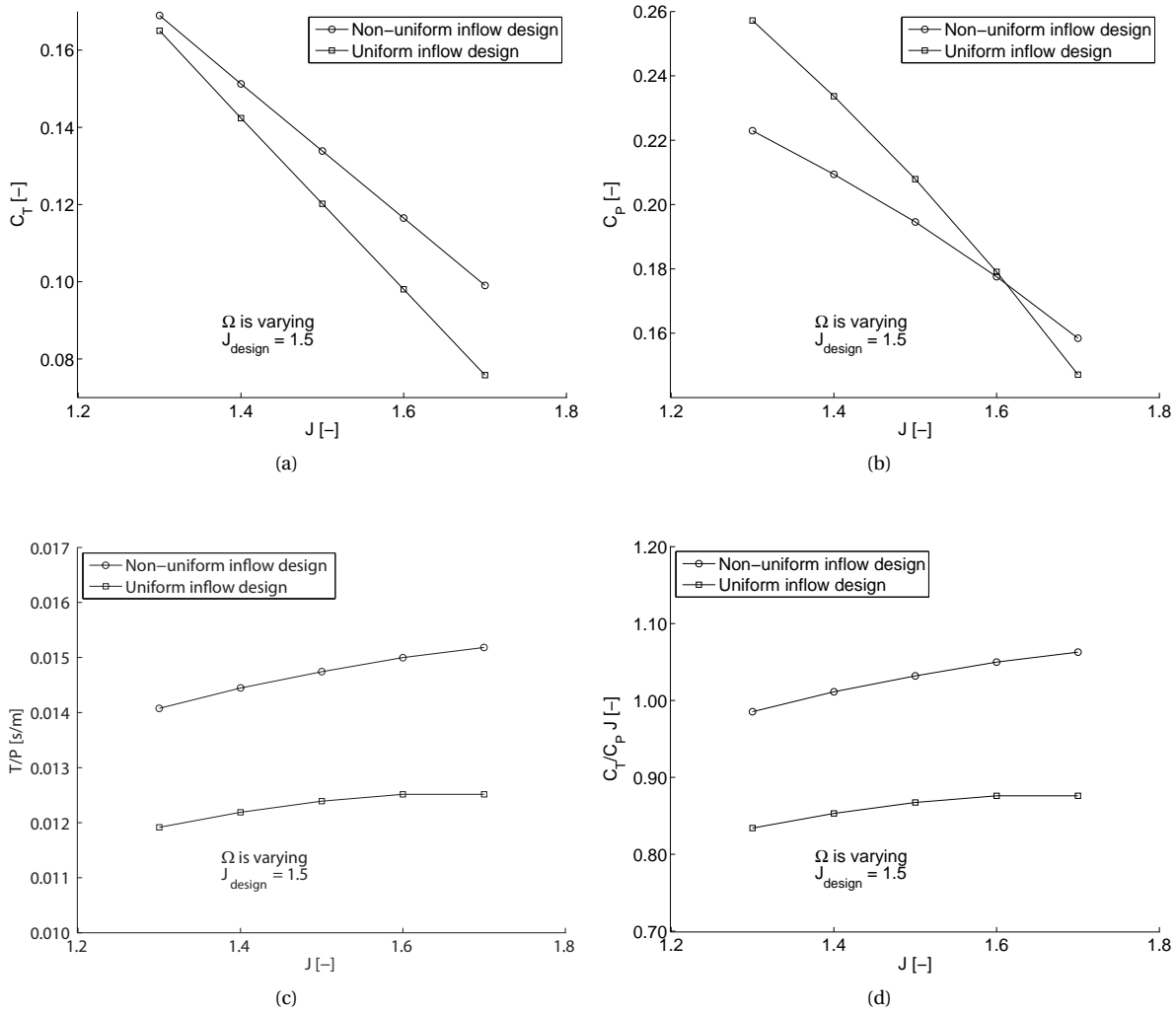


Figure 6.6: Performance curves of the designed uniform and non-uniform inflow propellers. A varying advance ratio is obtained by varying  $\Omega$ .

For this case all operating conditions are equal to the reference cases in section 6.2. The uniform inflow propeller is designed at  $1.25 \cdot T_{ref}$  and  $1.50 \cdot T_{ref}$  in which  $T_{ref} = D_{isolated}$ . The non uniform inflow propeller is designed for with a thrust requirement of  $1.25 \cdot T_{ref}$  and  $1.50 \cdot T_{ref}$  in which  $T_{ref} = D_{isolated} + \Delta D_{skin} + \Delta D_{pressure}$ . This means that the  $T_{ref}$  is constant, independent of the thrust setting and it is assumed that the additional thrust does not induce an additional  $\Delta D_{skin} + \Delta D_{pressure}$ . A more realistic case is to include the additional interference drag which comes from the additional thrust. The small increase in interference drag means that at higher thrust settings the benefit of the installed non-uniform inflow is slightly decreased. Section 5.4 shows that this effects is small.

The results of individually designed propellers are shown in figure 6.8 (a), in which the ratio of power required to the power required of the uniform inflow case at  $T_{ref} = D_{isolated}$  is plotted. A linear increase in power with a higher thrust requirement is shown for the uniform inflow propeller and the NUI propeller (without taking into account the increased interference drag). Because these two trends are linear it is shown that there is a constant and absolute benefit in terms of power possible using the NUI propeller when the interference drag is kept the same. The uniform inflow case shows an increase in bound circulation with a higher thrust requirement as shown in figure 6.8 (b). The shape of the distribution is almost not altered, meaning that there are no limitations in terms of stall or induced velocities restricting this distribution. For the non uniform inflow approximately the same is the case, except the  $\frac{T}{T_{ref}} = 1.25$  shows a relatively large circulation in the root region which has about the same magnitude as the  $\frac{T}{T_{ref}} = 1.50$  case. This may indicate

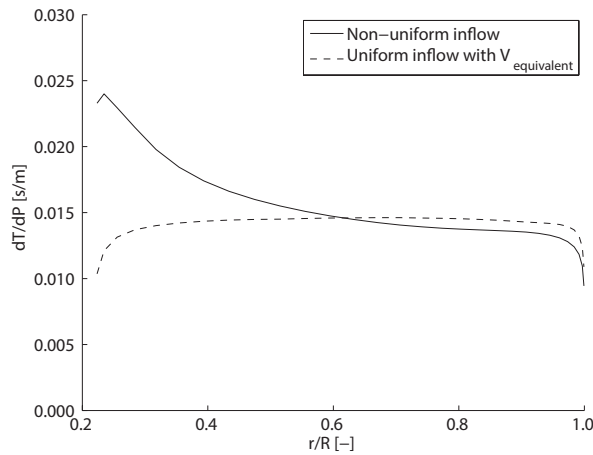


Figure 6.7: Effect on the thrust to power ratio along the blade when a propeller is designed with uniform inflow velocity  $V_{equivalent}$  which results in the same mass flow as the non-uniform inflow profile.

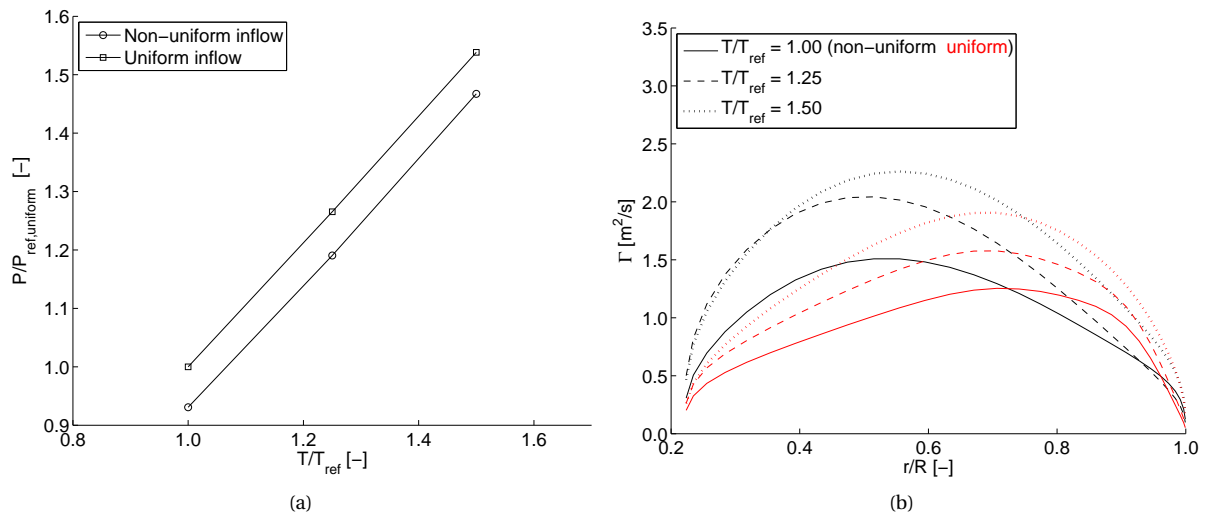


Figure 6.8: Effect of the a different design thrust on the required power in (a) where each data point represents an optimised design. The reference thrust is equal to the force balance situation. In (b) the effect on the circulation distributions is shown.

that the  $\frac{T}{T_{ref}} = 1.50$  experiences slight limitations in the root region in terms of stall characteristics, in which it is difficult to obtain a very high lift coefficient in order to get a high circulation.

### 6.5.3. EFFECT OF NUMBER OF BLADES

Apart from considerations such as noise and structural properties of the blade, the number of blades directly dictates the thrust per blade. The relation between the number of blades and the power is an interesting case, as on the one hand a low number of blades may lead to lower profile losses due to a reduced skin friction but both the induced losses and pressure drag may increase. As noted in section 3.1, the number of blades is equal to the number of vortex sheets that trail from the lifting line. Around the edge of a vortex sheet the flow tends to flow around the edge causing a radial flow component and making the blade tip less effective [10]. This effect is reduced with a higher number of blades at for the same thrust setting.

Figure 6.9 (a) shows the required power of an optimised NUI propeller for several values of  $B$ . It can be seen that  $B = 4$  is the optimal amount of blades (although  $B = 3$  and  $B = 5$  are not considered) for both uniform and non-uniform inflow, which is equal to the design condition. The reference case of section 6.2 also has four blades. To obtain a required total thrust, a method is to reduce the chord length. In terms of design properties, the most apparent change in geometry is a reduced  $\frac{c}{R}$  with increasing blades. The lift to drag ratio is dependent of airfoil geometry but may not differ significantly between designs.

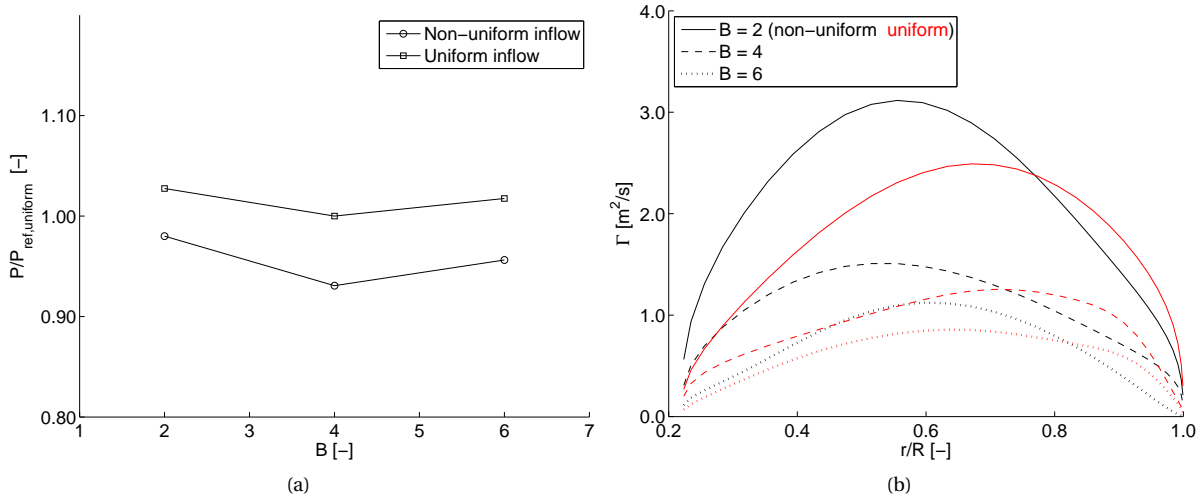


Figure 6.9: Effect of the number of blades  $B$  on the required power in (a) where each data point represents an optimised design.

The figure shows that the uniform inflow propeller has a trend of a higher circulation shifted towards the tip with increasing number of blades, which is in line with the theory of a lower tip loss with more blades [10]. A higher number of blades also leads to a larger effect of each blade onto the other blades in terms of circulation and induced velocities. The same trend of shifting the circulation towards the tip is followed in both the uniform and non-uniform inflow cases.

A low number of blade for a given thrust requires a relatively large  $C_{1c}$ . This leads to relatively high induced velocities. A very large number of blades for a moderate thrust leads to excessive profile drag due to the number of blades. It can be seen that in this particular case  $B = 4$  is a good balance as in both uniform and non-uniform optimal designs this is the number of blades with the lowest required power.

#### 6.5.4. EFFECT OF ADVANCE RATIO

As discussed in section 6.2, the design condition of both uniform and non-uniform inflow is equal  $J = \frac{V_\infty}{nD}$  and is set to 1.50. Assuming the axial velocity at the tip of the non-uniform inflow is  $V_\infty$ ,  $\Omega$  is constant between the conditions.

The trend of power as function of  $J_{tip}$  for three tip advance ratios is shown in figure 6.10 (a). This figure shows a decreasing required power with decreasing  $J_{tip}$  (or increasing  $\Omega$ ). A similar behaviour is shown for uniform inflow propellers in section 6.1. The trend shows that the design condition at  $J = 1.50$  is not an optimum. The thrust to power ratio in figure 6.10 (b) shows no clear trend over the complete blade. In the region  $\frac{r}{R} = 0.40..0.80$  the trend is a higher  $\frac{dT}{dP}$  with lower  $J$ . In the root and tip regions this trend is not followed for the advance ratios considered. There is no clear identification of why there is no distinct trend in these regions.

#### 6.5.5. EFFECT OF TIP RADIUS

For all previous results the radius was taken as  $\delta_{99}$ . It was shown that the non-uniform inflow propeller has a much better thrust to power ratio in the inner radii. Therefore it is of interest to design the propellers at different radii as well to analyse the effect of this constraint. The  $\Omega$  is adjusted to maintain the same  $J$ .

In figure 6.11 (a) is shown that both a smaller radius and a larger radius than  $\delta_{99}$  lead to a lower required power of the non-uniform inflow propeller. A smaller radius leads to a lower axial inflow velocity along the blade hence the tip region with a low thrust to power ratio is not used to produce a thrust. Larger radii have the benefit of a large disk area which requires a smaller induced velocity to meet the thrust requirement. For uniform inflow propellers generally a lower power is required for the same thrust. A similar behaviour is seen for the non-uniform inflow propeller as the required power is slightly reduced. This is shown as a slightly higher  $\frac{dT}{dP}$  ratio along the blade with a  $R = 1.10\delta_{99}$  (figure 6.11). The smaller radius yields a higher  $\frac{dT}{dP}$  in the tip region compared with  $R = \delta_{99}$ . The circulation distribution (shown in figure 6.11 (c)) shows that both a larger and smaller  $R$  yield a higher circulation in the root region. This may be explained by two effects. The

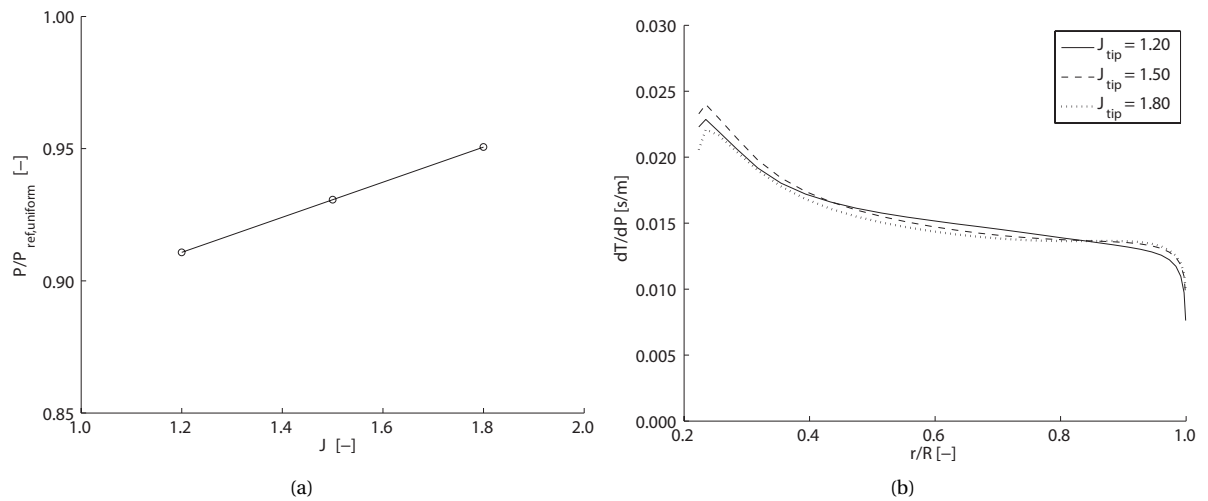


Figure 6.10: Effect of the tip advance ratio  $J_{\text{tip}} = \frac{V_{\infty}}{nD}$  on the required power in (a) where each data point represents an optimised design. In (b) the effect on the thrust to power ratio along the blade

smaller radius requires a larger loading as the thrust requirement should still be met. This results in a higher circulation. The larger radius experiences a lower  $\Omega$  and, to maintain the thrust, the circulation should be increased in a region with a favourable  $\frac{dT}{dP}$ .

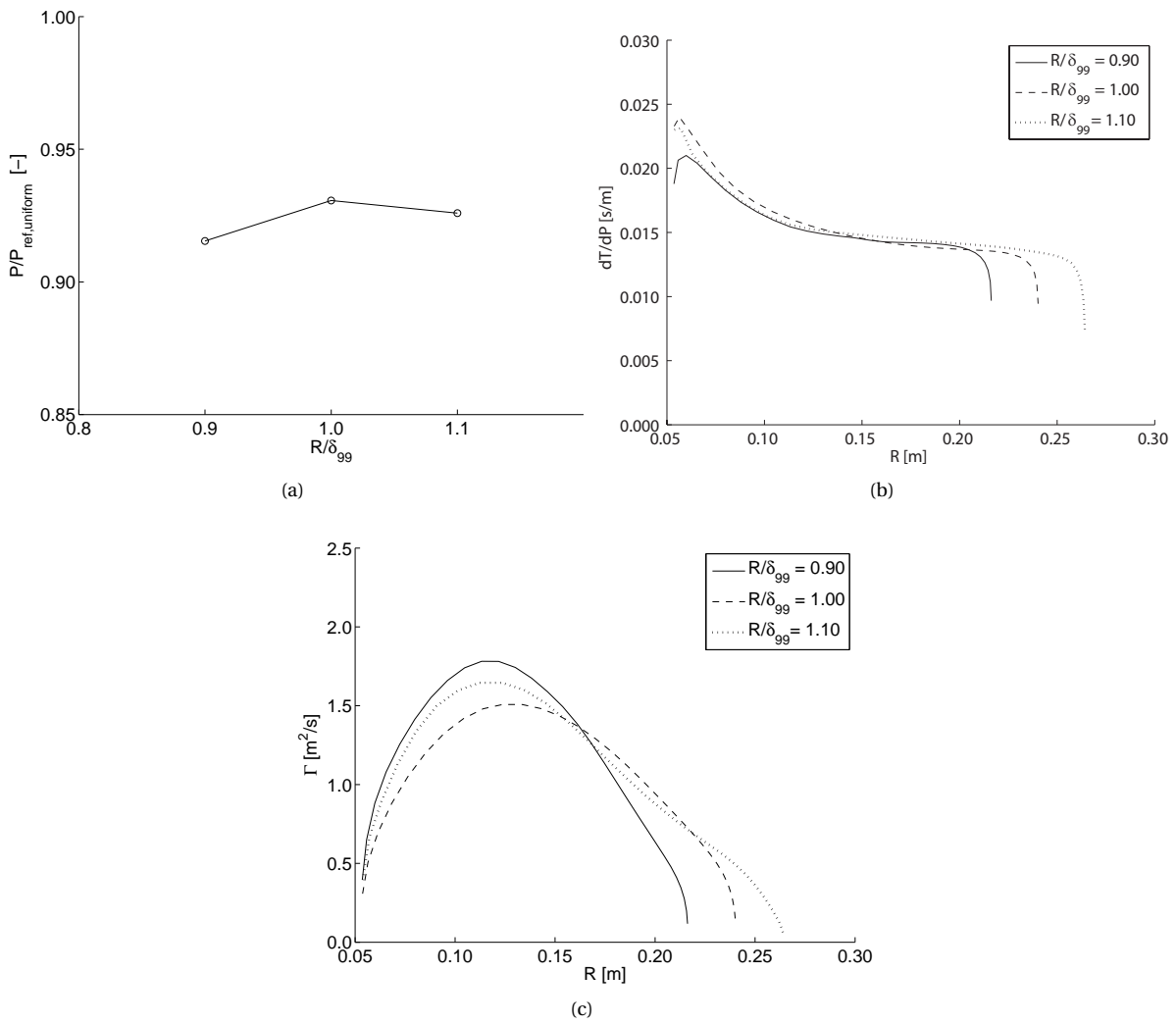


Figure 6.11: Effect of the propeller radius on the required power in (a) where each data point represents an optimised design. In (b) the effect on the thrust to power ratio along the blade and in (c) the effect on the bound circulation.

# 7

## CFD ANALYSIS OF OPTIMISED PROPELLER

This chapter describes the Computational Fluid Dynamics (CFD) analysis of the optimised propeller installed at the aft fuselage. The purpose of these simulations is threefold; first the capability of N-XROTOR for non-uniform inflow in terms of performance quantities and the prediction of the radial distributions can be analysed. Additionally a more detailed flow field around the non-uniform inflow (NUI) propeller is constructed and finally the estimated fuselage-propeller interaction from the actuator disk model can be compared with the full fuselage-propeller CFD model. Where possible, the computational settings are the same as for the N250 CFD simulation.

### 7.1. COMPUTATIONAL SETUP

The computational settings for the propeller-fuselage simulation are in line with the previous CFD analysis on the N250 propeller and the fuselage simulation in section 4.2 and Chapter 5 respectively. In section 4.3.4 the Multiple Reference Frame (MRF) method has shown under predictions of the performance quantities of approximately 1% compared with the time consuming transient sliding mesh approach. Therefore the MRF method is used for the fuselage-propeller simulations.

The four bladed propeller allows for a domain consisting of a 90° wedge using periodic boundary conditions as shown in figure 7.1 and the domain size is equal to the isolated fuselage simulation. The domain of the fuselage simulation is slightly altered by implementing a rotating domain with a refined mesh. The propeller geometry as modelled in N-XROTOR does not have a physical connection to the hub as it is modelled as a lifting line instead of a three dimensional geometry. To make the propeller geometry fit the aft fuselage, the CAD model of the propeller is slightly changed with respect to the geometry modelled in N-XROTOR. This modification is shown in figure 7.1 as a small added surface in the trailing edge region and a small removed surface from the leading edge region. Note that the spinner surface is modelled as a slip wall to allow for the finite velocity at the hub, which is in line with the analysis in N-XROTOR.

The standard  $\kappa - \omega$  SST turbulence model and the  $\kappa - \omega$  SST with a low Reynolds number correction are considered as turbulence models. The low  $Re$  version is also used because the Reynolds number close to the propeller hub is relatively low (of the order  $10^5$ ) and a larger influence of using this correction may be expected than in the N250 simulation. The boundary conditions are equal to the values listed in table 5.2 in Chapter 5.

The mesh close to the propeller surface is slightly altered with respect to the N250 propeller. The minimum element size on the trailing edge surface is different. This is taken as the smallest trailing edge thickness of the propeller blade. The leading edge and propeller surface refinements are chosen to obtain a reasonable mesh throughout the propeller surface. It is checked that the value of  $y^+$  is in an appropriate range over the blade (4 to 30). Initially an inflation layer consisting of eight layers was used in the CFD model but it lead to a boundary layer which was partially outside the refined inflation layer. However, this number is increased to twelve as the boundary layer in some regions on the propeller blade. The value of twelve was selected based on a two-dimensional airfoil CFD simulation at  $r/R = 0.52$  (further elaborated in section 7.2.2) in which the boundary layer is captured within the twelve cells. This simulation showed a smoother  $C_l - \alpha$  curve at high lift coefficients and lower drag coefficients using the increased inflation layer. The mesh settings are provided in table 7.1.

Table 7.1: Mesh of the installed non-uniform inflow propeller.

Region	Property	Value
Inflation layer	Number of layers	12
	Growth rate	1.20
	First layer thickness	$8.0 \cdot 10^{-5} [m]$
Rotating domain	Minimum element size	$7.5 \cdot 10^{-3} [m]$
Slipstream domain	Minimum element size	$7.5 \cdot 10^{-3} [m]$
Refinement domain	Minimum element size	$1.0 \cdot 10^{-1} [m]$
Outer domain	Minimum element size	$2.0 \cdot 10^{-1} [m]$
Leading edge	Minimum element size	$1.5 \cdot 10^{-4} [m]$
Trailing edge	Minimum element size	$4.0 \cdot 10^{-5} [m]$
Propeller surface	Minimum element size	$7.0 \cdot 10^{-4} [m]$

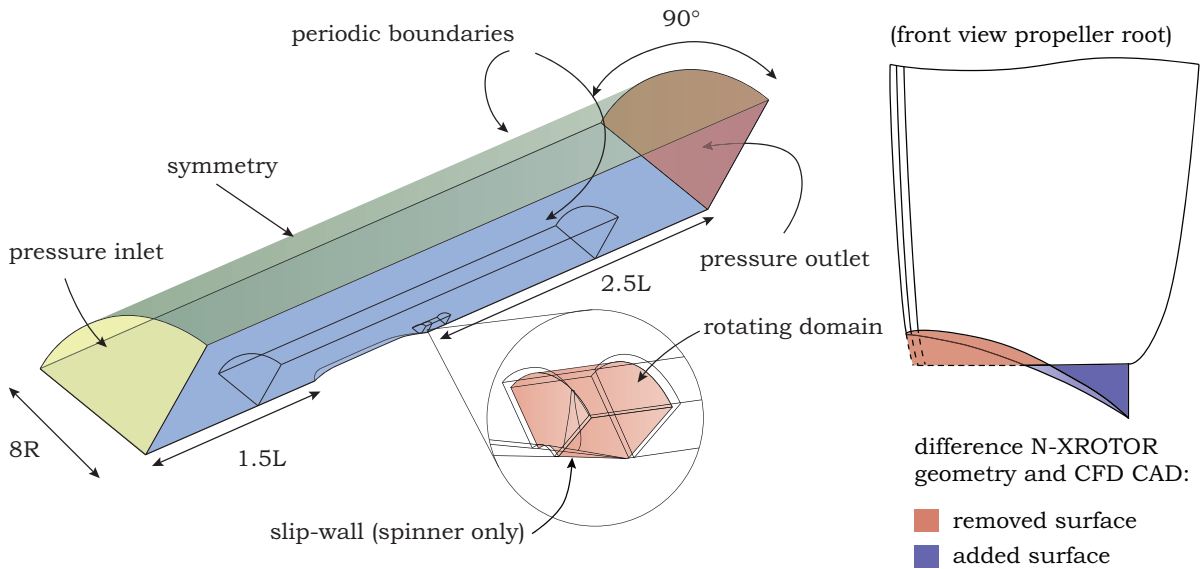


Figure 7.1: Left: the domain of the fuselage-propeller simulation with the boundary conditions indicated.  $R$  is referred to as the propeller radius and  $L$  as the fuselage length. Right: the modification of the geometry modelled in N-XRATOR to fit the aft fuselage shape in the CFD simulation.

## 7.2. COMPARISON WITH N-XRATOR

In this section the CFD results are compared with the results from N-XRATOR and deviations between the results are addressed. The comparison between the simulations indicates how well the simplified analysis tool can be used for design of the non-uniform inflow propeller.

Some radial distributions are shown in section 7.2.1. A number of possible causes for deviations are addressed in the subsequent sections. The effect of airfoil properties on the propeller performance is discussed in section 7.2.2. Radial flow on the blade is discussed in section 7.2.3. Special attention is paid on the flow in the outboard and root regions in sections 7.2.4 and 7.2.5 respectively.

### 7.2.1. RADIAL DISTRIBUTIONS

The performance quantities are compared in table 7.2. The table shows an over prediction of thrust coefficient of 4.15% by N-XRATOR and an over prediction in power of 4.71% using the standard  $\kappa - \omega$  SST model, which are in the same range as the deviations observed in the N250 simulation. The distributions of  $C_T$  and  $C_P$  are shown in figure 7.2 and a relatively good correspondence is observed between the two methods. The location of maximum thrust is well predicted by N-XRATOR. In the regions of higher thrust, the lifting line code slightly over predicts the thrust. Near the root and in the outboard radii there are some larger deviations. An interesting comparison is the distribution of thrust to power  $\frac{dT}{dQ\Omega}$ , shown in figure 7.2 (c). The trend of a higher thrust to power ratio in the low axial velocity region is followed except for the outer radii and root region. By looking at the performance quantities and radial distributions, the first observation is that there

Table 7.2: Comparison of  $C_T$  and  $C_P$  from CFD with the predictions of N-XROTOR

Method	$C_T$ [-]	Deviation	$C_P$ [-]	Deviation
CFD (MRF) with standard $\kappa - \omega$ SST	0.1277	-	0.1889	-
CFD (MRF) with $\kappa - \omega$ SST with low $Re$ correction	0.1278	+0.08%	0.1900	+0.06%
N-XROTOR using XFOIL airfoil data	0.1330	+4.15%	0.1979	+4.71%
N-XROTOR using CFD airfoil data	0.1287	+0.78%	0.1912	+1.22%

are no significant effects on the performance of the propeller which are not captured by N-XROTOR.

Some deviations between N-XROTOR and CFD may be visible in the section pressure distributions. In figures 7.3 (a) through (e) the pressure distribution computed with XFOIL and from the full blade CFD simulation at a number of radial sections is shown. The radial positions are indicated in figure 7.6 (a). The distribution by XFOIL is computed at the flow conditions and angle of attack calculated in N-XROTOR. The figures show that the distributions of the CFD model up and till  $r/R = 0.50$  have an off set relative to the XFOIL result. This is due to the induced pressure field by the fuselage. At  $r/R = 0.50, 0.67, 0.87$  there is no full pressure recovery on the suction side at the trailing edge, which indicates trailing edge stall. The reduced lift results in a reduced thrust with respect to the calculated thrust by N-XROTOR. This explains the relatively large deviation in thrust and torque distributions. Subsequent sections discuss the deviations in more detail, but phenomena that may cause a reduced suction include:

- The boundary layer thickness is expected to influence the pressure distribution. A faster growth of the boundary layer in CFD results in a lower curvature as experienced by the potential flow resulting in lower over speeds on the suction side.
- The lifting line theory neglects the variation of circulation in chordwise direction. For slender propeller blades up to moderate aspect ratios, the effect of this variation may be small. However, the  $\frac{c}{R}$  in the root region is relatively large in which a variation of  $\Gamma_B$  results in a change in  $\alpha$  [40, 48].
- The flow field upstream and downstream of the propeller may result in a different angle of attack due to differences in inflow velocity and induced velocity.
- The mesh in the vicinity of the propeller may not capture the flow accurately.

At  $r/R = 0.998$  the pressure distribution shows a rather unconventional shape. From the leading edge to approximately 10% of the chord there is a pressure region on the suction side and a suction region on the pressure side. The CFD results showed a stagnation point on the suction side of the airfoil. However, this still results in a thrust force as both the CFD and N-XROTOR results show a positive thrust over the complete blade. The most probable cause for this inefficient use of the tip airfoil is the constraint of one airfoil that is used for the complete blade. As discussed earlier, the optimisation routine tries to reduce the thrust towards the tip and with a cambered airfoil this requires a negative angle of attack which results in a stagnation point in the suction side of the airfoil. When a symmetrical airfoil is used over the complete blade or at the tip, it is expected that this behaviour is not present.

### 7.2.2. INFLUENCE OF AIRFOIL DATA AND TURBULENCE MODEL

XFOIL uses a different method in calculation the airfoil properties compared with the CFD calculations and a deviation between airfoil properties and hence an effect on the thrust and torque distributions may be expected. To quantify this effect, a comparison is made of the radial distributions of the designed blade using CFD data of two-dimensional airfoil sections and data from XFOIL. A CFD simulation is performed on the airfoil at  $r/R = 0.52$  using the same grid properties as in the propeller CFD model. This location is chosen as it represent approximately the location of the highest  $dT$  and an average to high  $C_l(r)$  value (figure 7.2 (f)) as estimated by N-XROTOR.

The flow quantities for the 2D section are approximated using the value of  $V_{eff}$  computed by N-XROTOR. Appendix D summarises the boundary conditions and the CFD setup of this simulation. As discussed in section 4.3.2, the  $\kappa - \omega$  SST model shows not very good performance for low Reynolds number flows and has a quite large effect on the development of the boundary layer in the leading edge region where the local  $Re_x$  is low. In the N250 propeller simulation the  $\kappa - \omega$  SST with a low Reynolds number correction does not show significant deviations in the thrust and torque distributions compared with the standard SST model.

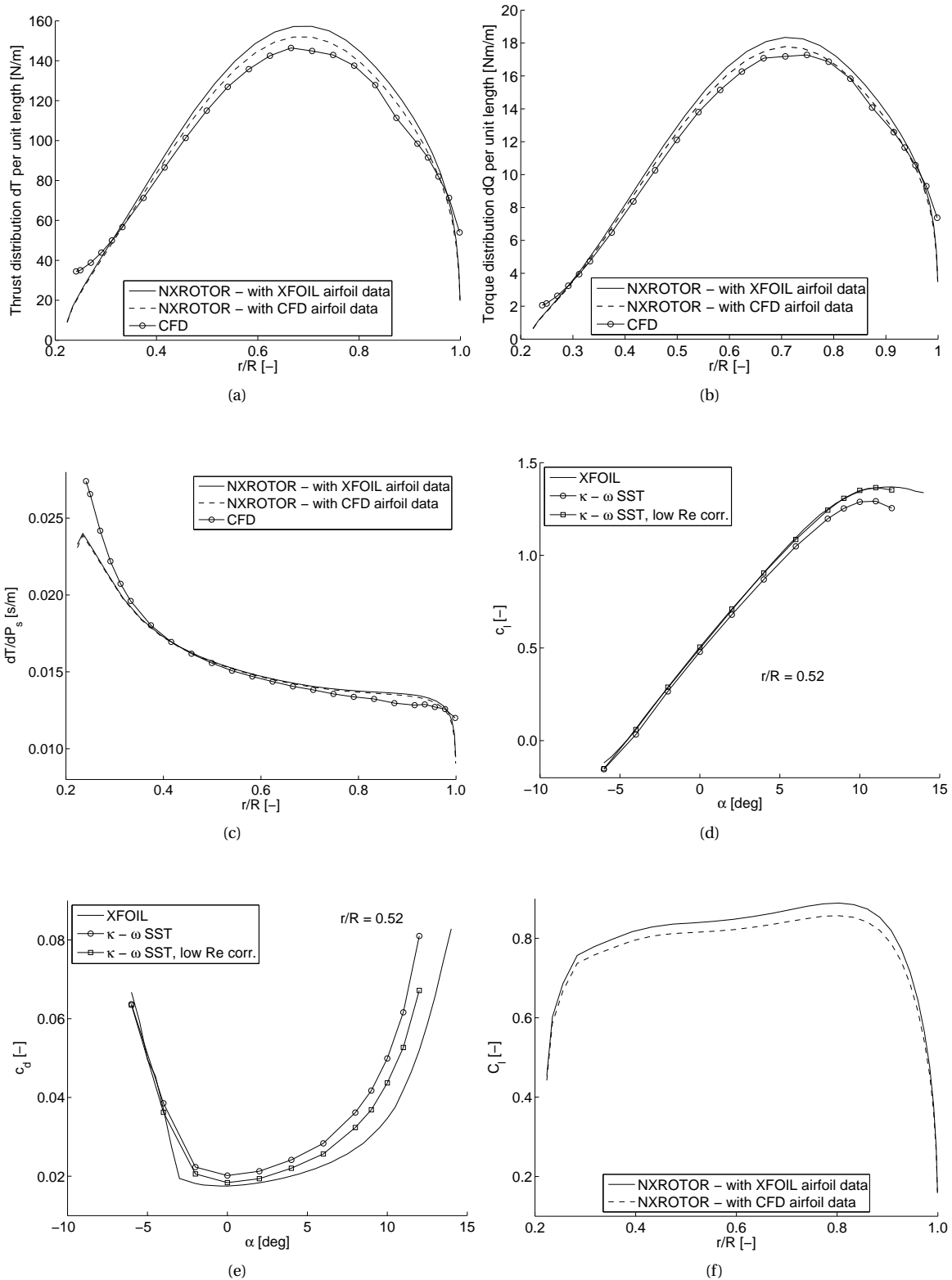


Figure 7.2: Comparison of distributions between N-XROTOR and the multiple reference frame CFD simulation. The results of N-XROTOR are computed using airfoil data calculated by XFOIL and the airfoil data as computed by CFD simulations on the 2D airfoil at  $r/R = 0.52$ . For the other airfoils the airfoil data is estimated using the XFOIL and CFD results.

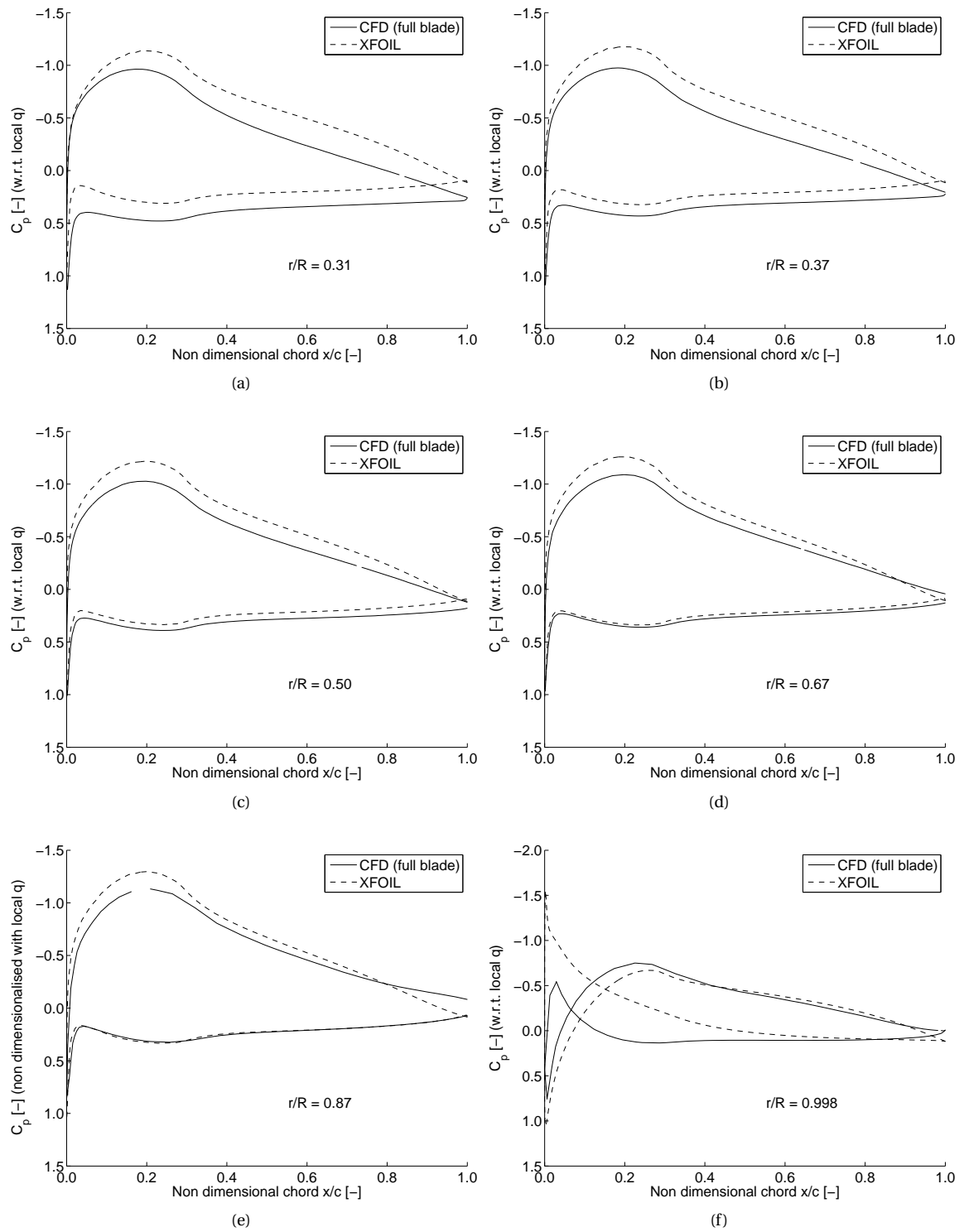


Figure 7.3: Comparison of pressure distributions at six radial positions as found by XFOIL and by CFD. The  $C_p$  is normalised w.r.t. the local dynamic pressure using the effective velocity predicted by N-XROTOR at that radial position.

However, the reduced inflow velocity and lower tip Mach number of the NUI propeller shows a distribution of lower Reynolds numbers than occur in the N250 simulation. Therefore also airfoil properties are computed with this turbulence model. The  $\alpha - C_l$  and  $\alpha - C_d$  curves computed with CFD and XFOIL are shown in figures 7.2 (d) and (e) respectively. A number of observations can be made:

- The lift curve slope of the standard SST model is slightly lower compared with XFOIL and there is an offset in the lift-curve. Both phenomena may be explained as a result of a thicker boundary layer. A thicker boundary layer on the upper surface results in a decambering of the airfoil which may explain the offset. When this decambering effect grows with angle of attack, the lift curve slope also reduces. In addition to the deviations of the linear lift curve,  $C_{l,max}$  occurs at a lower  $\alpha$  and the non-linear part of the curve starts several degrees earlier compared with XFOIL. Therefore earlier stall may occur in the CFD simulation of the propeller-fuselage configuration.
- Figure 7.2 (d) shows that the lift curve computed by XFOIL has significantly better agreement with the SST model with low Reynolds number correction. The  $C_l - \alpha$  curves from CFD and XFOIL almost exactly coincide over the complete range of  $\alpha$ . The laminar boundary layer region at the leading edge modelled in XFOIL is more in line with the boundary layer growth from the leading edge predicted by CFD.
- The shape of the  $C_d - \alpha$  curve is well captured by XFOIL, although a consistent under prediction of the  $C_d$  is present, likely due to a difference in skin friction as the deviation is almost an offset. The drag prediction of XFOIL corresponds better with the low Reynolds number model as the skin friction in the leading edge region is likely to be modelled more closely as XFOIL and the pressure drag is lower due to the less rapid growth of the boundary layer in that turbulence model.

To estimate the effect of using CFD data instead of XFOIL, the airfoil properties at all radial locations are corrected using the comparison of the properties at  $r/R = 0.52$ . It should be stressed that this will provide only an estimate as the deviations between XFOIL and CFD are likely not to be constant throughout the blade due to the range of Mach numbers, Reynolds numbers and mesh size. When these airfoil properties are used to estimate the performance, the deviation of N-XROTOR with respect to the CFD prediction is reduced to 0.94% in  $C_T$  and 0.84% in  $C_P$  as shown in table 7.2. The corresponding thrust and torque distributions are compared in figures 7.2 (a) and (b). A better agreement with the CFD results is shown in both the thrust and torque distributions. These results show a significant influence of the airfoil properties on the propeller performance. However, on the  $\frac{T}{D}$  ratio the difference between N-XROTOR and CFD is almost unaltered.

Figure 7.4 shows the thrust and torque distributions from the full blade simulation using the standard SST model and the SST model with low  $Re$  correction. A relatively small difference is observed between the two models. In the region of highest loading there is a small increase in both thrust and torque. It should be noted that the two models also yield different velocity inflow profiles for the propeller. This different velocity profile in the simulation with the low  $Re$  correction may influence the distribution as well.

From the previous paragraphs it may be noticed that although there is much better agreement with XFOIL using the low  $Re$  correction, there is limited impact on the thrust and torque distributions when the full blade simulation is computed with the low  $Re$  correction. Therefore it may be concluded that the majority of deviations between CFD and N-XROTOR are not the result of the difference in turbulence modelling and other phenomena dominate, which will be addressed in the following sections.

### 7.2.3. RADIAL FLOW

One of the neglected quantities in N-XROTOR is the radial flow. Two radial flow components may be distinguished; the external flow induced by a contraction of the aft-fuselage and an induced component by the propeller.

Radial flow is visualised in figure 7.6. The externally induced flow (as shown in figure 5.2 (d)) is strongest near the root which is up to 25% of the local axial velocity. The wall shear streamlines in figure 7.6 (a) show that near the leading edge in the root region there is a flow direction towards the root primarily due to the externally induced flow. At the trailing edge of the blade a much stronger radial flow can be observed in both radial directions. This flow behaviour may be explained in the same way as radial flow on the N250 propeller as a result from the trailing vorticity which induces a flow component in the radial region of the propeller. Over the majority of the trailing edge this results in a smooth bending of the wall shear streamlines in which the direction is dictated by the direction of the trailing vorticity. In the N250 simulation the direction of the streamlines on the pressure side is approximately opposite to the ones on the suction side. This behaviour is

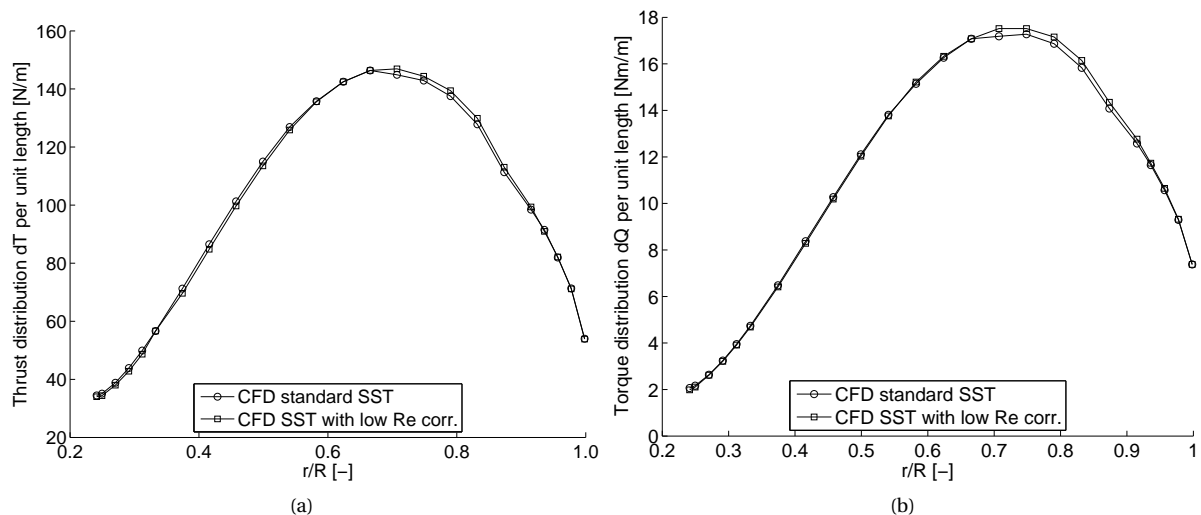


Figure 7.4: Effect of the low Reynolds number correction on the thrust and torque distributions in (a) and (b) respectively. The results are compared with the standard  $\kappa - \omega$  SST model.

only partly observed in figure 7.6 (a), possibly due to the external induced flow. However, when looking at a plane behind the propeller in figure 7.6(b) in which the radial flow distribution is shown, it is clear that the tendency of opposite radial flow is visible.

As discussed in 4.3.3, it is expected that the radial flow on the propeller influences the airfoil properties and the flow experienced by the airfoil. The airfoil properties are changed due to the influence on boundary layer growth in chord wise direction. It is expected that the magnitude of the local effective velocity is reduced due to the radial velocity component resulting in a lower dynamic pressure over the airfoil.

#### 7.2.4. STALL AT OUTBOARD SECTIONS

In the outer region of the blade  $\frac{dT}{dQ\Omega}$  is slightly lower in the CFD simulation of the full blade compared with N-XROTOR. Also the thrust in this region is suddenly lower compared with the other sections. The wall shear streamlines also show a quite abrupt change in direction in the region and the  $C_p$  plots show a pressure recovery downstream of the airfoil. These distributions indicate that is trailing edge stall which is not predicted in the N-XROTOR computation, neither in the results using XFOIL and CFD to calculate airfoil properties. Several differences exist between the three-dimensional blade simulation and the N-XROTOR computation. It may be argued that a larger angle of attack occurs in the CFD simulation of the full blade, leading to earlier stall than in the N-XROTOR simulation. However, the a comparison of the loading indicates that this is not the case as the loading of the CFD is primarily lower throughout the radii away from the root. In the full blade simulation a radial flow component is present (discussed in section 7.2.3). Though, three dimensional flow is shown be postpone stall (e.g. [57, 98]) due to the influence of the Coriolis force which is stabilising the boundary layer.

A possible cause is that the mesh influences the results. Compared with the chord length at  $r/R = 0.52$  the chord length at  $r/R = 0.85$  is almost 60% smaller. For the same surface mesh refinement, which is set in absolute dimensions, it means that airfoils with relatively small chords have a course mesh. The large deviation of the chord length over the radius is the case for the non-uniform inflow propeller. For uniform inflow propellers the chord distribution is more constant along the radius. To quantify this effect, CFD simulations on the airfoil at  $r/R = 0.85$  are compared with the airfoil data at  $r/R = 0.52$  using the same  $Re$  and  $M$  to only identify the effect of the mesh. Both airfoil sections have the same mesh refinement. The results are shown in figure 7.5 (a) and (b). The lift curve clearly shows that the courser mesh at the outboard section significantly influences the maximum lift coefficient, the angle of attack at which trailing edge stall starts and the camber of the airfoil due to a not sufficiently resolved boundary layer. It is therefore expected that the stall phenomena in the outboard regions is due to the course mesh in that region. In addition, the drag coefficient is has a higher value over the complete range of angles of attack. A variable mesh size depending on the local chord length would improve the results of the propeller-fuselage CFD simulation. It should be noted that the shown

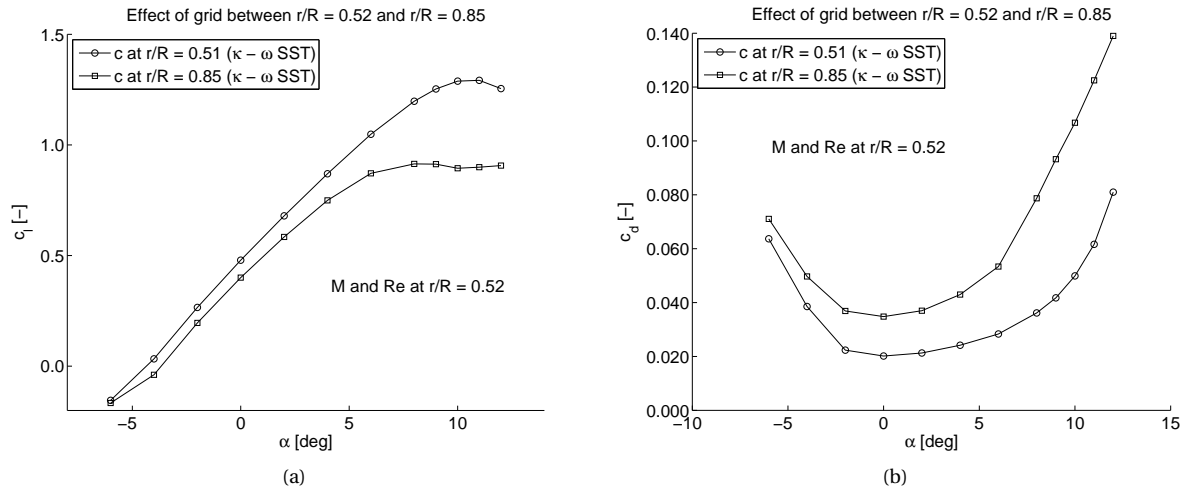


Figure 7.5: Effect of the mesh of the outboard region compared with the finer mesh in the inboard regions due to the constant mesh refinement along the blade with a varying chord distribution.

curves are therefore only an indication of the grid effect as each airfoil operates at different  $Re$  and  $M$ .

### 7.2.5. PERFORMANCE OF ROOT SECTIONS

Figures 7.2 (a) and (b) show a significant higher prediction in thrust and power in the root region by the CFD simulation compared with N-XROTOR. The underestimation of the hub effect by N-XROTOR has been indicated in section 4.3 for the N250 propeller. As the loading of the root region in the non-uniform inflow simulation is higher than in the N250 simulation, the influence of the hub can be expected to be larger. Not only the absolute force and torque distributions are higher in the hub region, also the ratio  $\frac{dT}{dP_s}$  is significantly higher than N-XROTOR predicts. This indicates that the finite loading at the hub is favourable for the propeller as the added thrust comes at a relatively low added torque. The higher thrust may be explained when looking at the flow in the root region.

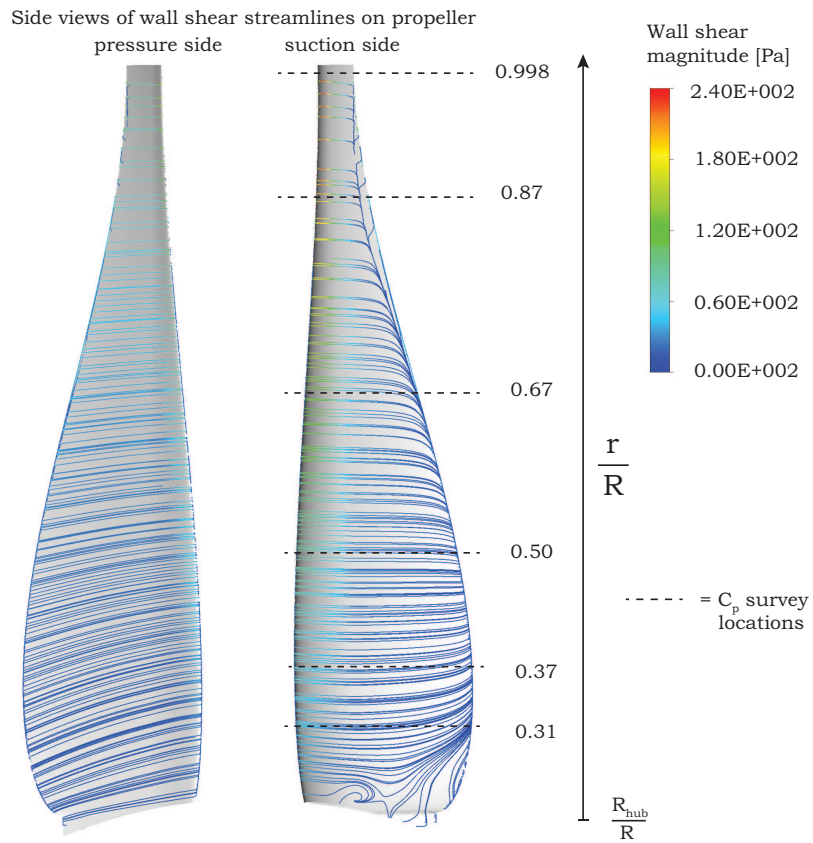
Figure 7.7 (a) shows the wall shear streamlines on the propeller in the root region as well as the velocity streamlines and pressure just above the spinner surface. It is shown that there is a three dimensional pocket of recirculating flow approximately at 40% of the chord. This pocket results in a relatively low pressure as indicated in the figure. The streamlines indicate a reattachment of the flow towards the trailing edge. In this particular setup there is a rapid deceleration of the velocity on the propeller surface at the junction with the spinner because the spinner is modelled as a slip wall while the propeller surface has a no slip condition. In combination with the adverse pressure gradient on the airfoil, this velocity gradient may result in separation. Figure 7.7 (b) shows the  $C_p$  distribution just above the spinner (adjusted for the operating pressure). The shape of the pressure side is approximately followed by XFOIL while the suction side is significantly under-predicted by XFOIL. The recirculating flow is expected to contribute to the low pressure as an analogy may be made with the additional 'vortex lift' on a swept wing or propeller which results in a leading edge vortex with a high dynamic pressure. The pressure distribution also indicates a higher angle of attack in the root section than predicted by N-XROTOR. N-XROTOR models the spinner with a constant radius. However in the CFD simulation the tapered spinner upstream of the propeller reduces the ability of the root sections to induce an axial velocity as the spinner effectively 'blocks' the flow to be induced by these sections. This yields an airfoil with a larger angle of attack than predicted in N-XROTOR and may contribute to the higher thrust observed in the CFD simulations.

Another effect on the root performance may be found in the pressure gradient induced by the fuselage. This induced pressure gradient acts as a force on the propeller which leads to an additional thrust and torque. This effect is schematically shown in figure 7.8. To estimate this effect on the propeller performance and the radial distributions, these components are assumed to act on a plate with a finite thickness with an angle equal to the blade angle  $\beta(r)$  such that the total force and power of the propeller due to the pressure gradient may be expressed as:

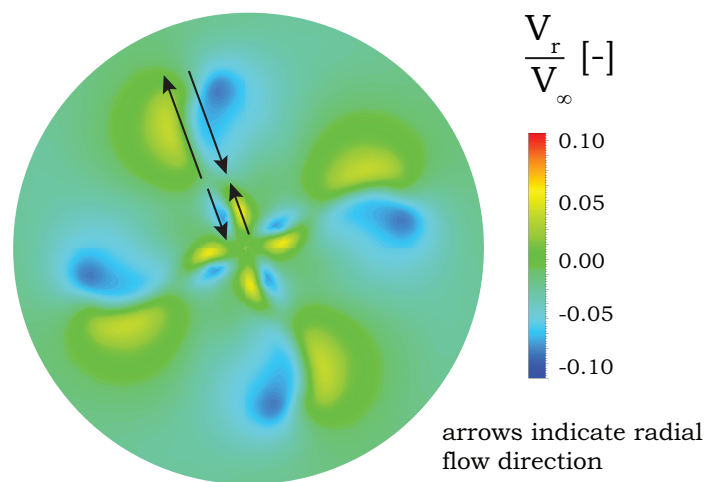
$$\Delta T_{\frac{dp}{dx}} = B \int_{R_{hub}}^R dp(r)c(r) \cos \beta(r) dr \quad (7.1)$$

$$\Delta P_{\frac{dp}{dx}} = B \int_{R_{hub}}^R \Omega dp(r)c(r) \sin \beta(r) r dr \quad (7.2)$$

in which  $dp(r)$  is the pressure difference between the two sides of the plate. The value of  $dp$  is approximated by taking the pressure difference between an upstream and downstream location of the isolated fuselage simulation and multiply it with the maximum thickness of the local airfoil. To indicate the importance of this effect on the total propeller thrust and torque, these terms are evaluated as  $\Delta T_{\frac{dp}{dx}} = 1.2 \cdot 10^{-4} T$  and  $\Delta P_{\frac{dp}{dx}} = 1.2 \cdot 10^{-4} P$ , which show that the pressure gradient does not significantly contribute to the (overall) propeller performance. Figure 7.8 also shows the radial distributions due to this pressure gradient. The distribution of  $dT_{\frac{dp}{dx}}$  to the propeller induced  $dT$  shows that there is a quite large variation along the radius with a relatively large contribution in the root region. However, that maximum value is only 0.12% of the value predicted by N-XROTOR and therefore the increased loading at the hub can not be explained by the externally induced pressure.



(a)



(b)

Figure 7.6: In (a) the propeller wall shear streamlines and the radial locations of which the pressure coefficient  $C_p$  is plotted in figures 7.3 (a) through (e). In (b) Radial flow in a plane just behind the spinner. The direction of the flow is indicated in arrows.

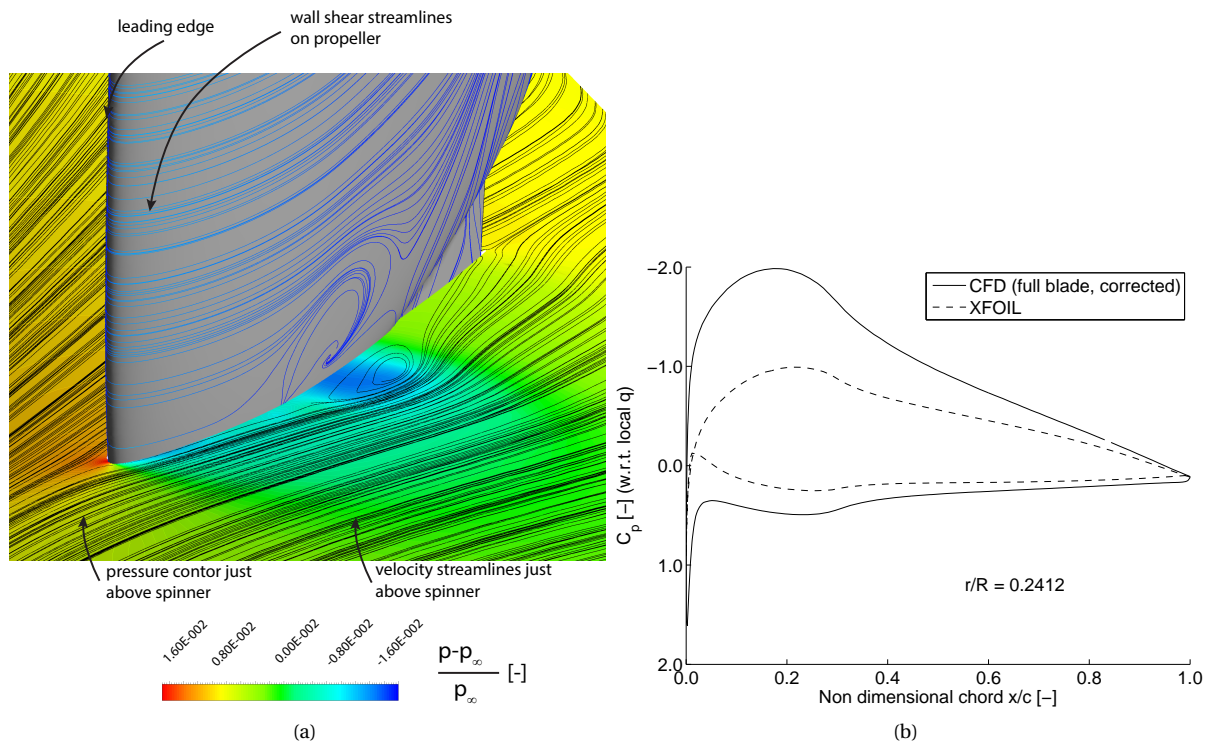


Figure 7.7: In (a) the wall shear streamlines on the propeller (side view) and a pressure contour with velocity streamlines just above the spinner. The corresponding  $C_p$  distribution is shown in (b), non-dimensionalised with the local dynamic pressure calculated by N-XROTOR and the curve is shifted with the operating pressure. Also the XFOIL result is shown, calculated with the  $\alpha$  determined by N-XROTOR.

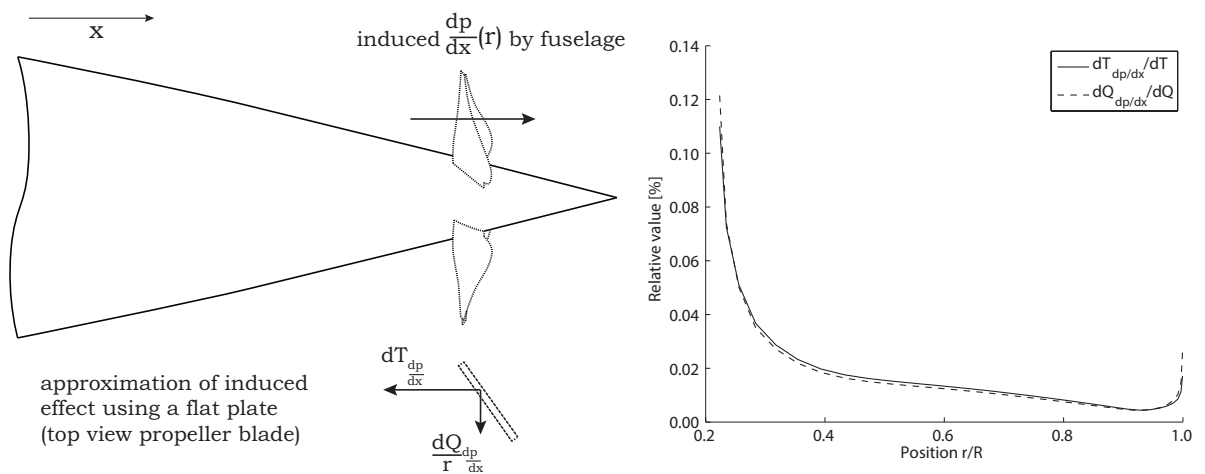


Figure 7.8: Effect of the induced pressure gradient in streamwise direction which adds to the thrust and torque of the propeller. For an order of magnitude analysis, the propeller is simplified as a flat plate with a finite thickness.

### 7.3. EFFECT PROPELLER ON AFT FUSELAGE

As mentioned in section 2.3, there are two main effects the propeller has on the flow field on the aft fuselage; (1) the strong hub vortex induces a lower pressure on the spinner resulting in pressure drag and (2) the pressure field of the propeller results in additional pressure and skin friction drag on the fuselage. The latter effect is approximated using an Actuator Disk (AD) model and is compared with the CFD results of the full simulation. The effect of the hub vortex is not predicted by the AD and gets therefore special attention in this section.

Table 7.3 shows the comparison of the fuselage drag in the isolated simulation, the simulation using the actuator disk and the multiple reference frame simulation. The drag forces on the spinner and on the fuselage minus spinner are listed as well. The spinner is shown to produce a net thrust force in all three cases due to the higher pressure which is built up behind the fuselage. As the spinner is modelled as a slip wall, in reality skin friction would decrease the net thrust force slightly. It is shown that the pressure jump by the AD especially changes the drag on the geometry without spinner, which is caused by the reduced upstream pressure. The drag on the spinner is almost not changed as the spinner experiences both a lower pressure on the surface upstream the AD and a higher pressure on the surface downstream the AD. In the full blade simulation the drag on the fuselage without spinner is slightly lower than predicted by the AD model. This is also predicted in section 5.4 as the largest pressure jump in the AD is at the root and the full blade simulation has the highest suction more towards the tip (shown in the thrust distribution in figure 7.2 (a)) and is further away from the upstream geometry. The full blade simulation shows a 1.87% higher (total) fuselage drag than predicted by the actuator disk simulation. It should be mentioned that this condition does not represent a force balance as the thrust by the propeller is 4.15% lower than predicted by N-XRATOR. The higher total drag is a mainly a result of a lower thrust force on the spinner. Compared with the AD simulation, there are a number of differences in the full blade simulation. The flow field in the full blade simulation is more concentrated than the flow field induced by the AD; the pressure field downstream of the propeller is not constant in circumferential direction. Also, there is no swirl velocity modelled by the AD simulation. This tangential velocity is only present behind the propeller (elaborated in section 2.2) and results in a lower pressure behind the propeller than predicted with the AD model and hence the thrust force on the spinner is also reduced.

Figure 7.9 (a) the circumferential average of the  $C_p$  from the full blade simulation is compared with the isolated fuselage and AD pressure coefficient. There are a number of observations. The  $C_p$  of the full simulation and AD compare quite well up and till  $\frac{x}{L_{fuselage}} = 0.95$  with a slightly higher pressure in the full blade simulation which explains the slightly lower fuselage drag. The  $C_p$  on the spinner is very different in both simulations. The circumferential averaged full blade  $C_p$  clearly does not have such a large jump in  $C_p$  as the AD. However, when considering different angles  $\phi$  in circumferential direction ( $\phi$  being defined in figure 7.9 (c)), one gets the distributions as shown in figure 7.9 (b). As may be expected with a finite number of blades, the circumferential variation of  $C_p$  is quite significant. The local pressure jump at the blade ( $\phi = 45^\circ$ ) is larger than predicted by the AD. The circumferential variation is especially visible near the blade and almost no deviations are shown for  $\frac{x}{L_{fuselage}} \leq 0.95$ .

One of the observations is that there is a quite sudden significant decrease of pressure on the aft portion of the spinner. This rise of  $-C_p$  may be a result from the hub vortex, which is schematically shown in figure 7.10 (a). The four blades each release a hub vortex due to the finite  $\Gamma_B$  which follows the contour of the spinner. Behind the spinner these vortices combine as one strong vortex trailing in axial direction along the axis of rotation. This vorticity induces a tangential velocity which leads to a lower pressure and results in a  $D_{vortex}$ . This effect is not included in the AD simulation. The hub vortex in the CFD simulation is shown in the top left figure of figure 7.10 (b) as a concentrated vorticity along the axis of rotation. In the top right figure it is shown that the majority of this vortex is axial vorticity. It should be mentioned that part of the concentrated vorticity comes from the hub vortex but also vorticity shed from propeller blade in the relatively lower radii

Table 7.3: Comparison of  $D_{fuselage}$  and  $D_{spinner}$  from a CFD simulation using an Actuator Disk (discussed in section 5.4) and the CFD simulation of the full blade. The drag of the isolated fuselage is provided as reference.

Method	Type of drag	$D_{spinner}[N]$	$D_{fuselage} - D_{spinner}[N]$
CFD (full simulation)	$D_{skin} + D_{pressure}$	-5.12	88.98
	$D_{skin}$	0.00	69.49
CFD (actuator disk)	$D_{skin} + D_{pressure}$	-7.44	89.64
	$D_{skin}$	0.00	67.83

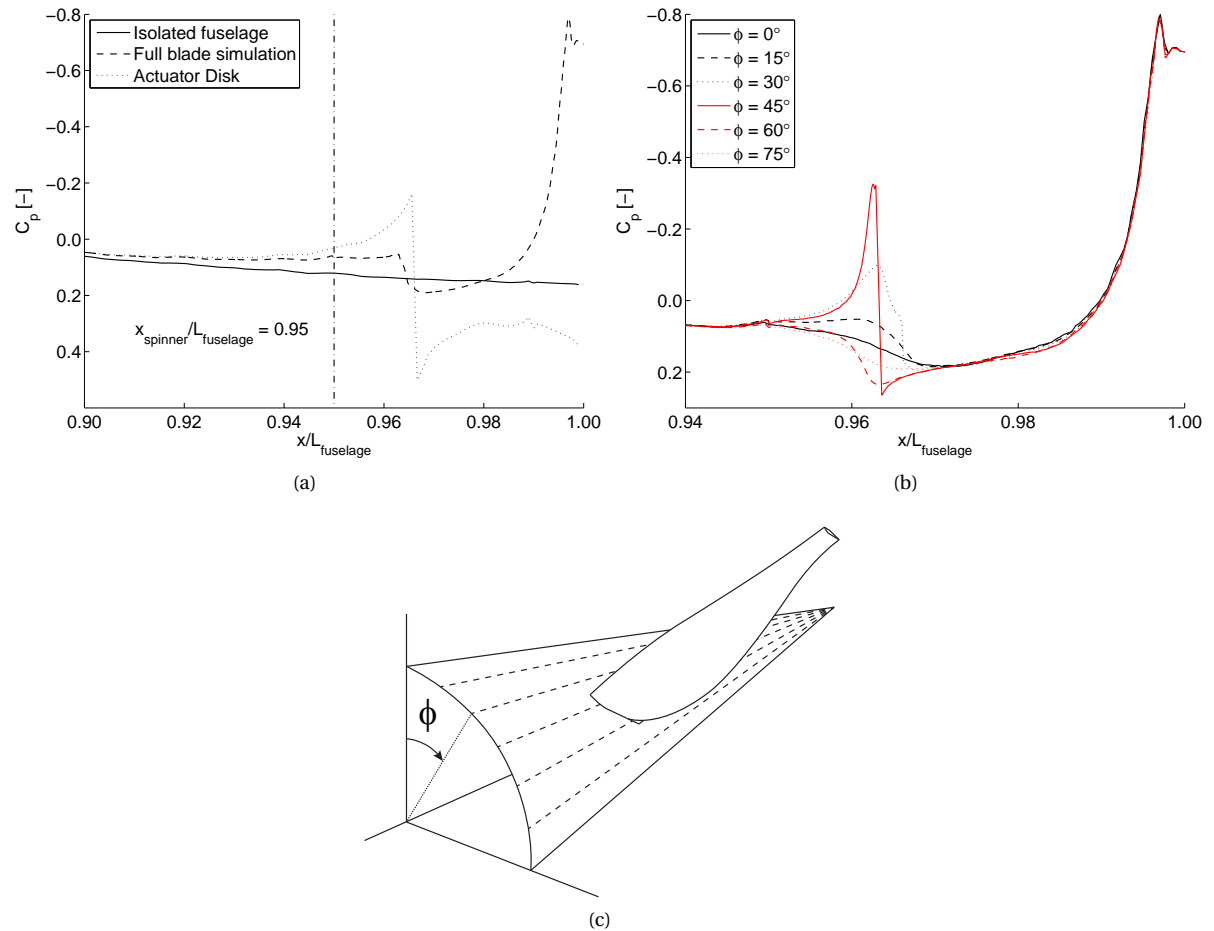


Figure 7.9: Comparison of  $C_p$  distributions along the aft part of the fuselage with the isolated fuselage simulation, the Actuator Disk and full blade simulation in (a). The location of the spinner is also indicated. In (b) the circumferential variation of  $C_p$  of the full blade simulation at several values of  $\phi$  where  $\phi$  is defined in (c).

which rolls up towards this hub vortex. This is the same phenomena as a trailing edge vorticity in the outer radii which rolls up into a strong tip vortex. The effect of this concentrated axial vorticity can be observed in the tangential velocity distribution and the pressure distribution in figure 7.10 (b). The magnitude of the tangential velocity shows a very high value at the spinner's axis of rotation. This results in a locally very low pressure which is the source of  $D_{vortex}$ . It may be observed in the vorticity plots that the periodic boundary conditions are visible. Vorticity is present at these boundary conditions which should not be the case. This behaviour is also present in the N250 simulation.

It is shown in figure 7.2 (c) that the propeller performance is enhanced by the high loading at the hub by the hub effect. However, it is questionable whether the finite circulation leads to a net benefit for the propeller as the additional interference drag of the hub vortex may cancel this benefit. In Wald [40] the additional drag is also recognised and it is recommended to have no circulation at the hub to prevent the  $D_{vortex}$ .

As noted in section 4.3.4, the sliding mesh approach results in a different and more concentrated upstream pressure than the multiple reference frame approach. Also the vorticity in slipstream is more averaged in circumferential direction and hence the hub vortex drag may be changed by applying the sliding mesh approach. This simulation is not performed for this thesis.

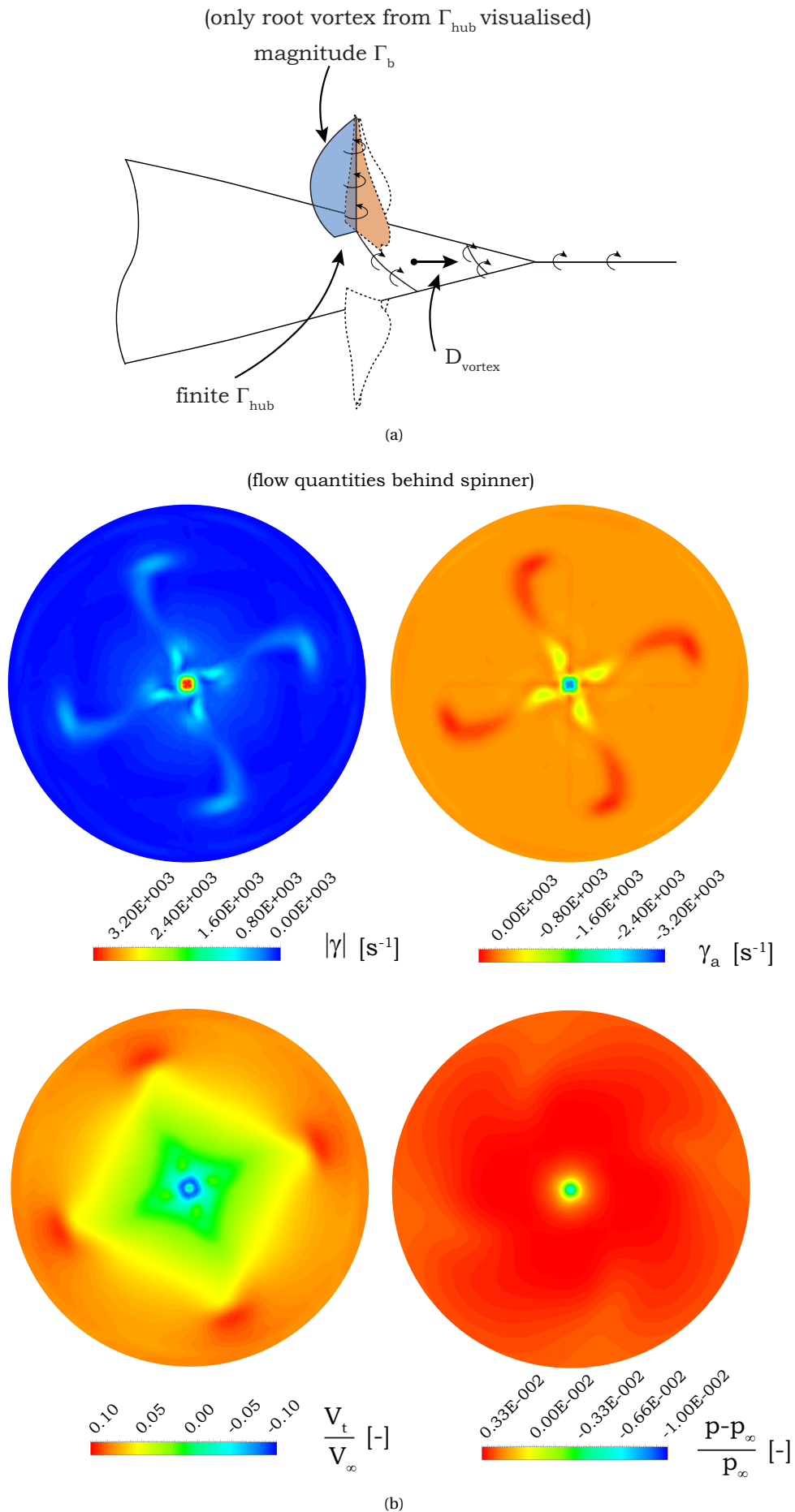


Figure 7.10: In (a) a schematic of the finite circulation at the hub which releases a vortex from each blade. Circulation indicated in blue and the corresponding blade in orange. In (b) some flow quantities to indicate the effect of the hub vortex in a plane just behind the spinner.

## 7.4. DESCRIPTION OF SLIPSTREAM

In this section the distributions of some flow quantities are compared between the isolated fuselage simulation and the full blade simulation. Both radial distributions at a plane behind the spinner and the development of averaged flow quantities in downstream direction are shown in sections 7.4.1 and 7.4.2 respectively.

### 7.4.1. RADIAL DISTRIBUTIONS WITH AND WITHOUT PROPELLER

To determine what the propeller does to the fluid properties, one can average the flow quantities at a plane in circumferential direction and compare this average to the flow state of the isolated fuselage simulation. Figure 7.11 (a) shows the considered survey plane just behind the spinner. The boundary layer follows the contour of the spinner and, if limited mixing takes place, should have the same thickness as at the location of the propeller. In figure 7.11(b) the total pressure contour of the isolated fuselage shows approximately the same boundary layer thickness as at the propeller plane as  $r/R = 1$  just behind the spinner corresponds roughly with the  $p_t/p_{t,0}$ . It is shown that the total pressure is increased by the propeller over the complete radius with the largest increase in the outer region, corresponding to the region of highest loading. In (c) there is a static pressure increase throughout the radius except for the inner radii, which is the result of the hub vortex. It is shown that the pressure field extends further than the propeller tip. The axial velocity (in (d)) shows a similar behaviour as the total pressure distribution, a maximum increase in magnitude in the outer radii. However the relative increase to the uninstalled velocity profile has its maximum at smaller radii. In the tip region one may observe a smaller axial velocity compared to the uninstalled condition. This is due to a contraction of the slipstream induced by the propeller which results in a radial velocity component and reduces the axial velocity component as indicated in figure 6.5. In (e) the effect of the hub vortex is observed in the tangential velocity distribution as a very large value along the axis of rotation as discussed in the previous section. Apart from this hub vortex, an increasing tangential velocity is observed towards the root in an almost linear distribution. The radial flow component in (f) indicates the contraction of the slipstream, which extends quite significantly beyond the radius of the propeller.

### 7.4.2. DEVELOPMENT OF FLOW QUANTITIES IN AXIAL DIRECTION

A method to analyse how the flow quantities develop downstream, the averaged quantities at circular planes at various axial directions may be computed. The quantities are averaged in circumferential and radial direction. Care should be taken when this method is applied, as the radius of each plane determines the averaged quantities of the flow; close to the propeller the averaged value of a very large plane is different than that of a much smaller plane. Of interest is the development of equal mass flux through a volume slightly larger than the slipstream. Therefore the edge of each plane is characterised by a common streamline; this ensures that the average is taken of the same flow at each plane. These planes are sketched in figure 7.12 (a). Figures 7.12 (b) through (f) provide averages of some flow quantities with the first plane having a radius of  $1.35R$ . Due to the discrete interpolation over the planes and the iterative approach to calculate the mass flow, the mass flow varies slightly from plane to plane, within 2% of the mass flow through the first plane.

The development of the pressure is shown in figure 7.12 (b). The isolated fuselage case shows an increasing pressure towards the propeller location and a decreasing pressure towards free stream conditions. When the propeller is installed, the typical averaged pressure of a propeller is shown as a jump in pressure. The jump is approximately equal in suction upstream and increased pressure downstream. The pressure development behind the propeller shows a very similar behaviour as the isolated case where the freestream value is reached after approximately six propeller radii downstream. It is noted that the pressure recovery is actually faster when the propeller is installed.

In figure 7.12 (c) the axial velocity is shown. The isolated fuselage shows an averaged axial velocity which very slowly increases behind the fuselage. In the installed case the velocity is increased smoothly through the propeller plane, which is also the case in momentum theory. The velocity is approaching the freestream velocity in a relatively short distance.

The tangential velocity (figure 7.12 (d)) shows no tangential velocity in the isolated case as expected. Upstream of the propeller the value of the averaged tangential velocity is zero, which is in line with vortex theory (section 2.2). The increase in  $V_{i,t}$  is a step and slowly decreases downstream. The contraction of the slipstream would lead to a slight increase in tangential velocity, however the viscous dissipation due to the velocity gradients near the slipstream yield a net decrease. Artificial dissipation in the CFD simulation results in an even faster decrease in tangential velocity. The contraction of the slipstream due to the propeller is shown in figure 7.12 (e) as a more negative radial velocity both upstream and downstream of the propeller.

The induced field of the propeller results in an increase in total pressure as shown in figure 7.12 (e). The isolated simulation shows variations of 1% in axial direction, also aft of the fuselage. This is likely due to the mass flow which is only approximately constant in axial direction and therefore the total pressure changing as well. Additionally, mixing of the flow outside the fuselage wake with the freestream flow occurs as very far from the fuselage the total pressure has its ambient value again. The total pressure experiences a step increase by the propeller, in line with the actuator disk theory and is very close to the total pressure in the freestream. It should be noted that the thrust of the propeller is 4.15 % lower than the fuselage drag (and the power is). In a thrust balancing situation, it can be expected that the total pressure in the slipstream is higher than predicted in 7.12 (e) due to the higher induced velocities in axial, tangential and radial directions.

In a plane parallel to the freestream flow at an azimuthal angle the axial velocity, total pressure and pressure are shown in figure 7.13 (a). Note that these quantities are not circumferential averaged and variations occur in circumferential direction. The axial velocity is shown as a quite increase at the outer radii of the propeller. Towards the axis of rotation, mixing of the flow occurs and the higher pressure is exchanged for increased axial velocity. The total pressure distribution shows that the thickness of the boundary layer from the fuselage is clearly reduced after the propeller. The dissipation of total pressure due to the hub vortex is clearly shown very close to the spinner. Downstream of the spinner the mixing is also shown in the total pressure. The pressure is shown to influence only a relatively small region, in upstream and downstream direction.

In 7.13 (b) the isosurface of axial vorticity is shown at a value of  $300 [s^{-1}]$ . It may be noticed that the root is dominating, both the vorticity shed from the inner radii as well as the axial vorticity from the hub vortex. The figure shows that the vorticity from the inner radii is merging with the hub vortex in a short distance. It is noted that the swirl angle in the root region is relatively large compared with the swirl angle of the tip, which is a result of the relatively low axial velocity.

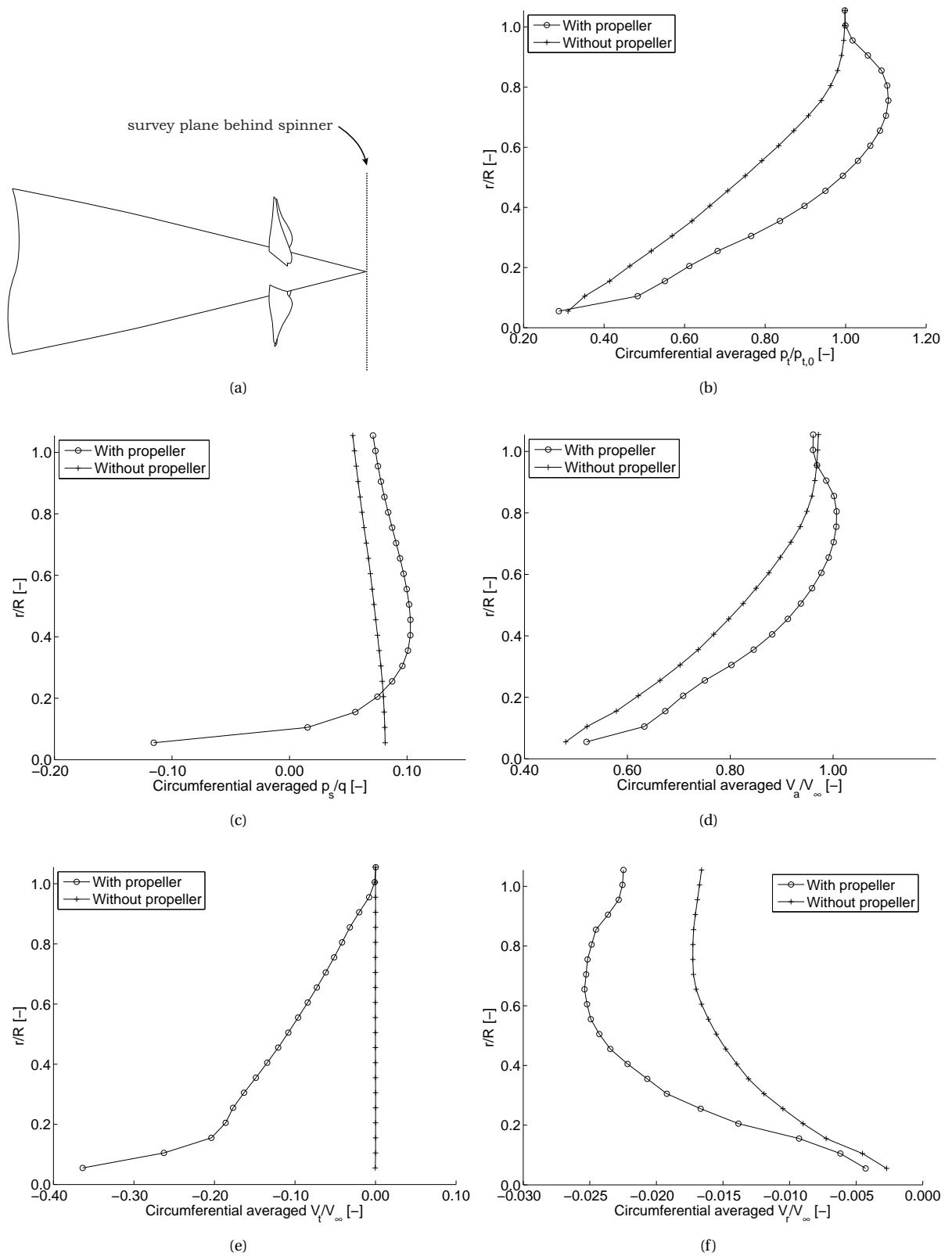


Figure 7.11: Circumferential averaged radial distributions with and without propeller. In (a) the location of the survey plane.

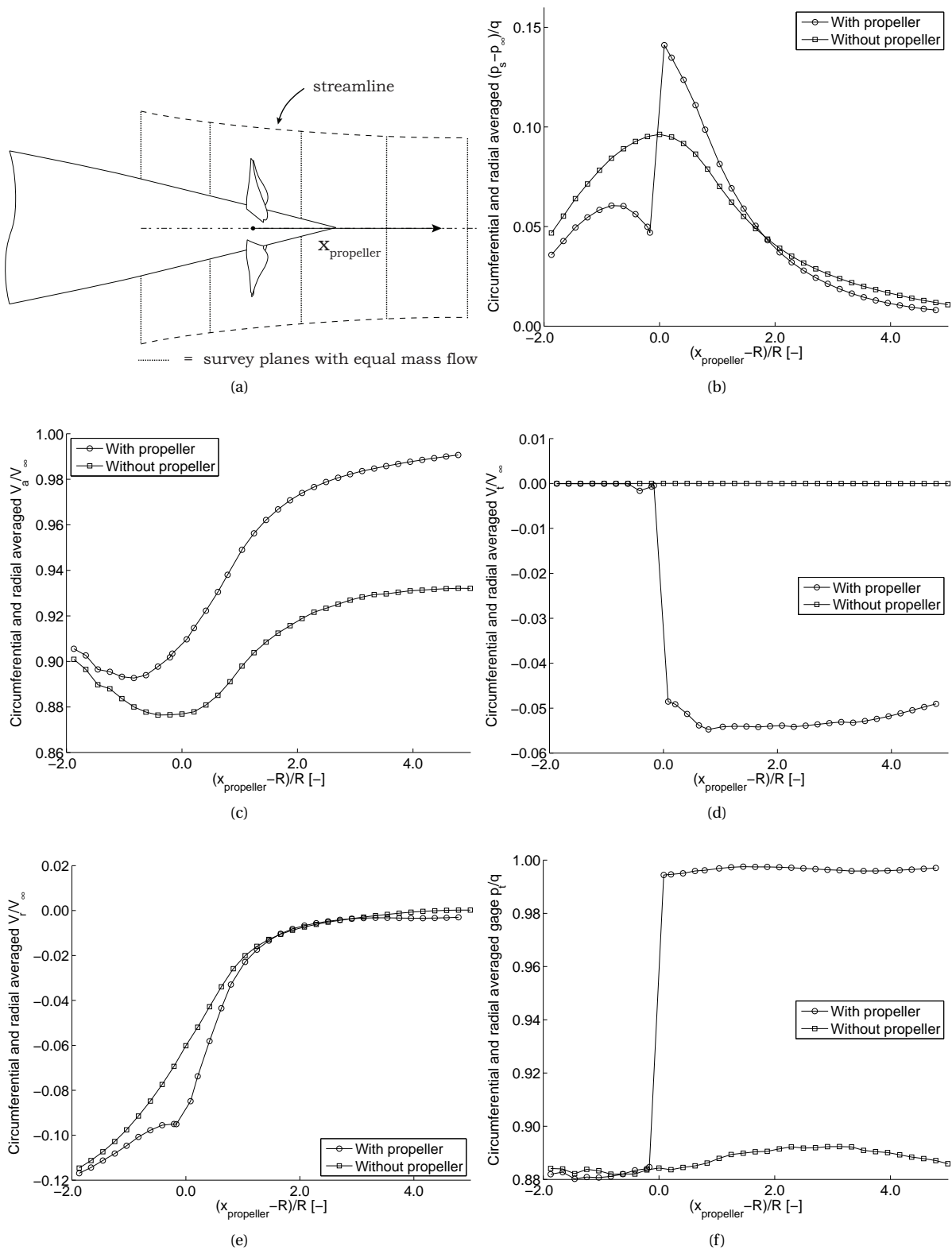
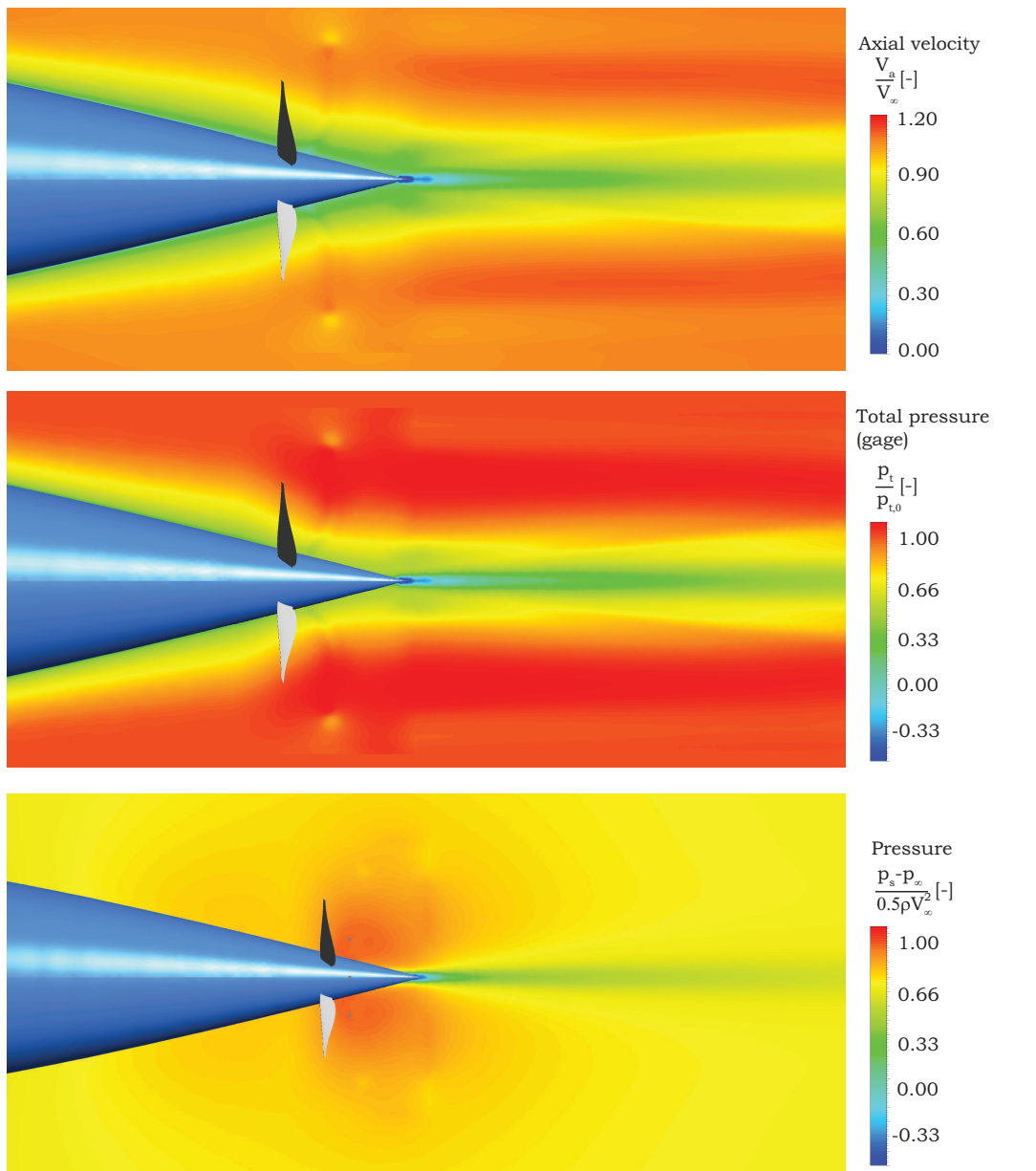
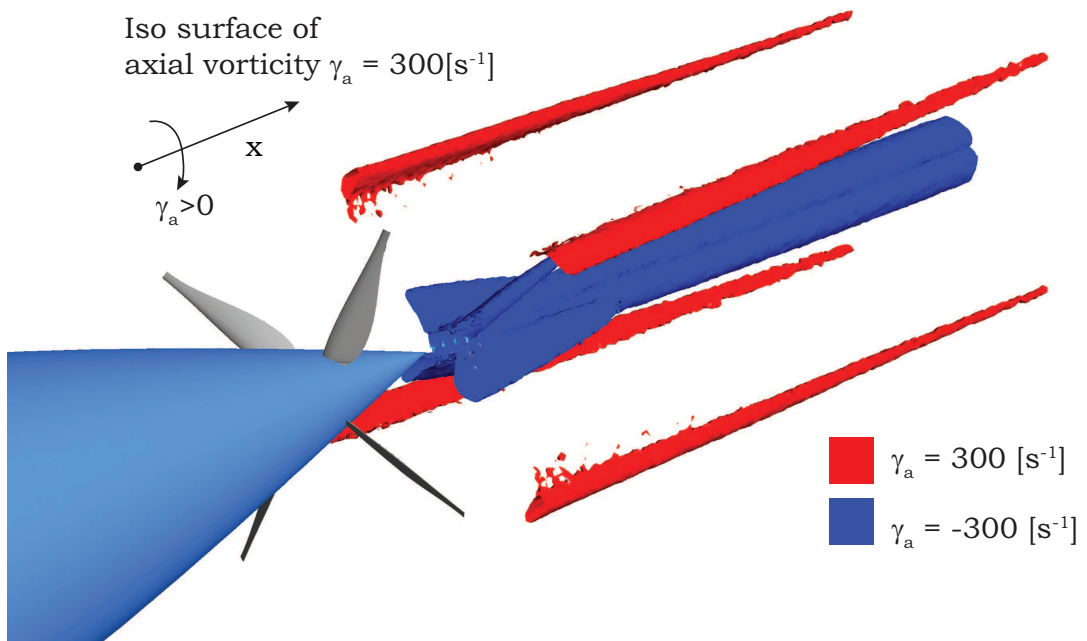


Figure 7.12: In (a) the schematic definition of the survey planes used for the slipstream analysis. These planes have equal mass flow and are bounded by the fuselage and streamlines. The radius of these planes is iteratively computed. In (b) through (f) the circumferential and radial averaged quantities with and without propeller in axial direction. The first plane has a radius of  $1.35R$ .



(a)



(b)

Figure 7.13: Some flow quantities in a plane parallel to the free stream flow (a). Isosurface of vorticity in (b).



# 8

## CONCLUSIONS AND RECOMMENDATIONS

In this chapter the conclusions and recommendations are summarised which are a result of the work performed in this thesis. Conclusions are provided in section 8.1 and recommendations for future work are given in section 8.2.

### 8.1. CONCLUSIONS

Previous research on the concept of 'Boundary Layer Ingestion' (BLI) includes experimental, numerical and analytical analysis. These studies are performed with theoretical propellers or propellers designed for uniform inflow and limited attention was paid to the propeller design of such configuration.

In an initial analysis of a uniform inflow propeller using the momentum and kinetic energy equations it is shown that a reduced axial inflow velocity results in a lower required power for a given thrust requirement. However, because the induced velocity increases with reducing axial velocity, the propulsive efficiency of this uniform inflow propulsor is decreased. The objective of this research is to obtain a better understanding of the power benefit of an installed pusher propeller operating in the boundary layer of an aft-fuselage and its interaction effects by developing a numerical method to design the aerodynamic shape of the propeller and validate the design by means of Computational Fluid Dynamics (CFD) simulations.

A propeller analysis tool named N-XROTOR is developed which uses the lifting line code XROTOR [1] for the propeller performance quantities and XFOIL [2] for the airfoil properties. The tool is capable of calculating propeller performance for both uniform or radially non-uniform inflow. No circumferential variations of the flow are taken into account. XFOIL is used to provide airfoil properties at several radial positions. The propeller analysis code is validated using experimental results of two uniform inflow propellers and CFD simulations. The performance quantities of the NACA III propeller [65] show a good prediction of the trend of the  $C_T - J$  and  $C_P - J$  curves but a constant over prediction of both quantities with respect to experimental data is observed. Good agreement is found in comparison with the experimental results of the N250 propeller [64]. Deviations include an over prediction of thrust at low advance ratios and a constant offset of the power coefficient. Deviations are explained by the absence of the spinner and radial flow on the propeller blade which are not taken into account, a finite chord length modelled as lifting line and the influence of modelled airfoil properties, which receives more attention in the non-uniform inflow simulation. A quite significant effect of the transition location is observed with a forward location of transition corresponding with a lower lift curve slope and a lower  $C_T$  and  $C_P$  over a range of advance ratios. A series of CFD simulations in ANSYS Fluent using a reduced wedge shaped domain of one blade of the N250 propeller is performed for several advance ratios. The standard  $\kappa - \omega$  SST is used as turbulence model and other computational settings are based on previous research. A grid refinement study is performed in which a balance is found between computational resources and convergence. Both a steady Multiple Reference Frame (MRF) method and a transient sliding mesh method are used for comparison purposes. Compared with the transient sliding mesh simulation, the MRF simulation results in a deviation of  $-0.85\%$  in thrust and a  $-1.00\%$  in torque at a moderate blade loading. This deviation is explained by the distribution of vorticity in the slipstream which is more concentrated from the propeller point of view in the MRF method resulting in a different induced velocity field compared with the sliding mesh results. Due to the significant computational resources required for the sliding mesh approach, the MRF approach is chosen for remaining simulations. The trends of N-XROTOR in terms of  $C_T - J$

and  $C_p - J$  compare well with the CFD simulation with a constant over prediction of the performance quantities by N-XROTOR. These over predictions are also noticeable in the radial distributions of thrust and torque with slight over predictions in the high loaded region on the blade. For a moderate advance ratio of  $J = 0.79$  the thrust and power are over predicted by 5.25% and 3.67% respectively. A comparison with the standard  $\kappa - \omega$  SST turbulence model and the SST model with low Reynolds number correction for a more accurate modelling of the flow near the leading edge shows that the low  $Re$  correction results in a minor increase in thrust and power of +0.08% and +0.06% respectively. The radial flow on the propeller blade is shown to be quite significant and varies along the blade. The distribution of bound circulation and the resulting trailing vorticity shows good agreement with the radial flow on the propeller blade, visualised using wall shear streamlines. The distribution of vorticity indicates to be the driving phenomenon of the radial flow near the propeller compared with other phenomena causing radial flow.

A design procedure is developed in which the propeller shape is optimised using shape functions to describe the pitch and chord distribution and a NACA four series airfoil is used to limit the number of design variables for a gradient based optimisation algorithm in Matlab environment. The interaction effects are assumed to be determined a-priori and a tapered aft fuselage and the pressure field induced by the fuselage are neglected. Input quantities for the design routine include an inflow field from CFD analysis, the design advance ratio and a thrust requirement. The design objective of all optimisations is minimum power. For the reference design case an axisymmetric body from ESDU is subject to CFD simulations with similar settings as the N250 simulation. The drag of the isolated body is determined which is used as thrust requirement for the uniform inflow design. For the installed non-uniform inflow design condition, an Actuator Disk (AD) model is used at the predefined location of the propeller with a pressure jump equal to the defect in total pressure upstream of the AD based on findings from previous research [3]. An 11% increase of drag is found for the equilibrium condition which is primarily due to increased pressure drag. Larger pressure jumps show only a marginal increase in drag. Due to limitations of the lifting line code and the AD model, a finite velocity at the aft fuselage is required which is realised using a slip wall boundary condition on the spinner surface.

The reference fuselage inflow field and thrust requirement are used to optimise a Uniform Inflow (UI) propeller with the thrust requirement equal to the drag of the isolated fuselage and the Non-Uniform Inflow (NUI) propeller with a thrust requirement including the approximated interference drag. The number of blades is set to four, an advance ratio of  $J = 1.50$  is chosen and in combination with a radius equal to 99% of the total gage pressure of the undisturbed air yields a tip Mach number of around 0.50. The optimisation results show that the NUI propeller requires 6.93% less power compared with the UI propeller even though the thrust is 11% higher. The thrust distribution of the NUI shows a significant increase in thrust in the low axial velocity region towards the root and the maximum thrust is shifted inboard. The torque distribution shows a similar behaviour although the increase in torque in the inner radii comes at a smaller increase. The ratio of thrust to torque  $\frac{dT}{dQ\Omega}$  along the propeller blade shows a constant distribution for the UI propeller, while the NUI propeller has a smooth increasing distribution towards the root. This distribution shows that thrust requires a relatively low power when the local axial velocity is relatively low. This is the main benefit of positioning a propeller in the boundary layer. The bound circulation distribution shows a shift towards the root compared with the distribution of the uniform inflow propeller which is the result of the optimised propeller shape which benefits from the favourable thrust to power ratio in the inner radii. The NUI propeller has a significant increased chord compared with the optimal UI and also a higher lift coefficient distribution. The blade pitch distribution is relatively constant for the NUI propeller to achieve moderate angles of attacks. In the tip region of the NUI propeller, the  $\frac{dT}{dQ\Omega}$  is higher than the distribution of UI as the axial velocity at the edge of the boundary layer is lower than free stream values because of the induced velocity of the fuselage. In addition to the benefit of the low axial velocity, the non-uniformity of the inflow is expected to be beneficial. The non-uniform inflow affects the outflow flow angles which dictate the direction of trailing vorticity and the axial vorticity results in tangential induced velocities and the tangential vorticity results in axial induced flow. The non-uniform inflow results in outflow angles at the NUI propeller blade which are smaller compared with the UI propeller outflow angles. Therefore the ratio of axial vorticity to tangential vorticity is lower and more constant for the NUI. The local efficiency defined as  $\eta_{local} = \frac{dT V_a}{dQ\Omega}$  with  $V_a$  as the local inflow velocity. Optimal UI propellers have a constant efficiency distribution, but the NUI propeller shows a decreasing trend towards the root which is also found in literature. This is analogous to the momentum analysis for uniform inflow which shows a reduced efficiency at lower axial velocities. The trend of lower  $\eta_{local}$  is also found when an optimisation for minimum power is performed using a radially varying actuator disk with the same inflow and thrust requirement as for the full blade propeller.

Compared with the UI propeller, the NUI propeller has a lower slope of the  $C_T - J$  curve. A possible

cause for this behaviour this is that due the compressibility effect which is on average more dominant in the uniform inflow case due to the higher local Mach numbers. This results in a higher lift curve slope than the non-uniform inflow propeller.

Additional optimisations are performed to quantify the effect of the number of blades, radius and advance ratio which are all set a priori in the reference optimisations. The effect of the number of blades on the minimum power is similar for NUI and UI propellers with two and six blades resulting in a higher minimum power compared with four blades. A lower number of blades results in higher induced losses while a larger number of blades results in more profile drag losses. An increased rotational speed (or decreased advance ratio) shows to be beneficial for the minimum required power due to lower induced losses which is in general also the case for UI propellers. Both a 10% larger and smaller radius shows to be beneficial for the NUI propeller. The smaller radius result on average in a lower average axial velocity and a higher radius is expected to be similar to the UI propeller which requires smaller induced velocities for the same thrust requirement. In addition it is shown that when a higher thrust requirement is set, individually designed NUI propellers for each thrust requirement show a constant power benefit compared with the optimised UI propellers.

The optimised NUI propeller in the installed configuration is simulated using CFD with the Multiple Reference Frame method with a reduced wedge shaped domain. The operating conditions correspond to the design condition. N-XROTOR over predicts the thrust and power by 4.15% and 4.71% respectively compared with the CFD simulation with the standard  $\kappa - \omega$  SST turbulence model, which are deviations of the same order as the N250 simulation. The  $\frac{dT}{dQ\Omega}$  distribution shows good correspondence, although in the outer region ( $\frac{r}{R} = 0.7 \dots 0.95$ ) the  $\frac{dT}{dQ\Omega}$  is over predicted by N-XROTOR and in the root region this ratio is under predicted by N-XROTOR. Several causes are found for these deviations.

In the root region the CFD simulation shows a quite significant over prediction of thrust and it is considered that this is caused by two effects. The junction between the slip wall boundary condition on the spinner and the no slip wall propeller surface result in a significant velocity and pressure gradient. A separated flow region is present at approximately half the chord which reattaches downstream of the airfoil. This region results in a locally low pressure and thereby an additional thrust force. Also the tapered spinner constrains the root region to induce an axial velocity which results in a higher angle of attack in the CFD simulation compared with N-XROTOR, also shown in the  $C_p$  distribution of the root airfoil compared with XFOIL results. The fuselage induced streamwise pressure gradient varies in radial direction at the plane of the propeller and leads to an additional force on the propeller. However it is shown that the maximum deviation of this pressure gradient is 0.12% of the local thrust and the integrated value has shown to be in the order of 0.01% of the total thrust and torque.

The  $C_p$  distributions at several radial locations compared with the XFOIL results indicate trailing edge stall at the outboard radii. Several causes are identified. A two-dimensional CFD simulation is performed on the airfoil section at the location of highest loading with the same mesh as the full blade simulation. Compared with the predicted properties from XFOIL, a reduced lift curve slope, a lower maximum lift coefficient and an offset is obtained indicating a decambering effect of the airfoil in the CFD simulation. When these airfoil properties are used by N-XROTOR instead of the XFOIL computation, the deviation between N-XROTOR and CFD is reduced to +0.78% on the thrust and +1.22% on the power. However, no trailing edge stall is observed in N-XROTOR which indicates another effect causing the trailing edge stall. A similar two dimensional airfoil simulation using the  $\kappa - \omega$  SST model with low Reynolds number correction shows almost exact agreement with XFOIL. This indicates the importance of accurately modelling of the boundary layer in the low Reynolds number regions near the leading edge. A full blade CFD simulation with this turbulence model shows minor deviations in the thrust and torque distributions and is therefore not the main cause of deviation. A two-dimensional simulation with constant Mach and Reynolds number on a section at  $\frac{r}{R} = 0.52$  and  $\frac{r}{R} = 0.85$  with constant mesh refinement shows a significant influence of the mesh on the airfoil properties. A much lower maximum lift coefficient, a reduced lift curve slope, an off set in lift curve slope and a higher drag coefficient over a range of angle of attacks is the result. The coarse mesh in the outer region is found to be the driving factor for the reduced loading in the CFD results compared with N-XROTOR.

The remaining deviations between N-XROTOR with approximated CFD airfoil properties are expected to originate from the radial flow on the blade which is not modelled and the finite chord which is modelled as a lifting line in N-XROTOR. The radial flow is visualised with wall shear streamlines on the propeller surface. A similar pattern is recognised as the N250 simulation with the radial flow being proportional to the magnitude and direction of trailing vorticity. In a plane behind the spinner the radial flow is clearly observable with the radial flow direction being opposite on the pressure side. Both the externally induced radial flow by the tapered aft fuselage and the self induced radial flow are expected to result in a decambering of the airfoil due

to the influence on boundary layer growth as well as a reduced chord wise velocity resulting in a locally lower dynamic pressure experienced by the airfoil contour. The finite chord results in a variation of circulation in chordwise direction which results in generally a lower effective angle of attack and therefore a reduced loading.

The interference effects of the propeller onto the fuselage are compared with the AD approximation. The circumferential average  $C_p$  upstream of the propeller on the fuselage geometry excluding spinner shows reasonable agreement and an over prediction of 0.74% of the drag by the AD model is observed. This indicates that for a first order estimate of upstream effects the AD model performs reasonably well. Close to the propeller the over prediction of the  $C_p$  by the AD model is increased. This is because the AD has the largest pressure jump at the root while the maximum pressure jump of the full blade simulation is further away from the spinner. Downstream of the full blade simulation the pressure is rapidly decreased to a low finite value at the aft end of the spinner. This is the result of the finite bound circulation at the propeller root which releases a strong trailing vortex from each blade. These vortices are following the contour of the spinner and combine into a strong vortex. This is shown in the vorticity magnitude contour as concentrated vorticity which is mainly in axial direction. This vortex induces a strong tangential velocity resulting in a low pressure acting on the spinner. The net thrust force on the spinner is significantly reduced compared with the AD simulation resulting in an overall drag increase of the fuselage.

A slipstream analysis is performed of circumferentially averaged flow quantities in radial direction at a plane behind the propeller and the axial development of several averaged flow quantities is shown. At a plane just behind the spinner the largest axially induced velocity is shown to be at the location of highest loading. A similar behaviour is shown for the total pressure distribution which varies in radial direction. The total pressure has larger values than free stream values in the outer radii. The tangential induced velocity is shown to be highest in the root region. The strong vortex at the axis of rotation is shown as a large tangential velocity. To analyse how the flow quantities develop downstream, the flow properties at several planes axial locations are extracted and averaged in radial and circumferential direction in which each plane has a approximately the same mass flow. A jump in pressure is shown at the location of the propeller with a symmetrical distribution. The axial velocity is shown to be increased smoothly and at about five propeller radii downstream has almost reached freestream values. The tangential velocity is shown as a jump, which is expected from vortex theory. The total pressure is shown as a step increase and behind the propeller is close to the freestream total gage pressure.

## 8.2. RECOMMENDATIONS FOR FURTHER RESEARCH

Several recommendations for future work are formulated in this section. It is expected that these recommendations improve the propeller design, improve the design procedure and increase the power benefit of the non-uniform inflow propeller. Some recommendations for the design and analysis tool are proposed:

- Improvements are expected when more attention is paid to airfoil design. The current setup allows for thickness and camber optimisations of NACA four series airfoils. When more airfoil families are considered or the complete airfoil shape is optimised, better airfoil properties may be the result. It is recommended that multiple airfoils are optimised along the radius as it is expected that due to the varying lift coefficient and Reynolds number the optimal airfoil changes along the propeller radius.
- To reduce the vortex drag arising from the vortex shed from a finite bound circulation at the hub, a boundary condition may be imposed to have no circulation at the propeller hub. However, this may result in a decreased propeller performance and therefore a method to estimate the vortex drag should be implemented in the optimisation routine to find a balance between propeller performance and interference drag.
- The finite loading at the root as a result of the limited capability to induce axial velocity from the tapered aft fuselage shape is recommended to be included in the analysis tool. This means that the actual effective angle of attack should be increased due to this blockage effect.
- As the interference drag is found to be significant for the reference case, the shape of the aft fuselage is suggested to be optimised. The shape upstream of the propeller may be optimised using an actuator disk representation.

For the CFD analysis of the non-uniform inflow propeller the following is suggested:

- A better representation of the interference effect may be found when the actuator disk has a finite swirl velocity in addition to the pressure jump. The reduced thrust force on the spinner from this lower pressure downstream is included in the total fuselage drag computation. A linear and decreasing tangential velocity profile from root to tip is suggested.
- It is recommended that the mesh refinement on the propeller blade and consequently the element size near the blade is not a constant value along the blade but rather changes with changing chord. The non-uniform inflow propeller has a highly changing chord distribution and a constant minimum element size leads to a too coarse mesh at the outboard sections with a low  $\frac{c}{R}$  value.
- A sliding mesh simulation of the installed configuration is suggested as the upstream effect of the pressure on the boundary layer is expected to be different from the multiple reference frame simulation.
- The junction of the propeller blade with the spinner which has a slip wall boundary condition may be improved by the use of fillets to reduce the pressure and velocity gradients at the junction.



# A

## GEOMETRY DESCRIPTION OF TWO PROPELLERS USED IN VALIDATION OF N-XROTOR

The following sections describe the propeller geometry of two propellers of which the performance curves are compared with the output of N-XROTOR.

### A.1. N250 PROPELLER

Quantity	Value
$B$	6 [-]
$R$	0.2033 [m]
$R_{hub}$	0.0468 [m]
$\Omega$	$1.0472e+03$ [rad/s]

	$r/R = 0.2300$	0.4050	0.5100	0.6150	0.7200	0.7900	0.8600	0.9300	0.9650	1.0000
$c/R$ [-]	0.1556	0.1456	0.1468	0.1515	0.1534	0.1515	0.1380	0.1094	0.0912	0.0681
$\beta$ [°] ( $\beta_{0.75} = 25^\circ$ )	47.89	38.87	33.73	28.75	24.27	22.09	20.20	18.47	17.63	17.00

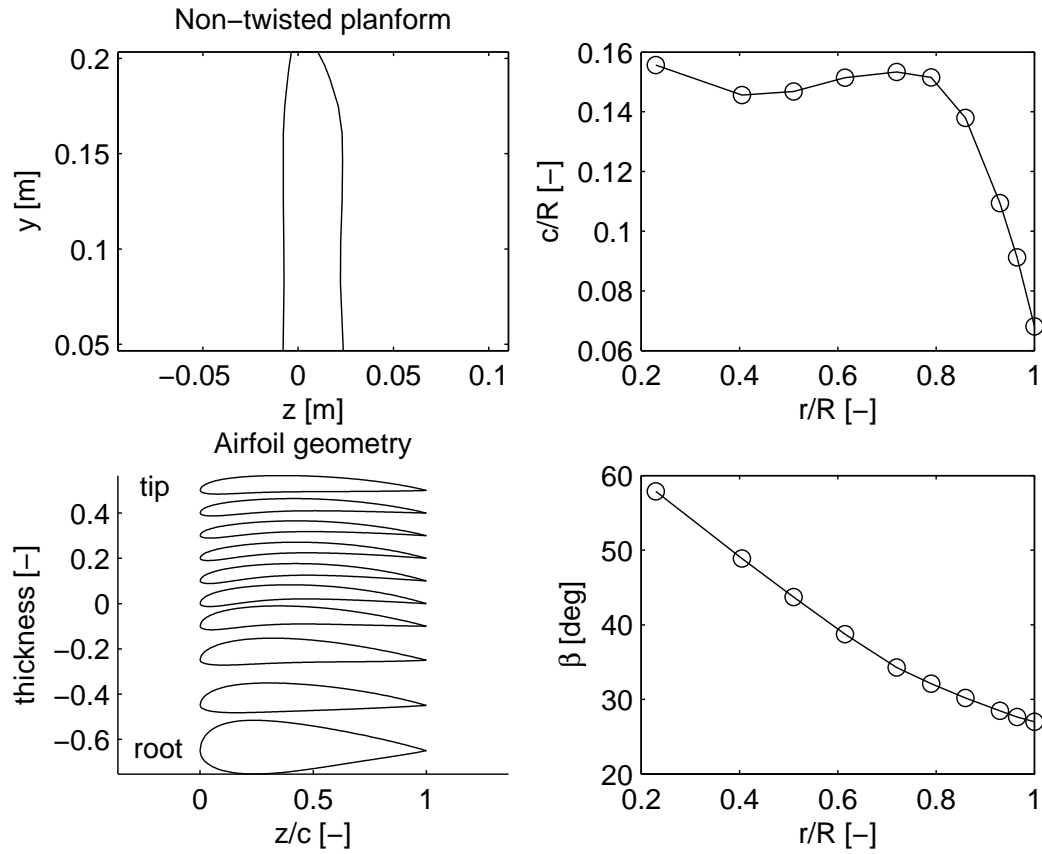
A graphical representation of the N250 propeller is shown in figure A.1 (a).

### A.2. NACA-3 PROPELLER

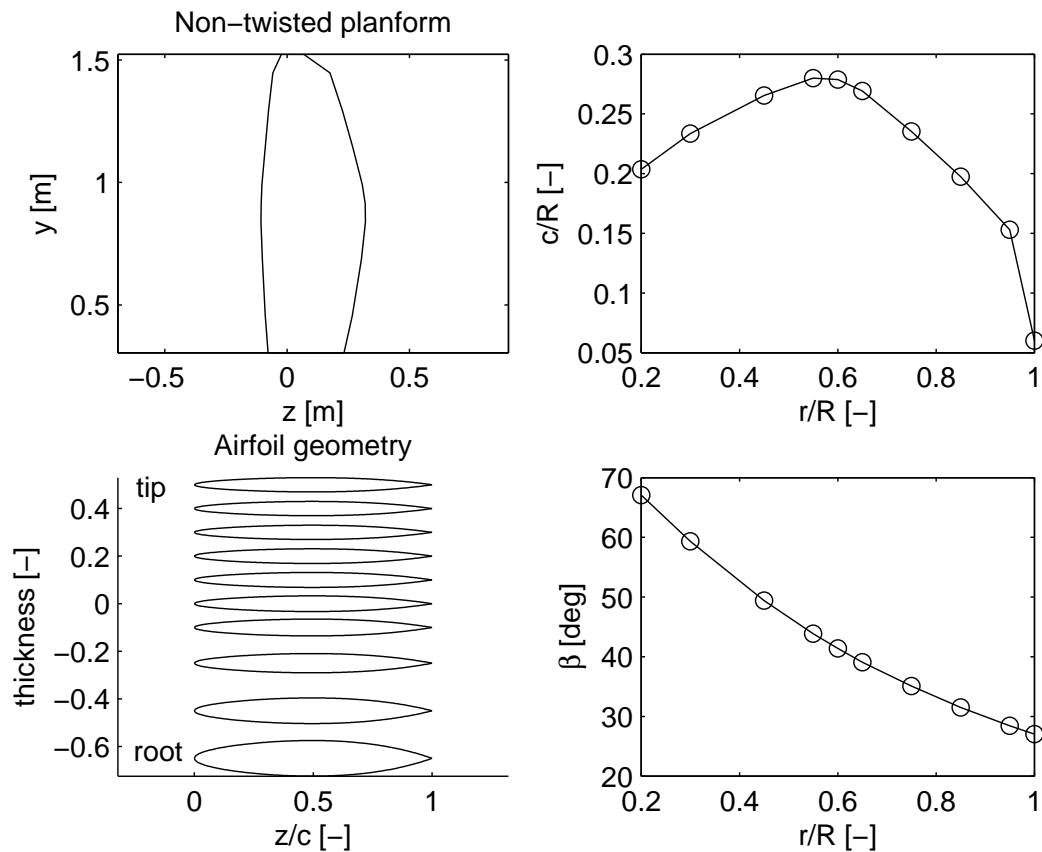
Quantity	Value
$B$	2 [-]
$R$	1.524 [m]
$R_{hub}$	0.3048 [m]
$\Omega$	141.37 [rad/s]

	$r/R = 0.2000$	0.300	0.4500	0.5500	0.6000	0.6500	0.7500	0.8500	0.9500	1.0000
$c/R$ [-]	0.2037	0.2335	0.2654	0.2799	0.2788	0.2691	0.2353	0.2353	0.1975	0.0600
$\beta$ [°] ( $\beta_{0.75} = 35^\circ$ )	67.06	59.34	49.388	43.85	41.38	39.08	35.10	31.49	28.43	27.04

A graphical representation of the NACA-III propeller is shown in figure A.1 (b).



(a)



(b)

Figure A.1: Graphical representation of the (a) N250 propeller ( $\beta_{0.7R} = 35^\circ$ ) and the (b) NACA-III propeller ( $\beta_{0.75R} = 35^\circ$ ) used for the validation of the N-XROTOR isolated propeller analysis tool for uniform inflow. The airfoil geometries correspond to the radial positions indicated with a circle on the  $c/R$  and  $\beta(r)$  distributions.

# B

## ADDITIONAL RESULTS OF THE N250 PROPELLER

### B.1. MESH REFINEMENT STUDY IN N-XROTOR

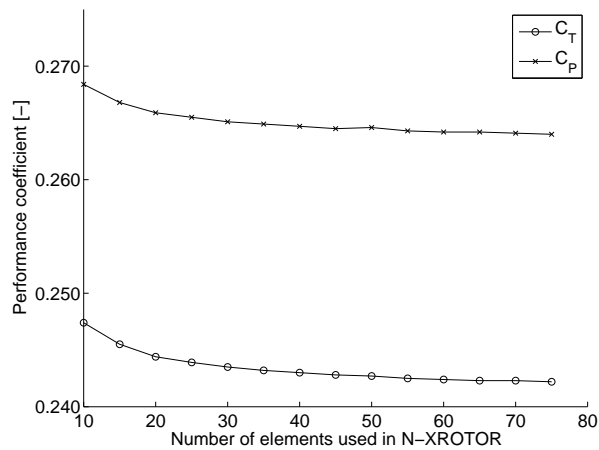


Figure B.1: The effect of the number of radial elements used in XROTOR on the  $C_T$  and  $C_P$  of the N250 propeller at  $J = 0.79$  with a critical  $N$  factor in the  $e^N$  method of 5.

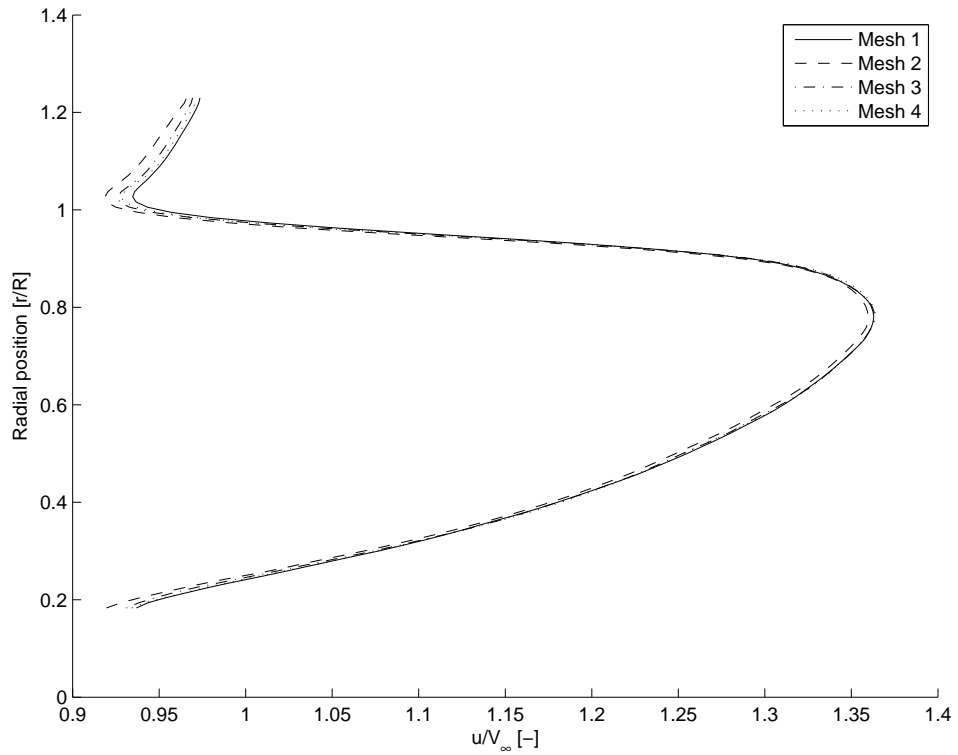
### B.2. MESH REFINEMENT STUDY

Table B.1: Definition of sub-meshes used in the grid convergence study of the isolated fuselage CFD simulation

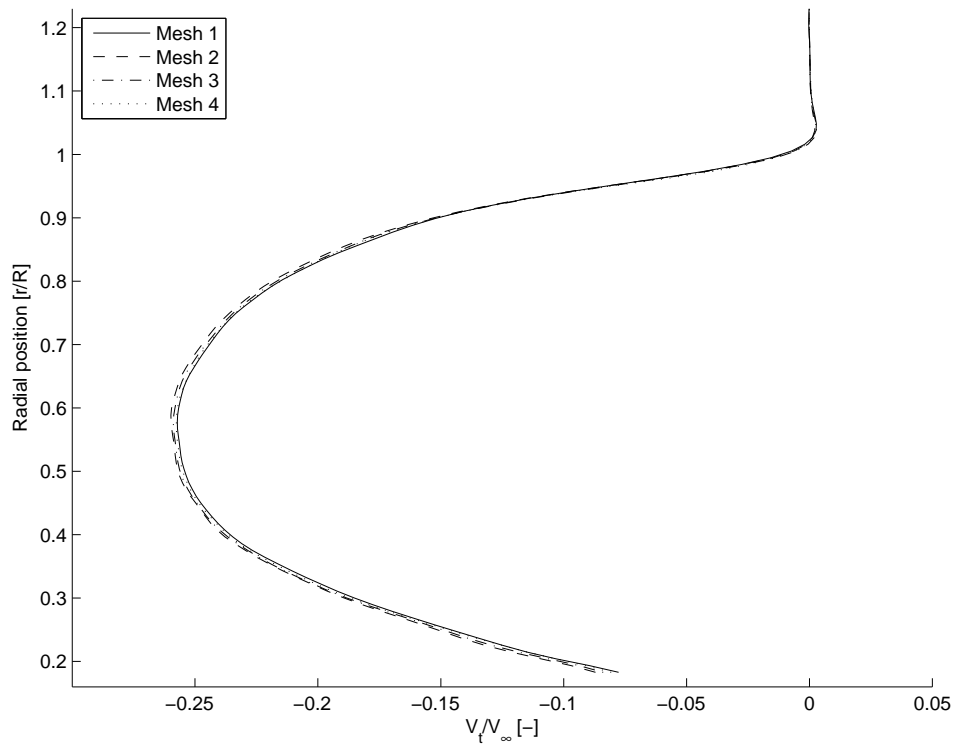
Volume	Mesh Type	Element size [m]
Outer domain	Coarse	$1.0e-1$
	Fine	$8.0e-2$
Refinement box	Coarse	$1.0e-1$
	Fine	$5.0e-2$
Upstream domain	Coarse	$1.5e-2$
	Fine	$1.0e-3$
Rotating domain	Coarse	$9.0e-3$
	Fine	$7.0e-3$
Slipstream domain	Coarse	$1.5e-2$
	Fine	$7.0e-3$
Propeller surface	Coarse	$1.0e-3$
	Fine	$7.0e-4$
	Extra fine	$6.0e-4$
Propeller leading edge	Coarse	$1.2e-4$
	Fine	$1.0e-4$
	Extra fine	$9.0e-5$
Propeller trailing edge	Coarse	$1.0e-4$

Table B.2: Grid refinement study on the isolated uniform inflow CFD simulation of the N250 propeller using the Multiple Reference Frame approach. The different meshes can be constructed using table B.1. The general flow settings are listed in table 5.1. For the drag computation the  $\kappa - \omega$  SST turbulence model is used.

Mesh	Outer domain	Refinement box	Upstream	Rotating part	Slipstream	Propeller Surface and LE	Number of elements	$C_T$ [-]	$C_P$ [-]
Mesh 1	Coarse	Coarse	Coarse	Coarse	Coarse	Coarse	6,473,833	0.2190	0.2469
Mesh 2	Coarse	Coarse	Coarse	Fine	Fine	Fine	8,704,778	0.2214	0.2483
Mesh 3	Fine	Fine	Fine	Fine	Fine	Fine	9,129,987	0.2209	0.2480
Mesh 4	Fine	Fine	Fine	Fine	Fine	Extra fine	10,753,963	0.2195	0.2470



(a)



(b)

Figure B.2: Comparison of CFD results of the circumferentially averaged axial (a) and tangential (b) velocities at a plane just downstream of the propeller computed with different meshes for the N250 propeller at  $J = 0.79$  using the Multiple Reference Frame method in Fluent

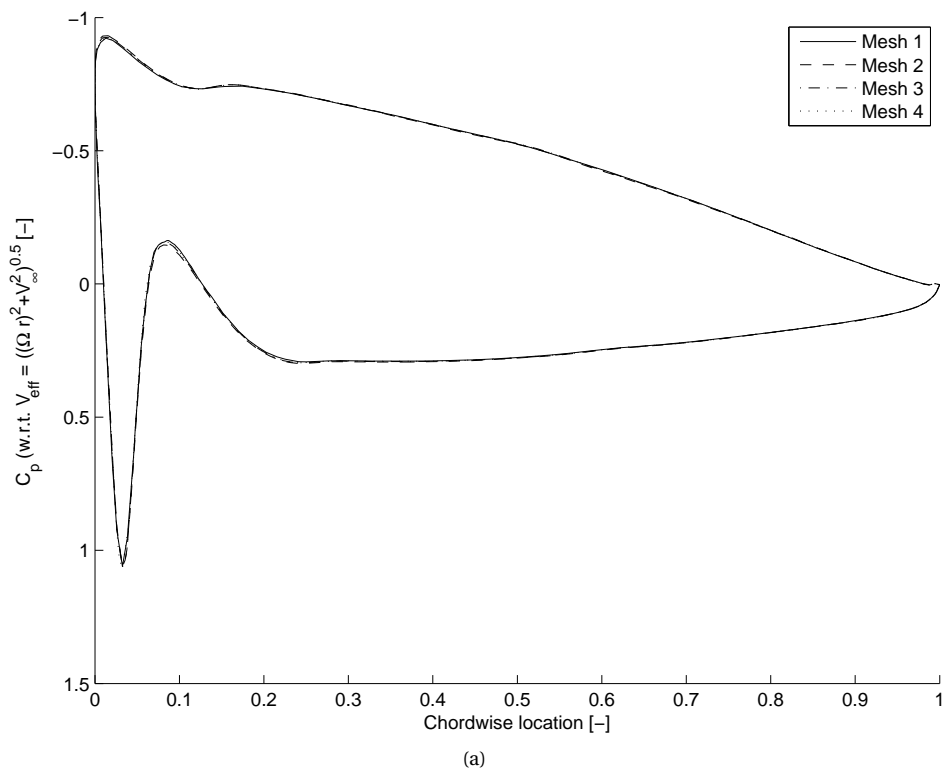


Figure B.3: Comparison of CFD results of the  $C_p$  distribution at  $r/R = 0.70$  computed with different meshes for the N250 propeller at  $J = 0.79$  using the Multiple Reference Frame method in Fluent

### B.3. EFFECT OF TRANSITION IN N-XROTOR ON $C_l(r)$ AND $C_d(r)$

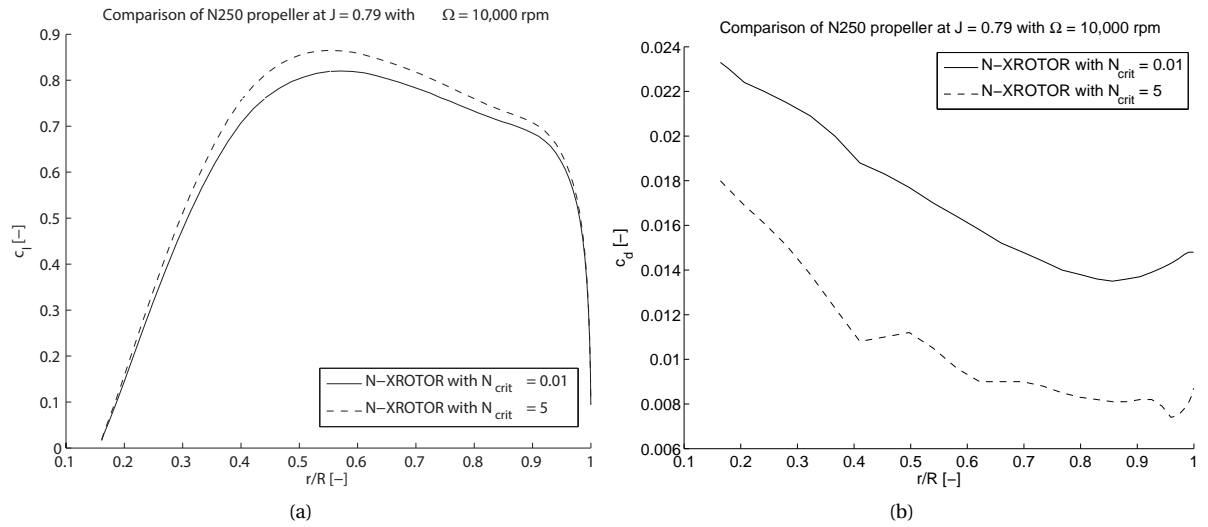


Figure B.4: Effect of  $N_{crit}$  in the  $e^N$  method on the lift and drag coefficient distributions computed with N-XROTOR on the N250 propeller

### B.4. EFFECT OF LOW- $Re$ CORRECTION ON CFD RESULTS

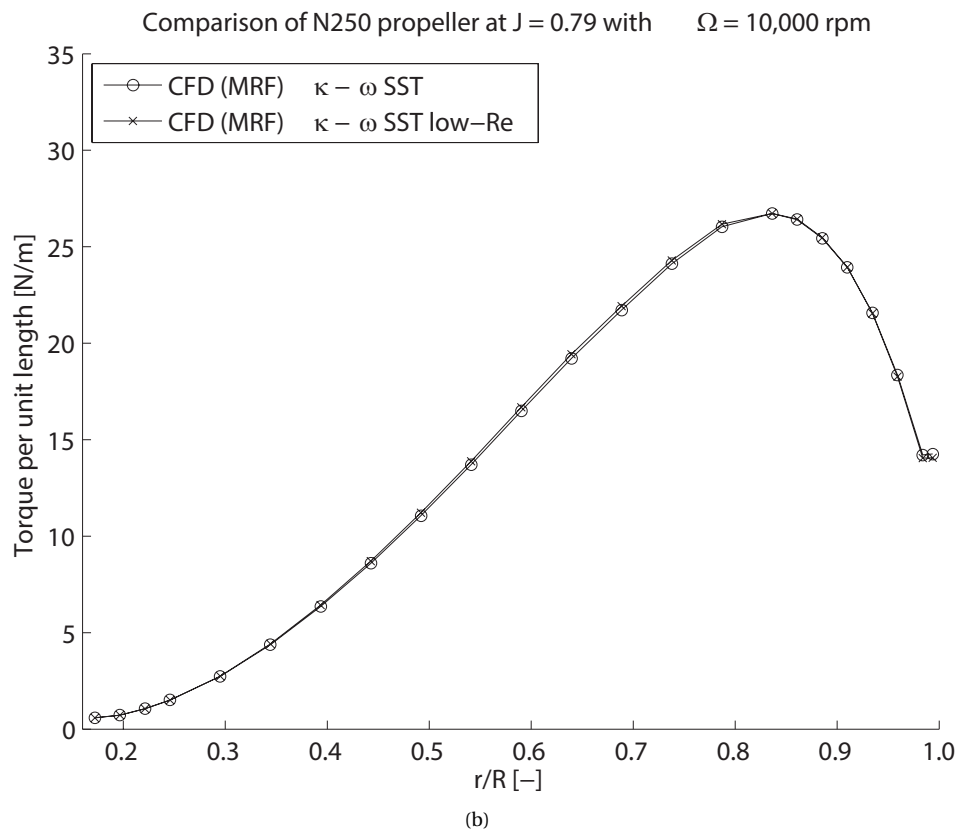
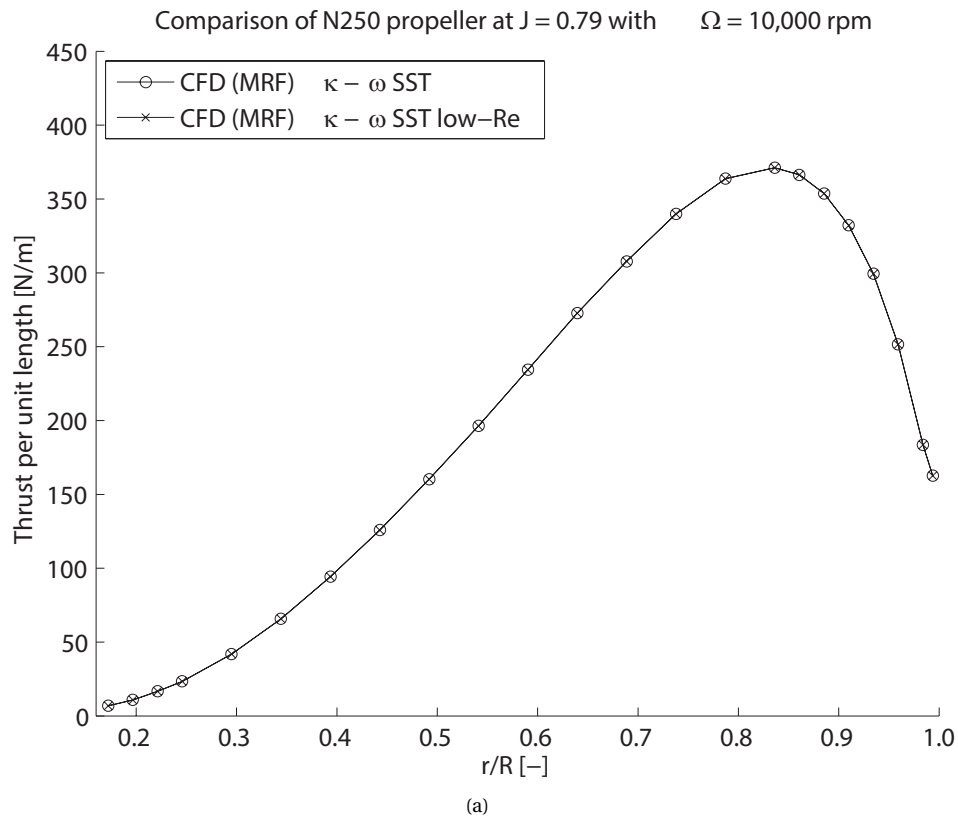


Figure B.5: Comparison of CFD results of the N250 propeller with the standard  $\kappa - \omega$  SST model and the  $\kappa - \omega$  SST model with low Reynolds number correction. The Reynolds number on the blade varies between  $1 \cdot 10^5$  to  $4 \cdot 10^5$

# C

## DESCRIPTION OF REFERENCE FUSELAGE SHAPE

This appendix provides the detailed shape of the fuselage used in the CFD calculations to obtain an inflow profile for the to-be-optimised propeller.

The fuselage has three sections; a fore-body, a center body and an aft-body. Figure C.1 gives a line representation of the fuselage.

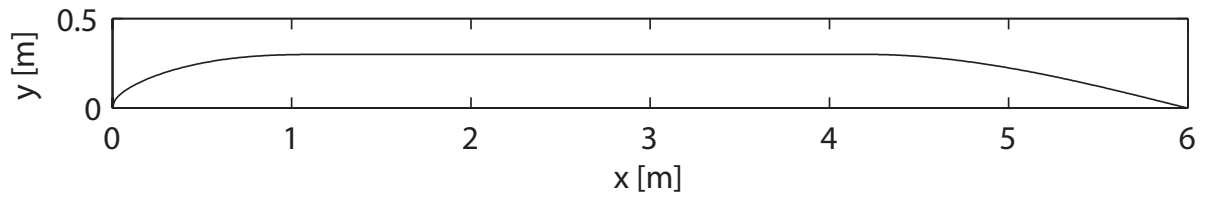


Figure C.1: Contour of reference fuselage based on body 7 from Chappell et al. [88].

Table C provides the mathematical representation of the fuselage contour and relevant constants.

Fuselage section	$y/R_{fuselage}$ [-] description	Constants	Section length	Common name
Fore-body	$\frac{y}{R_{fuselage}} = \frac{\alpha_1^{1/2}}{8} (15 - 10\alpha_1 + 3\alpha_1^2)$ $\alpha_1 = \left[ \frac{x}{L_{f,FB}} + k_1 \left( \frac{x}{L_{f,FB}} \right)^2 \right] / (1 + k_1)$	$k_1 = 1$	$L_{f,FB} = 1.2 [m]$	ESDU I
Center-body	$\frac{x}{R_{fuselage}} = 1$	-	$L_{f,CB} = 3 [m]$	-
Aft-body	$\frac{y}{R_{fuselage}} = 1 - (3 - 2A) \left[ 1 - \frac{x}{L_{f,AB}} \right]^2$ $+ 2(1 - A) \left[ 1 - \frac{x}{L_{f,AB}} \right]^3$	$A = 0.75$	$L_{f,AB} = 1.8 [m]$	Myring (Cubic)



# D

## CFD SETUP OF NACA AIRFOIL SIMULATION

The following sections describe the propeller geometry of two propellers of which the performance curves are compared with the output of N-XROTOR.

### D.1. CFD SETUP

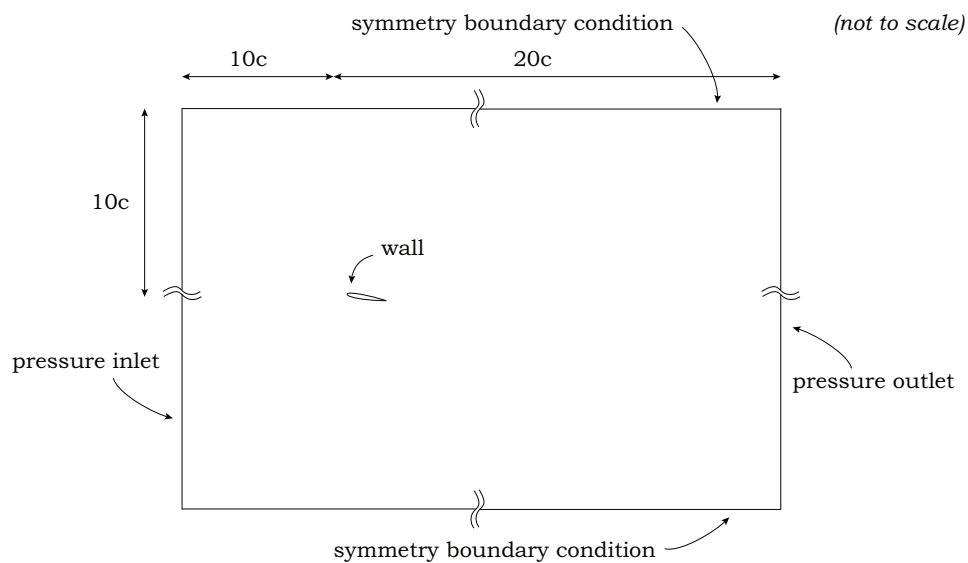


Figure D.1: Domain and boundary conditions of the NACA airfoil CFD simulation to determine the airfoil properties at  $r/R = 0.5$  of the Non-Uniform Inflow propeller design.

### D.2. GRID REFINEMENT STUDY

Mesh	Airfoil surface	Leading edge	Domain	Number of elements
Mesh 1	1.000E-3	4.000E-4	1.5E-2	13,351
Mesh 2	5.000E-4	1.500E-4	7.5E-3	44,755
Mesh 3	1.500E-4	7.000E-5	3.0E-3	261,937

### D.3. EFFECT OF TURBULENCE MODEL



## REFERENCES

- [1] XROTOR User Guide. [http://web.mit.edu/drela/Public/web/xrotor/xrotor\\_doc.txt](http://web.mit.edu/drela/Public/web/xrotor/xrotor_doc.txt), August 2014.
- [2] M. Drela. XFOIL: An Analysis and Design System for Low Reynolds Number Airfoils. *Conference on Low Reynolds Number Airfoil Aerodynamics*, Jun. 1989.
- [3] P. Lv and A.G. Rao. Conceptual Analysis of Boundary Layer Ingestion Towards Aircraft Propulsion Integration. *ISABE conference*, (ISABE 2013-1436), 2013.
- [4] European Commission. Flightpath 2050: Europe's vision for aviation, report of the high level group on aviation research. *Publications Office of the European Union*, 2011.
- [5] O. Atinault, G. Carrier, R. Grenon, C. Verbecke and P. Viscat. Numerical and Experimental Aerodynamic Investigations of Boundary Layer Ingestion for Improving Propulsion Efficiency of Future Air Transport. *31st AIAA Applied Aerodynamics Conference*, 2013.
- [6] A. Seitz and C. Gologan. Parametric design studies for propulsive fuselage aircraft concepts. *CEAS Aeronautical Journal*, 2014. doi: 10.1007/s13272-014-0130-3.
- [7] D.G.M. Davis R.M. Bass. A Review of Some Recent U.K. Propeller Developments. In *AIAA/SAE/ASME/ASCE 21st Joint Propulsion Conference*, Monterey, CA, USA, 1985. doi: 10.2514/6.1985-1261.
- [8] D. Küchemann and J. Weber. *Aerodynamics of Propulsion*. McGraw-Hill, 1953.
- [9] A. Fage and H.E. Collins. An Investigation of the Mutual Interference of Airscrews and Bodies of the Pusher Type. Technical report, Advisory Committee for Aeronautics, 1920.
- [10] W.F. Durand. *Aerodynamic Theory Vol. IV*. Julius Springer, 1935.
- [11] A. Betz. *Introduction to the Theory of Flow Machines*. Pergamon Press, first english edition edition, 1966.
- [12] L. Smith Jr. Wake Ingestion Propulsion Benefit. In *27th Joint Propulsion Conference*, Sacramento, CA, USA, June 1991.
- [13] D.E. Cooney. Lear Fan Propulsion System. Technical Report 800609, LearAvia Corp.
- [14] R.H. Liebeck. Design of the Blended Wing Body Subsonic Transport. *Journal of Aircraft*, 41(1):10–25, Jan.-Febr. 2004. doi: 10.2514/1.9084.
- [15] M. Drela. N+3 Aircraft Concept Designs and Trade Studies, Final Report. Technical Report NASA/CR—2010-216794/VOL2, Glenn Research Center, 2010.
- [16] Photograph Douglas XB-42 aircraft. [http://www.aircraftinformation.info/gallery\\_bombers\\_cancelled.htm](http://www.aircraftinformation.info/gallery_bombers_cancelled.htm), September 2014.
- [17] Photograph Learfan aircraft. [http://www.aircraftinformation.info/gallery\\_bombers\\_cancelled.htm](http://www.aircraftinformation.info/gallery_bombers_cancelled.htm), September 2014.
- [18] Photograph NASA-Boeing X48 aircraft. <http://www.bauhaus-luftfahrt.net/archive/ila-2014-bauhaus-luftfahrt-praesentiert-201epropulsive-fuselage201c>, September 2014.
- [19] Photograph Voltair aircraft. <http://www.airbusgroup.com/int/en/news-media/media-item=eea8f45a-b1a0-4fa5-8ae2-cb2e7e4d011a~.html>, September 2014.

- [20] M. Drela. Power Balance in Aerodynamic Flows. *American Institute of Aeronautics and Astronautics*, 47 (7):1761–1771, Oct. 2009. doi: 10.2514/1.42409.
- [21] A. Arntz, O. Atinault, D. Destarac and A. Merlen. Exergy-based Aircraft Aeropropulsive Performance Assessment: CFD Application to Boundary Layer Ingestion. *American Institute of Aeronautics and Astronautics*, 2014. doi: 10.2514/1.J054072.
- [22] H.D. Kim and J.L. Felder. Control Volume Analysis of Boundary Layer Ingestion Propulsion Systems With or Without Shock Wave Ahead of the Inlet. In *49th AIAA Aerospace Sciences Meeting including the New Horizons Forum and Aerospace Exposition*, Orlando, FL, USA, 2011. doi: 10.2514/6.2011-222.
- [23] H.B. Helmbold. Nachstromschrauben. *Werft, Reederei, Hatzen*, 1927.
- [24] A. Hirner, F. Dorn, Th. Lutz and E. Krämer. Improvement of Propulsive Efficiency by Dedicated Stern Thruster Design. In *7th AIAA Aviation Technology, Integration and Operations Conference*, Belfast, Northern Ireland, 2007. doi: 10.2514/6.2007-7702.
- [25] E.E. Larrabee and S.E. French. Minimum induced loss windmills and propellers. *Journal of Wind Engineering and Industrial Aerodynamics*, 15:317–327, 1983.
- [26] S. Goldstein. On the Vortex Theory of Screw Propellers. *Proceedings of the Royal Society of London A*, 123:440–465, 1929.
- [27] G.J.J. Ruijgrok. *Elements of Airplane Performance*. Delft University Press, 2004. ISBN 90-6275-608-5.
- [28] H. Glauert. *Aerofoil and Airscrew Theory*. Cambridge University Press, 1943.
- [29] D.C. Mikkelsen B.J. Blaha, G.A. Mitchell and J.E. Wikete. Design and Performance of Energy Efficient Propellers for Mach 0.8 Cruise. Technical Report NASA TM X-73612, Lewis Research Center, 1977.
- [30] C.J. Miller and J.P. Sullivan. Noise Constraints Effecting Optimal Propeller Designs. Technical Report TM 86967, Lewis Research Center and Purdue University, 1985.
- [31] F.B. Metzger and C. Rohrbach. Benefits of Blade Sweep for Advanced Turboprops. *Journal of Propulsion and Power*, 2(6):534–540, 1986.
- [32] B.J. Humpert, R.J. Gaeta and J.D. Jacob. Optimal Propeller Design for Quiet Aircraft using Numerical Analysis. In *21st AIAA/CEAS Aeroacoustics Conference*, Dallas, TX, USA, 2015. doi: 10.2514/6.2015-2360.
- [33] O. Gur and A. Rosen. Multidisciplinary Design Optimization of a Quiet Propeller. In *Proceedings of the 29th AIAA Aeroacoustics Conference*, Vancouver, Canada, May 2008. doi: 10.2514/6.2008-3073.
- [34] L. Prandtl. Tragflügel Theorie. *Nachrichten von der Gesellschaft der Wissenschaften zu Göttingen*, pages 451–477, 1918.
- [35] P. van Oossanen. Calculation of Performance and Cavitation Characteristics of Propellers Including Effects of Non-Uniform Inflow and Viscosity. Technical Report 457, Netherlands Ship Model Basin Wageningen, The Netherlands, March 1998.
- [36] H.C. McLemore. Wind-Tunnel Tests of a 1/20-Scale Airship Model with Stern Propellers. Technical Report TN D-1026, Langley Research Center, January 1962.
- [37] A.M.O. Smith and H.E. Roberts. The Jet Airplane Utilizing Boundary Layer Air for Propulsion. *Journal of the Aeronautical Sciences*, 14(2):97–109, 1947.
- [38] F.R. Goldschmied. Aerodynamic Design of Low-Speed Aircraft with a NASA Fuselage/Wake-Propeller Configuration. *American Institute of Aeronautics and Astronautics*, (AI AA-86-2693), 1986.
- [39] M.-H. Wang. *Hub Effects in Propeller Design and Analysis*. Ph.D. Thesis, Massachusetts Institute of Technology, Massachusetts Institute of Technology, 1985.
- [40] Q.R. Wald. The Aerodynamics of Propellers. *Elsevier Progress in Aerospace Sciences*, 42:85–128, Oct. 2006.

- [41] J.H. Rowse and C.T. Havey. Propeller/Propfan In-Flight Thrust Determination. Technical Report AIR4065, Society of Automotive Engineers, 2004.
- [42] A. Betz. Schraubenpropeller mit geringstem Energieverlust. Mit einem Zusatz von L. Prandtl. *Nachrichten von der Gesellschaft der Wissenschaften zu Göttingen, Mathematisch-Physikalische Klasse*, pages 193–217, 1919.
- [43] H.W. Lerbs. Moderately Loaded Propellers with a Finite Number of Blades and an Arbitrary Distribution of Circulation. In *Trans. Society of Naval Architects and Marine Engineers Vol. 60*, New York, NY, USA, November 1952.
- [44] J. Balhan and J.D. van Manen. Ontwerpen van Cavitatievrije Scheepsschroeven. *Schip en Werf*, 1950.
- [45] J.D. van Manen. *Involed van de ongelijkmatigheid van het snelheidsveld op het ontwerp van schepsschroeven*. Ph.D. Thesis, Delft University of Technology, Delft, The Netherlands, 1951.
- [46] G.P. Succi. Design of Quiet Efficient Propellers. In *SAE Technical Paper Series*, Wichita, KS, USA, April 1979. doi: 10.4271/790584.
- [47] J.B.H.M. Schulten. Advanced Propeller Performance Calculation by a Lifting Surface Method. *Journal of Propulsion and Power*, 12(3):477–485, 1996. doi: 10.2514/3.24060.
- [48] S. Mishima. *Design of Cavitating Propeller Blades in Non-Uniform Flow by Numerical Optimization*. Ph.D. Thesis, Massachusetts Institute of Technology, 1996.
- [49] J. Sodja, D. Stadler and T. Kosel. Computational Fluid Dynamics Analysis of an Optimized Load-Distribution Propeller. *Journal of Aircraft*, 2012. doi: 10.2514/1.C031469.
- [50] O. Gur and A. Rosen. Comparison between blade-element models of propellers. *The Aeronautical Journal*, 112(1138):689–704, Dec. 2008.
- [51] A. Colozza. High Altitude Propeller Design and Analysis Overview. Technical report, Federal Data Systems, March 1998.
- [52] N.K. Borer and M.D. Moore. Integrated Propeller - Wing Design Exploration for Distributed Propulsion Concepts. In *53rd AIAA Aerospace Sciences Meeting*, Kissimmee, FL, USA, 2015. doi: 10.2514/6.2015-1672.
- [53] T. Sinnige and L.L.M. Veldhuis. Pylon Trailing Edge Blowing Effects on the Performance and Noise Production of a Pusher Propeller. In *52nd Aersopace Sciences Meeting*, National Harbor, Maryland, USA, January 2014. doi: 10.2514/6.2014-0566.
- [54] I.H. Abbott and A.E. von Doenhoff. *Theory of Wing Sections*. Dover Publications, 1959. ISBN 90-6275-608-5.
- [55] R.S.W. Cheung. VGK method for two-dimensional aerofoil sections. Part 1: principles and results. Technical Report ESDU 96028, IHS ESDU, 2004.
- [56] J.L. van Ingen. The eN method for transition prediction. Historical review of work at TU Delft . In *38th Fluid Dynamics Conference and Exhibit*, Seattle, WA, USA, June 2008.
- [57] H. Snel, R. Houwink and J. Bosschers. Sectional Prediction of Lift Coefficients on Rotating Wind Turbine Blades in Stall. Technical Report ECN-C-93-052, National Aerospace Laboratory (NLR), 1994.
- [58] G.J.D. Zondervan. *A Review of Propeller Modelling Techniques Based on Euler Methods*. Delft University Press, 1998.
- [59] S.B. Pope. *Turbulent Flows*. Cambridge University Press, ninth edition, 2011. ISBN 978-0-521-59886-6.
- [60] C. Lindenburg. Modelling of Rotational Augmentation Based on Engineering Considerations and Measurements. Technical Report ECN-RX-04-131, ECN, 2004.
- [61] J.D. Anderson, Jr. *Fundamentals of Aerodynamics, 4th edition*. McGraw-Hill, 2007. ISBN 007-125408-0.

- [62] J. Klesa. Optimal Circulation Distribution on Propeller with the Influence of Viscosity. In *32nd Applied Aerodynamics Conference*, Atlanta, GA, USA, Jun. 2014. doi: 10.2514/6.2014-3132.
- [63] B.M. Kulfan. Universal Parametric Geometry Representation Method. *Journal of Aircraft*, 45(1):142–158, 2008.
- [64] Nationaal Lucht en Ruimtevaartlaboratorium. N250 propeller Shoptest. Technical report, NLR, 1993.
- [65] A.J. Evans and G. Liner. A Wind-Tunnel Investigation of the Aerodynamic Characteristics of a Full-Scale Sweptback Propeller and two Related Straight Propellers. Technical Report NACA RM L50J05, Langley Aeronautical Laboratory, 1951.
- [66] D.C. Wilcox. *Turbulence Modeling for CFD*. DCW Industries, third edition, 2006. ISBN 978-1-928729-08-2.
- [67] E.W.M. Roosenboom, A. Stürmer and A. Schröder. Advanced Experimental and Numerical Validation and Analysis of Propeller Slipstream Flows. *Journal of Aircraft*, 47(1):284–291, 2010. doi: 10.2514/1.45961.
- [68] L.P. Ruiz-Calavera and D. Perdonés-Díaz. CFD computation of in-plane propeller shaft loads. In *49th AIAA/ASME/SAE/ASEE Joint Propulsion Conference*, San Jose, CA, USA, 2013. doi: 10.2514/6.2013-3798.
- [69] B. Ortun, R. Boisard and I. Gonzalez-Martino. In-plane airloads of a propeller with inflow angle: prediction vs. experiment. In *Proceedings of the 29th AIAA Aeroacoustics Conference*, New Orleans, Louisiana, USA, June 2012. doi: 10.2514/6.2012-2778.
- [70] J. Yin, A. Stuermer and M. Aversano. Aerodynamic and Aeroacoustic Analysis of Installed Pusher-Propeller Aircraft Configurations. *Journal of Aircraft*, 49(5):1423–1433, 2012. doi: 10.2514/1.C031704.
- [71] *ANSYS FLUENT Theory Guide, Release 14.5.*, 2012.
- [72] S.-E. Kim and S.H. Rhee. Assessment of Eight Turbulence Models for a Three-Dimensional Boundary Layer Involving Crossflow and Streamwise Vortices. In *40th Aerospace Sciences Meeting and Exhibit*, Reno, Nevada, USA, January 2002. doi: 10.2514/6.2002-852.
- [73] J.E. Bardina, P.G. Huang and T.J. Coakley. Turbulence Modeling Validation, Testing, and Development. Technical Report 110446, NASA, 1997.
- [74] S. Béchet, C.A. Negulescu, V. Chapin and F. Simon. Integration of CFD Tools in Aerodynamic Design of Contra-Rotating Propeller Blades. In *3rd CEAS Air and Space Conference*, 2011.
- [75] C.O. Márquez, A. Stuermer, C. Clemen and A. Grimminger. Validation of Actuator Disk Simulations of CROR Propulsion Systems at Low-Speed Flight Conditions. In *30th AIAA Applied Aerodynamics Conference*, New Orleans, LA, USA, June 2012. doi: 10.2514/6.2012-2787.
- [76] M. Meheut. Thrust and Torque Far-Field Analysis of Propeller and Counter Rotating Open Rotor Configurations. In *31st AIAA Applied Aerodynamics Conference*, San Diego, CA, USA, 2013. doi: 10.2514/6.2013-2803.
- [77] F. Falissard, R. Boisard and G. Delattre. Aeroacoustic Computation of a Contra Rotating Open Rotor Model with Test Rig Installation Effects. In *18th AIAA/CEAS Aeroacoustics Conference*, Colorado Springs, CO, USA, 2012. doi: 10.2514/6.2012-2218.
- [78] C.L. Rumsey and P.R. Spalart. Turbulence Model Behavior in Low Reynolds Number Regions of Aerodynamic Flowfields. In *38th AIAA Fluid Dynamics Conference and Exhibit*, Seattle, WA, USA, June 2008. doi: 10.2514/1.29373.
- [79] D.S. Jang, R. Jetli and S. Acharya. Comparison of the PISO, SIMPLER, and SIMPLEC Algorithms for the Treatment of the Pressure-Velocity Coupling in Steady Flow Problems. *Numerical Heat Transfer: An International Journal of Computation and Methodology*, pages 209–228, 1986.
- [80] C. Lenfers. Propeller Design for a future QESTOL Aircraft in the BNF Project. In *30th AIAA Applied Aerodynamics Conference*, New Orleans, LA, USA, 2012. doi: 10.2514/6.2012-3334.

- [81] B.G. Marinus. Comparative Study of Effects of Sweep and Humps on High-Speed Propeller Blades. *American Institute of Aeronautics and Astronautics*, 52(4):739–746, Apr. 2014.
- [82] S. Brizzolara, D. Villa and S. Gaggero. A systematic comparison between RANS and Panel Methods for Propeller Analysis. In *Proceedings of 8th International Conference on Hydrodynamics*, Nantes, France, October 2008.
- [83] L.L.M. Veldhuis and G.W. Luursma. Comparison of an Actuator Disk and a Blade Modeling Approach in Navier-Stokes Calculations on the SR-3 Propfan. *Fluid Dynamics and Co-located Conferences. American Institute of Aeronautics and Astronautics*, pages 924–932, 2000. doi: 10.2514/6.2000-4528.
- [84] G.V. Shankaran and M.B. Dogruoz. Validation of an Advanced Fan Model with Multiple Reference Frame Approach. *IEEE*, 211:497–513, 1990. doi: 10.1109/ITHERM.2010.5501404.
- [85] P.R. Spalart and C.L. Rumsey. Effective Inflow Conditions for Turbulence Models in Aerodynamic Calculations. *AIAA Journal*, 45(10):2544–2553, 2007. doi: 10.2514/1.29373.
- [86] E. H. Hirschel, J. Cousteix and W. Kordulla. *Three-Dimensional Attached Viscous Flow*. Springer, ninth edition, 2014. ISBN 978-3-642-41378-0.
- [87] A. Taranov and M. Lobachev. Influence of the Laminar-Turbulent Transition on the Accuracy of the Propeller Characteristics Prediction in the Model Scale. *IEEE*, (978-1-4799-6824-4/15).
- [88] P.D. Chappell, A.J. Clarke and R. Porter. Geometrical characteristics of typical bodies. Technical Report ESDU 77028, IHS ESDU, 1977.
- [89] I. Samuelsson. Experimental Investigation of Low Speed Model Propeller Slipstream Aerodynamic Characteristics Including Flow Field Surveys and Nacelle/Wing Static Pressure Measurements. *ICAS*, 1990.
- [90] M. Barry, N. Sirvin and J.-C. Boniface. Open-Rotor Aerodynamics Installation Effects By a RANS-Lifting Line Coupling Method. In *50th AIAA/ASME/SAE/ASEE Joint Propulsion Conference*, Cleveland, OH, USA, July 2014. doi: 10.2514/6.2014-3887.
- [91] P.D. Chappell. Profile drag of axisymmetric bodies at zero incidence for subcritical Mach numbers. Technical Report ESDU 78019, IHS ESDU, 1978.
- [92] H.K. Schlichting. *Boundary-Layer Theory*. McGraw-Hill, 1960.
- [93] Jin-Keun Choi and S.A. Kinnas. Prediction of Non-Axisymmetric Effective Wake by a Three-Dimensional Euler Solver. *Journal of Ship Research*, Vol. 45, No. 1, 2001.
- [94] P. Lv. Research progress on Boundary Layer Ingestion. Presentation (unpublished), 2014.
- [95] A.P. Plas, M.A., V. Madani, D. Crichton, E.M. Greitzer, T.P. Hynes and C.A. Hall. Performance of a Boundary Layer Ingestion (BLI) Propulsion System. In *45th AIAA Aerospace Sciences Meeting and Exhibit*, Reno, NV, USA, January 2007.
- [96] T.E. Taylor. Combined Experimental and Theoretical Determination of Effective Wake for a Marine Propeller. Master's thesis, Massachusetts Institute of Technology, 1994.
- [97] T. Theodorsen. *Theory of Propellers*. McGraw-Hill, 1948.
- [98] F.D. Harris. Preliminary Study Of Radial Flow Effects On Rotor Blades. *Journal of the American Helicopter Society*, 11(3):1–21, 1966. doi: 10.4050/JAHS.11.1.

